LABORATORY TESTING OF LATERAL LOAD RESPONSE FOR MONOPILES IN SAND

Final Report

From:

Dr. Robert Gilbert, UT Austin

Dr. Kenneth Stokoe, UT Austin

Yunhan Huang, UT Austin

James Munson, UT Austin

Jonas Bauer, UT Austin

Reihaneh Hosseini, UT Austin

Ahmed Hussien, UT Austin

Dr. Shin-Tower Wang, ENSOFT

Dr. Hossein Fadaifard, ENSOFT

Date:

August 24, 2018

DISCLAIMER

Neither the United States Government nor any agency thereof, nor any of their employees or officers, makes any warranty, express or implied, or assumes any legal liability or responsibility for the accuracy, completeness, or usefulness of any information, apparatus, product, or process disclosed, or represents that its use would not infringe privately owned rights. Reference herein to any specific commercial product, process, or service by trade name, trademark, manufacturer, or otherwise, does not necessarily constitute or imply its endorsement, recommendation, or favoring by the United States Government or any agency thereof. The views and opinions of document authors expressed herein do not necessarily state or reflect those of the United States Government or any agency thereof.

ACKNOWLEDGEMENT

Table of Contents

Appendix A – Database of Lateral Load Test of Monopiles in Sand

Appendix B – Udit Dasgupta UT Austin Thesis

Appendix C – Computer Model for Calculation of Resonance Frequency

Appendix D – Resonant Column Tests on All-Purpose Sand

Appendix E – Resonant Column Tests on Mustang Island Sand

List of Tables

List of Figures

Executive Summary

The current design methods for laterally-loaded offshore foundations in sand, API RP 2GEO (2011) and DNV (2013), are unverified for the large diameter, relatively short monopiles used for offshore wind turbines. The following factors are either questionable or not addressed by current design guidance for wind turbine monopiles: (1) monopiles have a significantly large pile diameter and small length-to-diameter ratios; (2) monopiles are subjected to large numbers of relatively small-amplitude cyclic loads that affect the lateral stiffness and the accumulated lateral displacement/rotation.

The objective of this research is to evaluate the suitability of existing guidance for the design of laterally-loaded monopiles at small displacements and to provide recommendations for improving design methods for monopile foundations. The research consisted of compiling and analyzing a data base of publicly available lateral load tests on field-scale piles, compiling and analyzing field monitoring data for offshore wind turbines in Belgium, developing a three-dimensional finite element method (3D FEM) model that incorporates a constitutive model to represent the non-linear stiffness of sand at even small shear strains, performing and analyzing foundation model tests in the laboratory using laterally-loaded spheres in sand beds, holding a technical workshop with technical experts from the U.S. and Europe, and developing design recommendations based on the results.

The following major conclusions are drawn from this research:

1) Model tests, field tests and operating wind turbines all show that the p-y curves from current design practice tend to underestimate the initial stiffness for laterally loaded piles and fail to capture the non-linearity of the stiffness at small lateral displacements. They also show that the lateral stiffness and the permanent lateral displacement tends to increase with increasing cycles of small-amplitude, one-way lateral loads.

2) A 3-D FEM model that incorporates a constitutive model to characterize the small-strain properties of sand, including the maximum shear stiffness at very small strains and the relationships between shear stiffness and shear strain and shear stiffness and effective confining stress, is capable of predicting the response of laterally loaded piles both at model and field scales.

These conclusions lead to the following recommendations for design of laterally loaded monopiles in sand:

1) Exercise caution in using conventional p-y curves for sand to predict the performance of offshore wind turbine monopiles in service. The p-y curves used in current design practice do not predict well the stiffness and the non-linearity of laterally loaded piles at the small lateral displacements relevant for offshore wind turbine monopiles in service.

2) Measure directly or empirically establish for sand the in situ maximum ("small-strain") shear modulus, the relationship between shear modulus and shear strain, the relationship between shear modulus and effective confining pressure, and the effect of cyclic loading on the shear modulus. These small-strain properties are needed in order to predict the stiffness and non-linearity of laterally loaded piles at small lateral displacements.

3) Establish improved p-y curves to be used in design directly from 3-D FEM analyses using representative properties of the sand in situ at small strains. It may also be possible with future

research to establish these curves from simplified models relating the shapes of the p-y curves to the small-strain properties of the sand.

Future work is recommended in the following areas to better integrate the results from this research into practice:

1) The proposed finite element model needs to be extended to capture the behavior at large displacements for design with ultimate load cases. While these cases, in our experience, do not govern the design of offshore monopiles, it would be helpful for the proposed approach to capture both design cases realistically.
2) The effects of cyclic loading on stiffness and permanent displacement need to be incorporated into (1) the laboratory testing procedures to characterize these properties of the sand and (2) into the finite element model to represent these properties realistically.
3) Simpler design approaches to adjust the p-y curves used in current practice to better represent the behavior of laterally loaded piles at small (service load) displacements need to be refined and made as practical as possible.
4) Additional analyses of field data from lateral load tests (e.g., the PISA lateral load tests on piles in sand) and monitoring results from offshore wind turbines are always needed to better understand and characterize the complicated behavior of laterally loaded piles subjected to many cycles of load at relatively small amplitudes of displacement.

0 Introduction

The current design methods for laterally-loaded offshore foundations in sand, API RP 2GEO (2011) and DNV (2013), are unverified for the large diameter, relatively short monopiles used for offshore wind turbines. The following factors are either questionable or not addressed by current design guidance for wind turbine monopiles: (1) monopiles have a significantly large pile diameter and small length-to-diameter ratios; (2) monopiles are subjected to large numbers of relatively small-amplitude cyclic loads that affect the lateral stiffness and the accumulated lateral displacement/rotation.

The objective of this research is to evaluate the suitability of existing guidance for the design of laterally-loaded monopiles at small displacements and to provide recommendations for improving design methods for monopile foundations. The research consisted of six tasks:

1) Lateral Load Model Test Database: A database was compiled from publicly available lateral load tests, focusing on the effects of cyclic loading for relatively stiff piles in sand. A master's thesis studying the contents of the data base was published and its major conclusions are summarized.
2) Offshore Wind Turbine Performance: Data was received from Parkwind for Bligh Bank Offshore Wind Farm and Northwind Offshore Wind Farm. The data was reviewed and analyses were performed using the data.
3) Numerical Analyses: A three-dimensional finite element method (FEM) approach was developed to model the lateral stiffness of a monopile in sand. This approach incorporates a constitutive model based on field and laboratory test results that utilizes an orthotropic linear elastic material and strain-induced anisotropy. It has been calibrated with element laboratory tests and compared with the Mustang Island lateral load pile tests that provided the original basis for the standard of practice in the design of laterally loaded piles in sand.
4) Lateral Load Model Tests: The FEM approach was applied to design a series of laboratory model tests using a sphere to represent the states and strain around a monopile. Static and cyclic testing were conducted.
5) Technical Workshop: A workshop was held in Austin, Texas to obtain technical guidance on the methods of analyses, the results and the conclusions of the research. The workshop was attended by a variety of technical experts from academia and industry including representatives from the European Joint Industry Pile-Soil Analysis (PISA) Project, which is investigating and developing improved design methods for laterally loaded monopiles.
6) Design Guidance: Guidance has been developed to incorporate the conclusions from this research into practical recommendations for the design of laterally loaded monopiles in sand.

This report consists of six chapters after the Introduction summarizing the work done in each task. In addition, appendices with the database of lateral load tests, computer codes, field and laboratory test results, and M.S. theses produced from this research are included.

1 Database of Laterally Loaded Piles Tests in Sand

1.1 Overview of Database

This section of the report constitutes the analysis of the product from Task 1 - Lateral Load Test Database of Monopiles in Sand. A literature review was carried out to find lateral load tests on deep foundations in predominantly sandy soils. The majority of the load test results in this database were obtained from papers and/or reports published by the original researchers who conducted the tests. These data were supplemented by load test results extracted from the Deep Foundation Load Test Database (DFLTD) by the Federal Highway Administration (FHWA) and by the Laterally Loaded Pile Database by the University of Florida. The database maintained by UC Irvine, DFI and ADSC (www.findapile.com) was also utilized. Data from over 150 lateral load tests was obtained, 82 of which are included in this database. Key criteria used in the selection process were soil stratigraphy, shape of foundation, and diameter of foundation.

The database has the following attributes:

- Total of 82 tests on laterally loaded deep foundations
- Tests conducted in clean sands (51), silty sands (19), gravelly sand (1) and layered clay-sand stratigraphy (11)
- Steel pipe piles, steel solid piles, reinforced concrete drilled shafts, winged monopiles, and prestressed concrete piles/shafts
- Field tests, and laboratory tests (including one-g and centrifuge) on models
- Pile/shaft diameters ranging from 2 inches to 173 inches (prototype model in centrifuges)
- Pile/shaft aspect ratios (length/diameter) ranging from 1 to 81

This database is compiled in the form of an MS Excel® spreadsheet that is included as Appendix A. Each test result is saved in a numbered worksheet; in some cases a single worksheet holds multiple test results. The worksheet named "Contents" provides a table of all the test results together with some key attributes of the load tests and the numbered worksheet in which each test result can be found. This table can sorted as required by the user via the "Sort & Filter" option in Excel; however, the order of worksheet tabs will not change.

Each test record contains two pages of data. The first page contains qualitative information about the load test such as source, type of lateral load test (monotonic and/or cyclic loading), pile head constraints (rotational fixity at pile head), and dates of installation and testing. Information regarding method of installation, soil stratigraphy, loading sequence, test results, and references are provided in greater detail. A schematic diagram of the pile setup including a simplified soil stratigraphy is also provided. The second page contains quantitative data such as foundation dimensions, structural properties, soil properties, and load-deflection data. A graph of measured load versus deflection is shown at the bottom of the page. In the cases, where multiple results need to be shown, a third page of results is added.

A worksheet named "Template" is included for the purpose of adding new data in the future.

A description of the database and detailed analyses of tests in the data base is provided in a M.S. thesis by Udit Dasgupta (Appendix B).

1.2 Analysis of Field Tests in Database

Selected field tests in the database are analyzed using the conventional p-y curve approach that is the standard of practice for laterally loaded monopiles. For this analysis, emphasis is placed on the initial stiffness of the lateral load and displacement curve with a displacement level of 0.25% of the pile diameter as a threshold of "small" displacement.

1.2.1 Mustang Island Test

Mustang Island Test was one of the field tests that were used to develop the conventional p-y curves for sands (Cox et al. 1974). The monotonic and cyclic responses are plotted against the conventional p-y curve approach predictions (Figure 1.1 and Figure 1.2). The p-y approach underestimates the stiffness at the relatively small lateral displacements of interest, particularly after cyclic loading. In addition, the measured response is non-linear, even at small displacements.

(a) Full range of results   (b) Range upto 0.0025 of Diameter
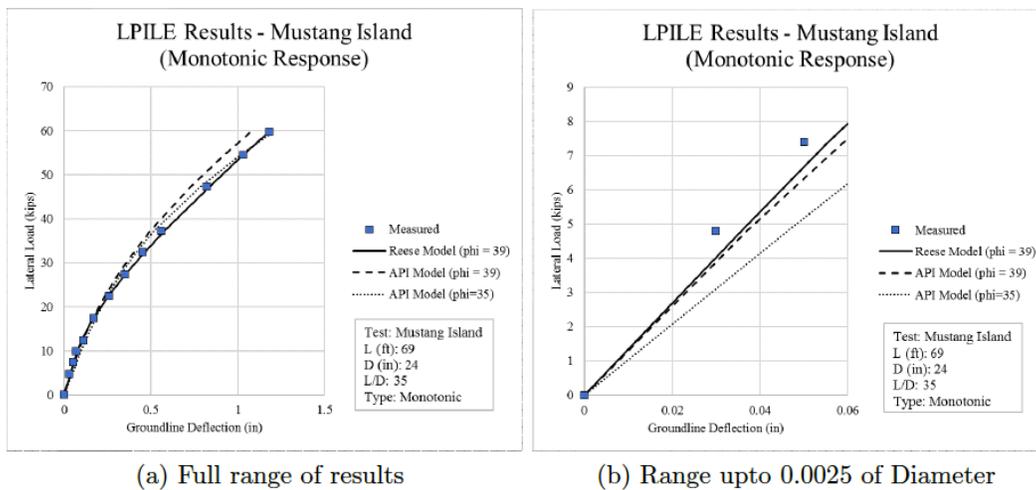
Figure 1.1 Comparison of measurements and p-y results for Mustang Island Field Tests – static loading

(a) Full range of results   (b) Range upto 0.0025 of Diameter
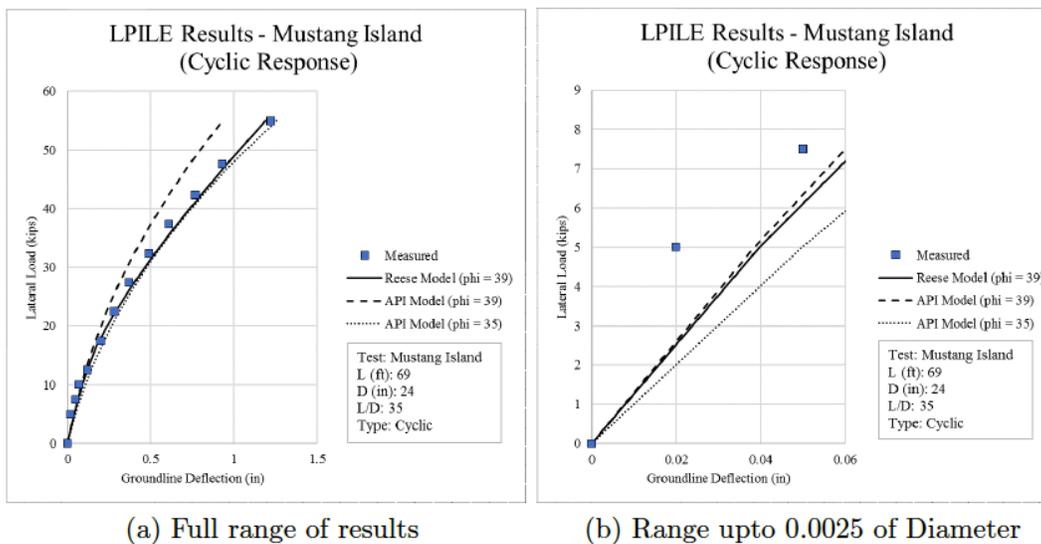
Figure 1.2 Comparison of measurements and p-y results for Mustang Island Field Tests – cyclic loading

1.2.2 Houston Test

The purpose of Houston Test was to subject piles to cyclic horizontal loading and study the corresponding accumulation of horizontal displacement (Little and Briaud 1988). The monotonic response data for the piles is given up to a load level of 40 kips. Beyond that, two stages of cyclic loading were done and the monotonic backbone curve is given. There is a good fit for the monotonic portion of the curve. On zooming in to a low strain level (Figure 1.3 and Figure 1.4), the API p-y method underestimates the response and does not capture the non-linearity of the response.
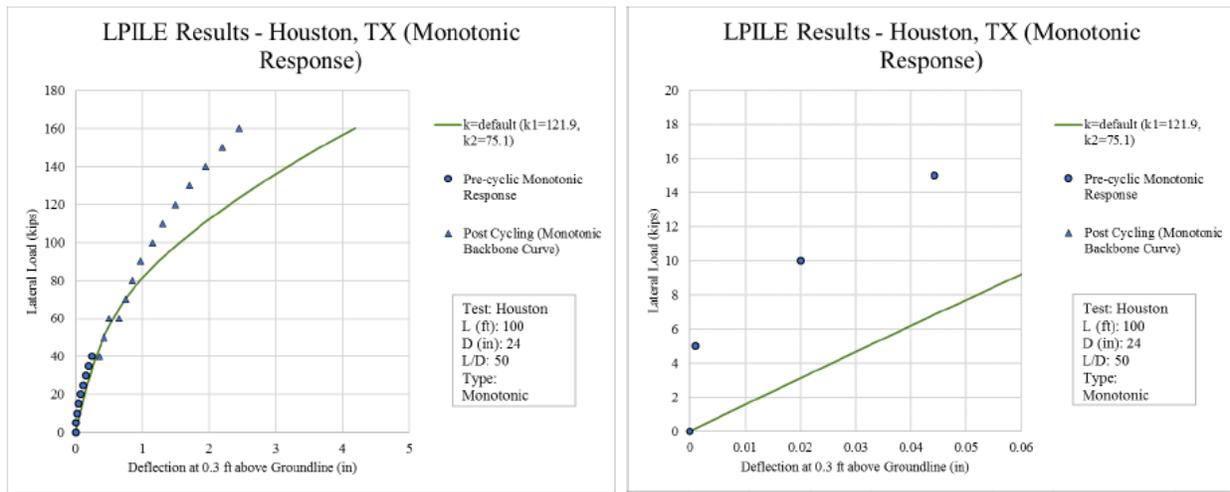
(a) Full range of results   (b) Range upto 0.0025 of Diameter

Figure 1.3 Comparison of measurements and p-y results for Houston Field Tests – static loading
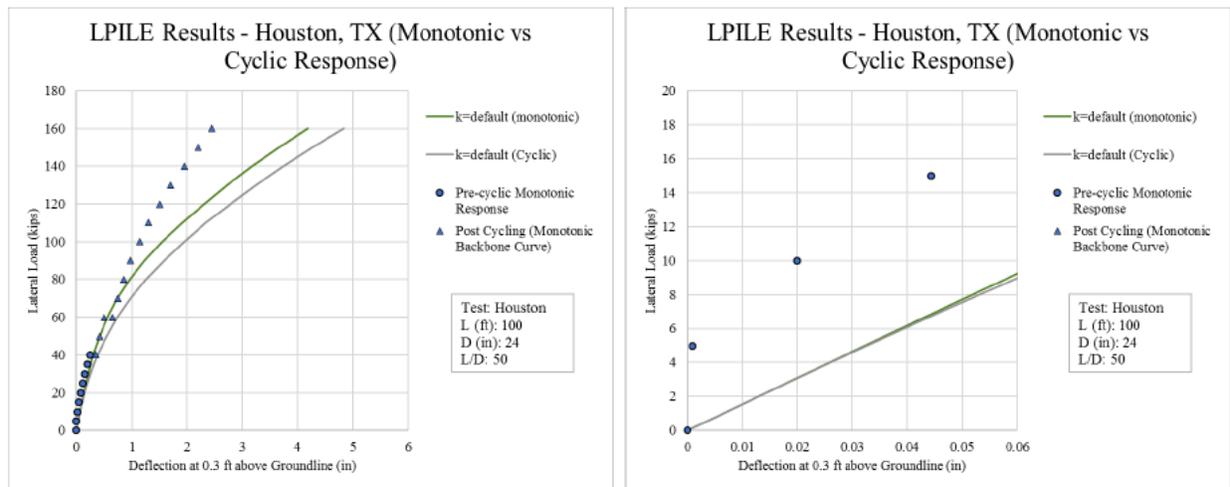
(a) Full range of results   (b) Range upto 0.0025 of Diameter

Figure 1.4 Comparison of measurements and p-y results for Houston Field Tests – cyclic loading

1.3 Database Conclusions

Major conclusions from analysis of the test results in the database are as follows:

1) The current design practice for laterally loaded piles in sand utilizes p-y curves that produce an initial linear relationship between lateral load and displacement of the pile head. This linear relationship is controlled by a parameter k characterizing an elastic subgrade modulus; the subgrade modulus is determined as a function of the friction angle of the sand.

2) In all of lateral load tests with enough resolution to discern the initial relationship between load and displacement of the pile head, the relationship is not linear and is, therefore, not easily captured by assuming an elastic subgrade modulus.

3) In general, the p-y curves from the current design practice underestimate the initial stiffness of laterally loaded piles in sand, both for monotonic and cyclic tests.

2 Offshore Wind Turbine Performance

Parkwind has provided access to field performance data from offshore wind turbines in the Belwind Offshore Wind Farm and the Northwind Offshore Wind Farm. The information includes geotechnical reports, design reports for the monopiles, pile installation data, and field monitoring results.

2.1 Belwind Offshore Wind Farm

Belwind Offshore Wind Farm is in the Flemish Banks area of the southern North Sea off the Belgian coast (Figures 2.1 and 2.2). A total of 55 wind turbine generator (WTG) structures, each with a rated power output of 3 MW, and 1 substation were installed in 2009. The support structures are driven monopiles with grouted transition pieces that support the WTG tower structures.
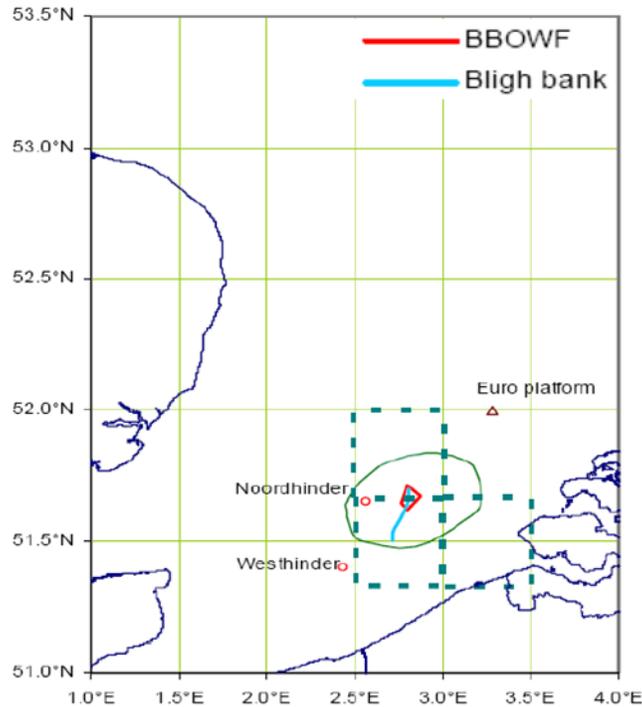
Figure 2.1 Location of Belwind offshore wind farm
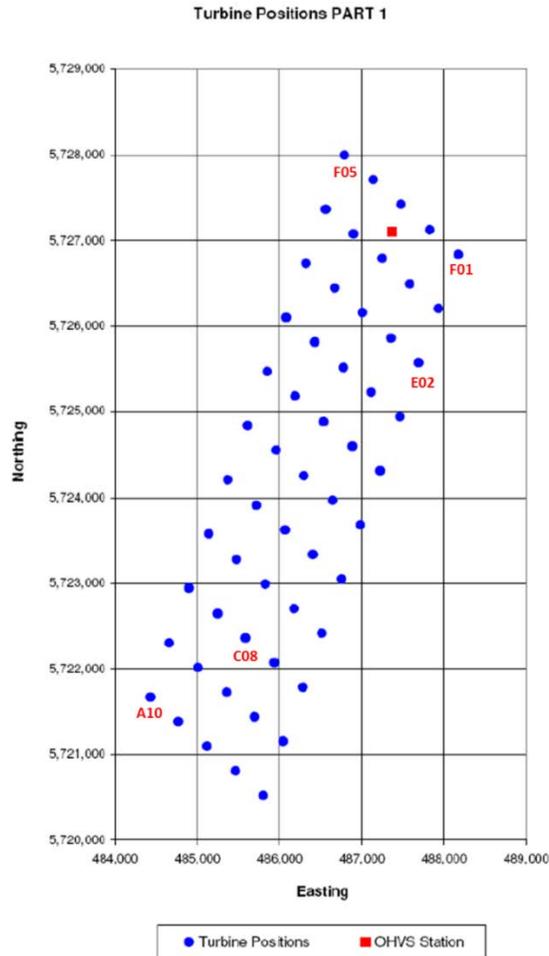
Figure 2.2 Layout of Belwind offshore wind farm and locations of boreholes

The subsurface consists of 15 to 20 m of very dense sand with shell fragments underlain by an overconsolidated clay with varying silt content. The following geotechnical investigations were carried out:

1. Cone penetrometer (CPT) tests at 24 locations
2. Soil borings at 5 locations (A10, C08, E02, F01, F05 in Figure 2.2) with standard penetration test (SPT) sampling in the sand and driven tube sampling in the clay
3. Laboratory index property tests
4. Laboratory UU triaxial compression tests on clay samples

These geotechnical investigation results were used to establish design parameters for the soil at different turbine locations: unit weight, friction angle for sand, and undrained shear strength for clay versus depth.

The structural design information includes analyses of the loads and estimates of the first order resonant frequency for each foundation structure. The field performance monitoring information consists of summary information about loads and responses, including the first and second order resonant frequencies versus time.

2.2 Northwind Offshore Wind Farm

The Northwind Offshore Wind Farm is located 40 km off the Belgian coast (Figure 2.3). It consists of 72 3-MW WTG structures with one offshore high-voltage substation (OHVS) (Figure 2.4) that were installed in 2014. The 72 WTG locations were divided into nine clusters based on water depth and soil conditions (Table 2.1).

Figure 2.3 Location of Northwind offshore wind farm

Figure 2.4 Layout of Northwind wind farm and locations of boreholes

Table 2.1 Clusters in wind farm and applied soil profile (Northwind)

Cluster	Max. DSBL (m LAT)	Min. DSBL (m LAT)	No. Of WTGs	WTG ID.
1	-17.9	-17.9	1	F06
2	-18.5	-19.9	8	F05, G02, G03, G05, G06, H01, H05 and H06
3	-20.0	-20.8	11	A01, A02, B01, C01, G01, G04, G07, G08, H02, H03 and H07
4	-21.0	-22.0	13	A03, A04, A05, A07, B02, B03, F01, F02, F08, F09, H04, H08 and H09
5	-22.3	-23.0	10	A06, A08, A09, B07, E06, E09, F03, F07, F10 and G09
6	-22.6	-24.3	9	B04, B06, C02, D01, E01, E04, E05, E07 and F04
7	-25.1	-25.8	9	B05, C03, C07, D02, D08, D09, E02, E03 and E08
8	-26.1	-27.7	9	C04, C05, C06, C08, D03, D04, D05, D06 and D07
9	-28.9	-28.9	2	C09 and C10

The subsurface consists of 15 to 20 m of dense to very dense sand containing localized gravel underlain by stiff to very stiff clay. Rows 11 and 12 have a stratum of stiff to very stiff clay within the dense to very dense sand at approximately 13-17.5 m below the surface. The following geotechnical investigations were carried out:

1. 79 piezocone penetration tests (PCPTs) measuring net cone resistance, total cone resistance, friction ratio, and excess pore-water pressure ratio
2. 8 soil borings (BH 1.01, 1.03, 3.01, 5.03, 8.02, 8.03, 11.07, 12.01 in Figure 2.4) with SPT sampling in the sand, driven tube sampling in the clay, and down-the-hole (DTH) CPT tests in 6 of the boreholes
3. Laboratory index property tests
4. Laboratory UU and CU triaxial compression tests on clay samples

These geotechnical investigation results were used to establish design parameters for the soil at different turbine locations: unit weight, friction angle for sand, and undrained shear strength for clay versus depth.

The structural design information includes analyses of the loads and estimates of the first order resonant frequency for each foundation structure. The field performance monitoring information consists of summary information about loads and responses, including the first and second order resonant frequencies.

2.3 Analysis of the Monitoring Data of Resonance Frequencies

With knowledge of the in-situ soil conditions and the dimensions of the wind turbines, the resonance frequencies for the first and second order mode for each wind turbine at Belwind Offshore Wind Farm and Northwind Wind Farm were calculated. The design reports of the two wind farms provided the designed first order resonance frequencies but did not include the designed second order resonance frequencies. A self-design computer model was used to calculate the second order resonance frequencies and incorporated the following objectives:

- Compare the first and second resonance frequencies from the in-situ measurement to those stated in the design reports
- Conduct a sensitivity analysis to determine the impact soil stiffness has on resonance frequencies using the self-design computer model
- Estimate the interested displacement of the monopile at mudline using p-y method with stronger soil stiffness under service load

2.3.1 Modeling Resonance Frequency

In order to calculate the designed second order resonance frequency not given in the report and investigate the sensitivity of the influence of the stiffness of the sand, a computer model was built following the report of resonance frequency calculation and written in the computer language Python and included as Appendix C. The similar simplified computer model was also used by Middelweerd (2017).

The computer model consists of two parts: the wind turbine structure and the soil-structure interaction model. The wind turbine structure consists of the nacelle and rotor, tower, transition piece, items on transition piece, and monopile. The soil-structure interaction is modeled as horizontal springs based on p-y method developed by the API procedures; resistance at the tip is neglected due to the small lateral displacements under service loading – see Section 3.4.5.4). The computer model is a 1-D model of the wind turbine simplified as an Euler-Bernoulli beam model (Figure 2.5). The 1-D Euler-Bernoulli beam model is divided into multiple elements and the mass of the appurtenances are modeled as a lumped mass. The linear springs are modeled as p-y curves determined by the characteristics of the soil layers.

p-y Curves for Sand

API RP 2GEO (2011) gives the sand p-y curves for both short-term static loading and for cyclic loading. At a given depth, the equation giving the smallest value of ultimate resistance should be used as the ultimate bearing capacity:

$$p_{us} = (C_1 z + C_2 D) r' z \qquad (2.1)$$

$$p_{ud} = C_3 D r' z \qquad (2.2)$$

Where, p_u is the ultimate resistance (force/unit length); r' is the submerged soil unit weight; z is the length below the original seafloor; ϕ' is the angle of internal friction of sand; D is the pile outside diameter. C_1, C_2, C_3 are the coefficient determined as function of ϕ' (Figure 2.6).
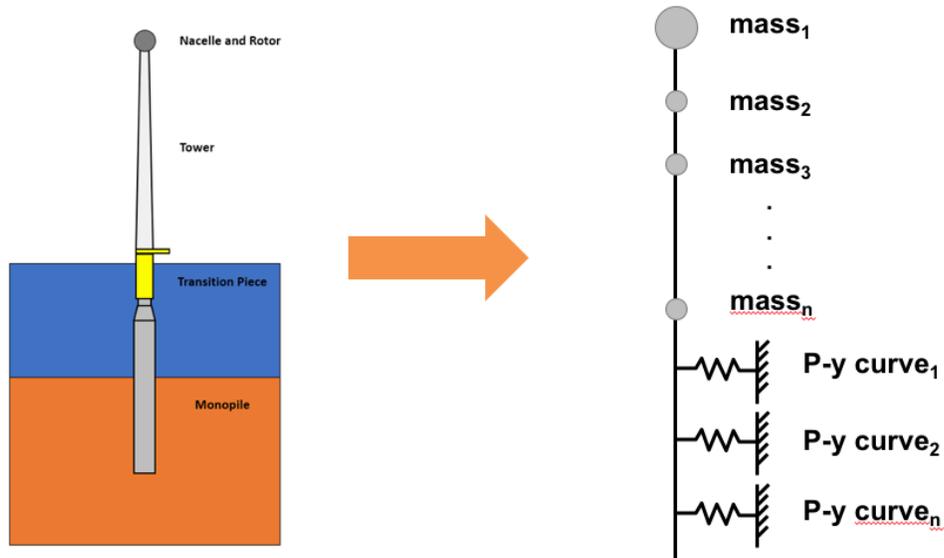
Figure 2.5 Simplified computer model of offshore wind turbine
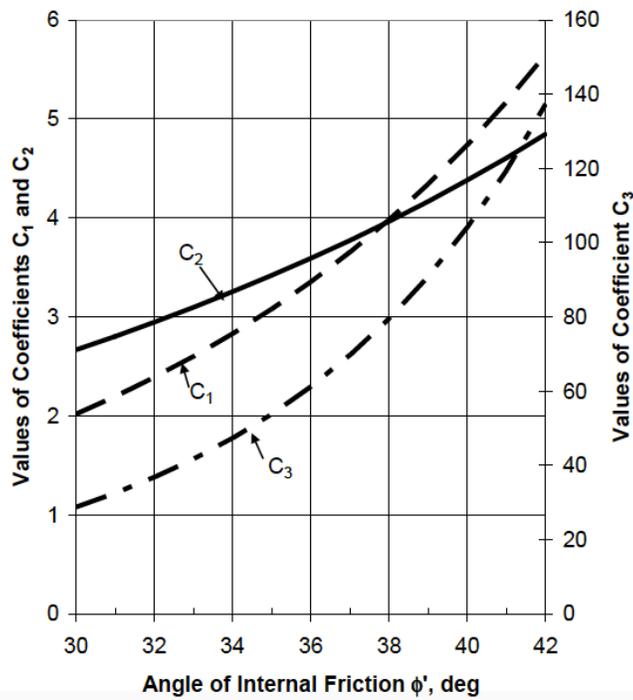
Figure 2.6 Coefficients C_1, C_2, C_3 as function of ϕ' (API RP 2GEO I 2011)

The p-y curves for sand is defined as non-linear and approximated at any specific depth x by the following expression:

$$p = Ap_u \tanh\left(\frac{kx}{Ap_u}y\right) \qquad (2.3)$$

where,

A is the factor to account for cyclic or static loading condition, evaluated by

$$A = 0.9 \text{ for cyclic loading}$$

$$A = (3.0 - 8.0\frac{Z}{D}) \geq 0.9 \text{ for static loading;}$$

p_u is the ultimate lateral resistance at depth z;

k is the rate of increase with depth of initial modulus of subgrade reaction, see Figure 2.7;

y is the lateral deflection at depth z;

z is the depth below the original sea seafloor.
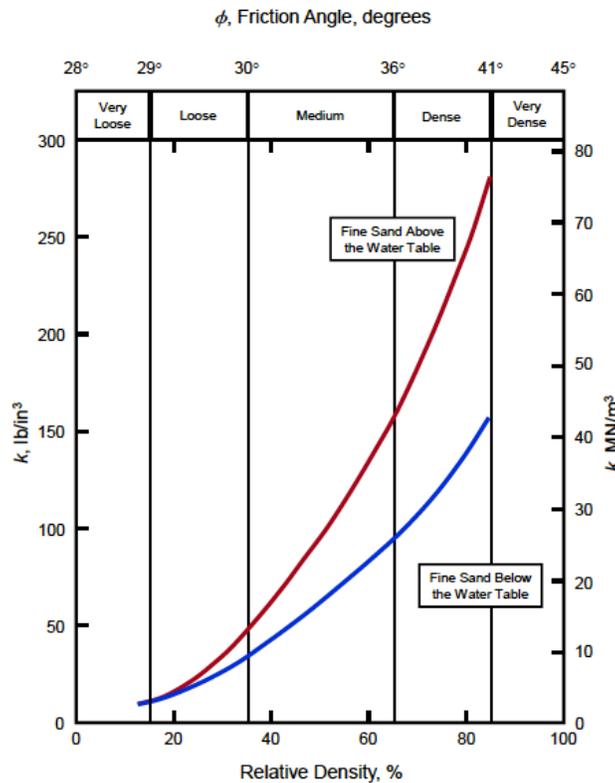
Figure 2.7 Value of k for API sand procedure (Isenhower and Wang 2018)

Scour Protection

The scour protection is post-installed by dumping the scour protection material in a developed scour hole. From the geotechnical report, a scour hole of 6 m is assumed based on the large variation in water depth during the life-time. The internal friction of the scour protection material is assumed to be either 40°

(lower design case) and 45° (upper design case). In the prediction of resonance frequency, the lower design case is used for the offshore wind turbines at Belwind.
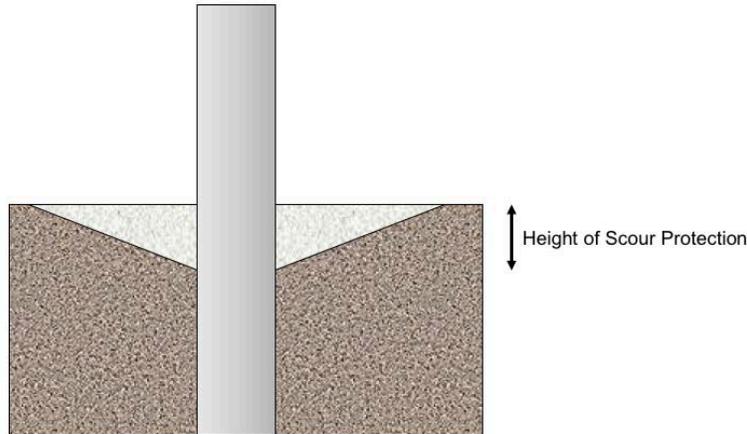
Figure 2.8 Sketch of the post-installed scour protection

Contained Mass

The analysis of the resonance frequency needs to take the mass of water and soil into account for the hollow structures submerged in the water and driven into soil. The contained mass includes the mass of the sea water and the soil contained inside the monopile. Equation (2.4) is the expression to evaluate the contained mass for each element in 1-D Euler-Bernoulli beam model.

$$m_{contained} = \rho \pi d^2 \Delta l / 4 \tag{2.4}$$

where, ρ is the density of the seawater or soil; d is the internal diameter of the monopile; and Δl is the length of the divided element.

Model Verification

For verification purposes, the predicted first order resonance frequencies from our computer model are compared to the resonance frequencies provided in the design reports (Table 2.2). The predicted resonance frequency from our model have a good agreement with the resonance frequency in the design reports.

Table 2.2 Comparison of first order resonance frequency (Belwind)

Wind Turbine #	Report (Hz)	Computer Model (Hz)	Difference (%)
A10	0.332	0.336	1.2%
B02	0.352	0.344	2.2%
C01	0.346	0.346	0.0%
D02	0.351	0.348	0.8%
E03	0.335	0.340	1.5%

2.3.2 Analysis of Belwind Offshore Wind Farm

Weijtjens and Deviendt (2017) published the monitoring data on the resonance frequencies of wind turbine C01 at Belwind from 2012 to 2016. Figure 2.9 shows the evolution of the first order resonance frequency over the five periods (2012 to 2016) of operational conditions. Based on the figure, the first order resonance frequency is slightly stiffening over time. The range of the measured first order resonance frequency is from 0.358 Hz to 0.375 Hz.
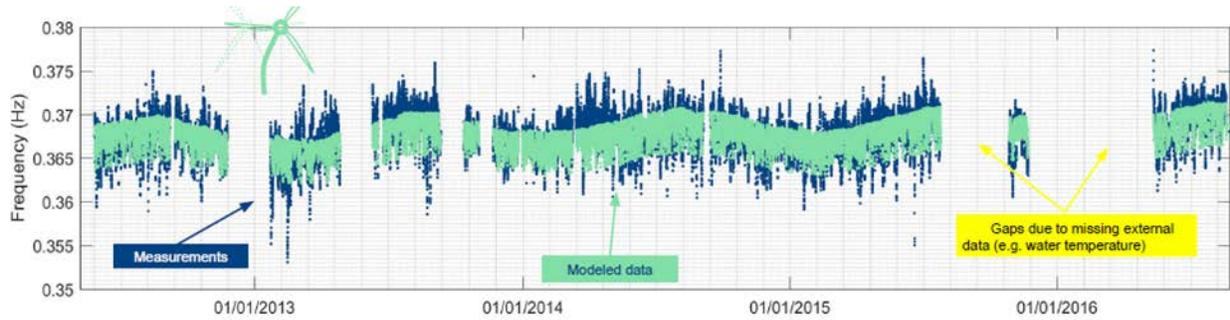
Figure 2.9 Measured first order resonance frequency at Belwind (Weijtjens and Deviendt 2017)

Figure 2.10 shows the evolution of the second order resonance frequency over 5 periods (2012 to 2016) of parked conditions. The second resonance frequency is stiffening significantly over time. The range of the second resonance frequency in 2012 is from 1.42 Hz to 1.5 Hz and in 2014 is from 1.47 Hz to 1.52 Hz. Figure 2.11 indicates that over the course of 4 years the second resonance frequency has increased with 0.05 Hz or 3%.
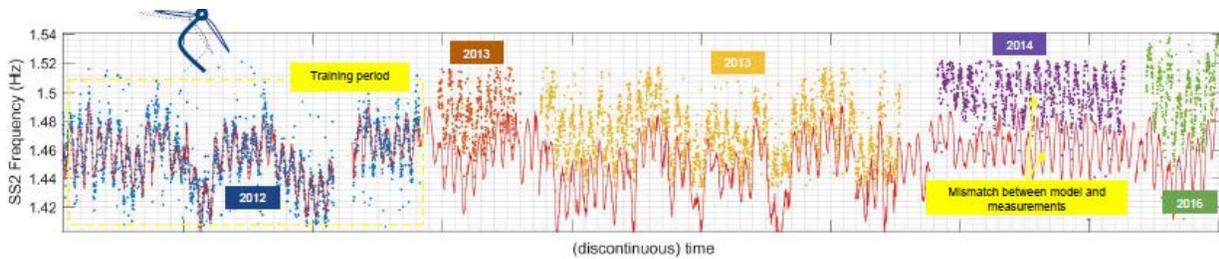
Figure 2.10 Measured second order resonance frequency at Belwind (Weijtjens and Deviendt 2017)
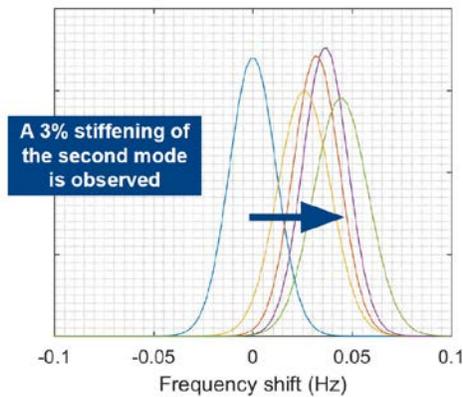
Figure 2.11 Frequency shift of the second order resonance frequency at Belwind (Weijtjens and Deviendt 2017)

Figure 2.12 compares the first order resonance frequency between the prediction from the design report and the in-situ measurements for each wind turbine. Position C01 is where the wind turbine equipped with multi-physics sensors and has been measured for years. The figure shows that the predicted first order resonance frequencies of most wind turbines are below the monitoring range.
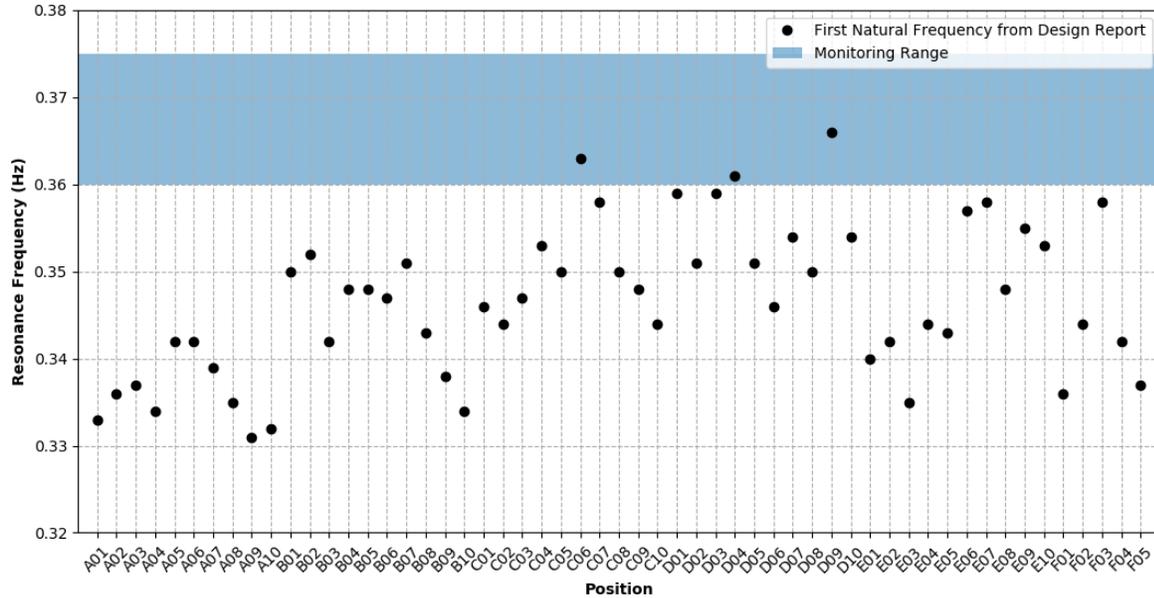
Figure 2.12 First order resonance frequencies from design and in-situ measurement at Belwind

The second order resonance frequencies were calculated by our computer model for five wind turbines. Beside the measured wind turbine C01, four other wind turbines were randomly picked to calculate their second order resonance frequencies. Figure 2.13 shows the comparison between the calculated and measured second order resonance frequencies. The figure indicates that the second order resonance frequencies are also underestimated in the design stage compared to the monitoring.
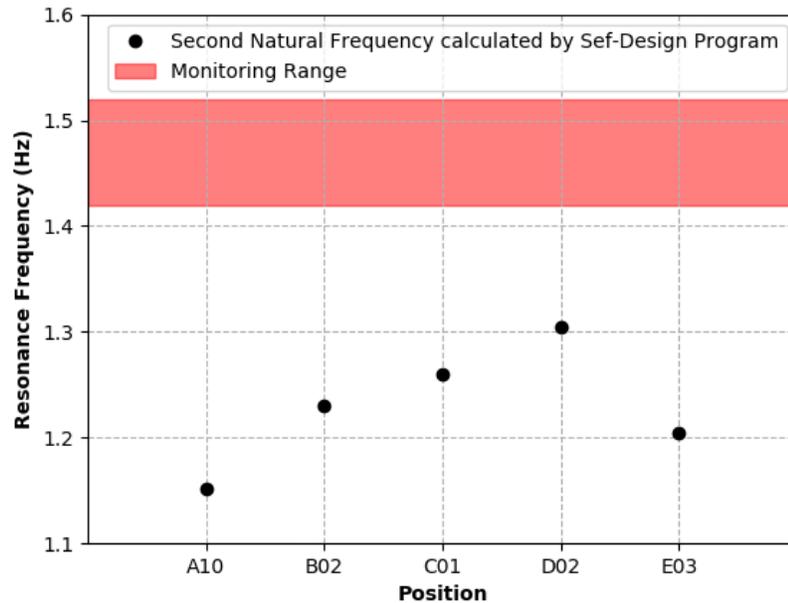
Figure 2.13 Second order resonance frequencies from design and in-situ measurement at Belwind

2.3.3 Analysis of Northwind Offshore Wind Farm

The monitoring report includes the measured first order resonance frequencies from multiple wind turbines at Northwind Offshore Wind Farm over two periods (2014 to 2015). The range of the measured first order resonance frequency is from 0.275 Hz to 0.307 Hz. The maximum frequency of the 1P harmonic is at 0.24 Hz, which indicates that the measured first order resonance frequencies are well above the 1P frequency.

The monitoring report also includes the evolution of the measured second order resonance frequencies from 2014 to 2015. The mean value of the second order resonance frequencies increases from 1.718 Hz in 2014 to 1.722 Hz in 2015. While not significant yet, the slight increasing trend in the monitoring hints that the long-term behavior of the Northwind turbines is similar to the behavior of the Belwind turbines.

Figure 2.14 shows a comparison between the predicted and measured first order resonance frequencies. The 72 wind turbine generators in Northwind are divided into nine clusters based on water depth and soil conditions, and one design is determined for each cluster. The figure shows that the predicted first order resonance frequencies from the design reports are all lower than the in-situ measurements.
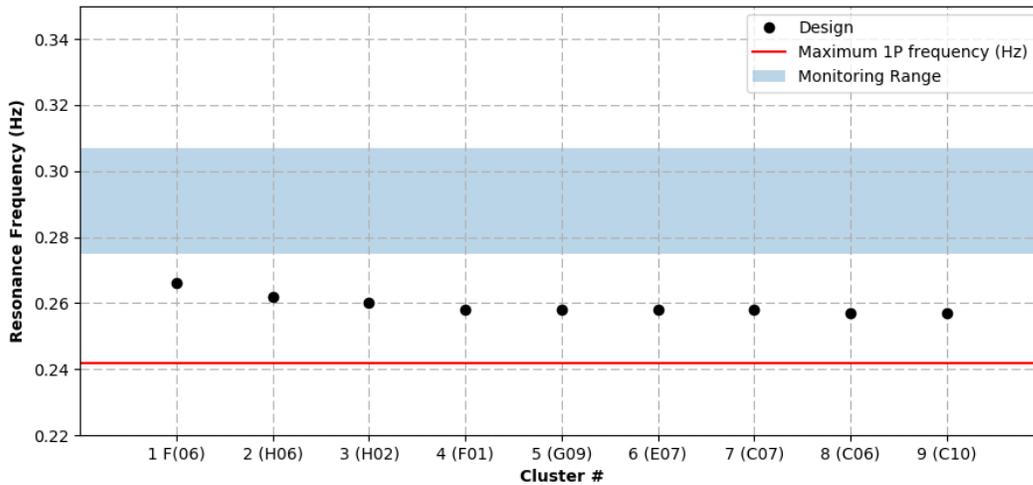
Figure 2.14 First order resonance frequencies from design and monitoring reports at Northwind

2.3.4 Influence of Sand Stiffness on Resonance Frequencies

Our computer model was used to analyze the influence of the soil stiffness had on the first and second order resonance frequencies. The stiffness of the sand was controlled by the coefficient of the lateral soil reaction, k, which was determined by the internal friction angle of the sand. In this analysis, k was multiplied by an amplified coefficient to investigate the influence of the soil stiffness on the resonance frequencies. Wind turbines A10, B02, C01, D02, and E03 at Belwind were chosen to be analyzed. The results show that the resonance frequencies increase with increasing stiffness of the sand the influence is larger for the second order resonance frequency than the first order resonance frequency.

Figure 2.15 shows in the influence of the soil stiffness on the first order resonance frequency of wind turbines at Belwind. The first order resonance frequencies increase with increasing sand stiffness. For the amplified coefficient from one to ten, the first order resonance frequency of wind turbine C01 changes from 0.346 Hz to 0.362 Hz, an approximate 4.6% increase. When the amplified coefficient approaches seven, the first order resonance frequency of wind turbine C01 reaches the lower bound of the measurement.

Figure 2.16 shows the influence of the soil stiffness on the second order resonance frequency of wind turbines at Belwind. For the amplified coefficient from one to ten, the second order resonance frequency of wind turbine C01 changes from 1.26 Hz to 1.415 Hz, an approximate 12.6% increase. When the amplified coefficient approaches seven as same for the first order resonance frequency, the second order resonance frequency of wind turbine C01 reaches the lower bound of the measurement.
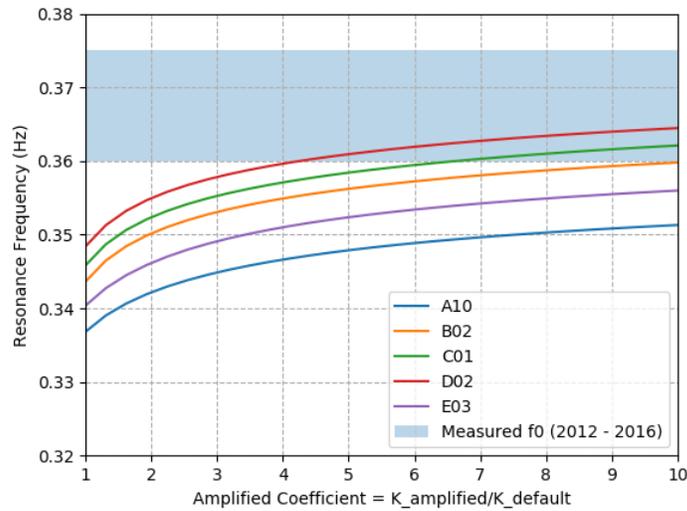
Figure 2.15 Influence of the sand stiffness on first order resonance frequency at Belwind
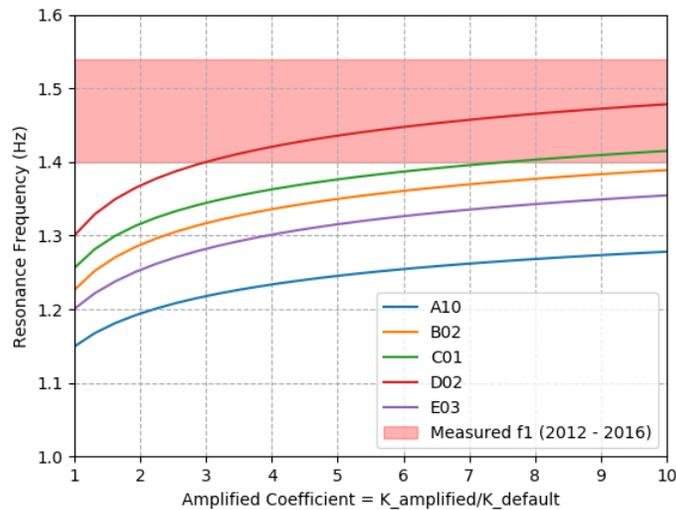
Figure 2.16 Influence of the sand stiffness on second order resonance frequency at Belwind

Table 2.3 summarizes the influence of the stiffness on resonance frequencies of wind turbines at Belwind. The increasing stiffness of the sand increases the predicted resonance frequencies of the offshore wind turbines and makes them closer to the measured resonance frequencies. The change of the stiffness of the sand has a larger influence on the second order resonance frequency than the first order resonance frequency.

Table 2.3 Influence of the stiffness of the sand on the resonance frequencies

	$F0\ (Hz)$ $K_{amp} = 1.0$	$F0\ (Hz)$ $K_{amp} = 10.0$	$Increment$	$F1\ (Hz)$ $K_{amp} = 1.0$	$F1\ (Hz)$ $K_{amp} = 10.0$	$Increment$
A10	0.336	0.351	4.3%	1.149	1.278	11.2%
B02	0.343	0.359	4.7%	1.226	1.388	13.2%
C01	0.346	0.362	4.7%	1.256	1.415	12.6%
D02	0.348	0.364	4.6%	1.300	1.478	13.7%
E03	0.340	0.356	4.6%	1.200	1.354	12.8%
$F0$: First order Resonance Frequency $F1$: Second order Resonance Frequency $Increment$: $(F_{K=10.0} - F_{K=1.0})/F_{K=1.0} * 100\%$						

2.3.5 Assessment of Lateral Displacement of Monopile at Mudline under Service Loading

The displacement of the monopile at mudline under service loading was estimated with the p-y method by using a stronger stiffness of the sand obtained from the previous analysis on the resonance frequencies. According to the results in the previous sections, the more realistic stiffness of the sand was around seven times the design value determined by the internal friction angle of sand based on API p-y method.

The monopile for wind turbine C01 was simplified to be 5 m diameter, 20 m length, and 0.06 m wall thickness. In the design report, the mean overturning moment was 30,000 kN-m and the mean horizontal force was 310 kN for an operating wind turbine with wind and wave load based on wind speed 12m/s. The soil profile was assumed to be uniform. The unit weight of the sand was 10 kN/m³. The friction angle of the sand was 40 degrees. The coefficient of the lateral soil reaction k was multiplied by seven to make the first order and second order resonance frequency reaching the measured range. The coefficient of the lateral soil reaction equaled to 290,000 kN/m³ in this p-y analysis.

The predicted displacement of the monopile at mudline is 0.0019 m under the service load combination. The normalized displacement is 0.04% of the diameter of the pile. The result indicates the importance of finding an optimal method to measure the stiffness of the sand under small displacement and developing an advanced methodology to apply the small-displacement stiffness on the p-y methods.

2.4 Conclusions

The following major conclusions can be drawn from these analyses using linear springs to model the soil-structure interaction:

1. The comparison of measured and designed values of resonance frequencies for wind turbines at Belwind and Northwind illustrates that the resonance frequencies have been under-predicted in design.
2. The measured resonance frequencies of wind turbines increase with time. The increase in second order resonance frequency is more obvious than the increase in first order resonance frequency.

3. Increasing the stiffness of the sand has a larger influence on the second order resonance frequency than on the first order resonance frequency.
4. The calculated resonance frequencies of wind turbines increase with the assumed stiffness of the sand. The results of this study (Table 2.3) demonstrate that the resonance frequency predictions are sensitive to an accurate evaluation of the pile-soil stiffness and that the subgrade modulus (k) value used in design needs to be increased by more than five times to match the field observations.
5. The predicted lateral displacement at the pile head for these monopiles under service loading (using the calibrated model to match field measurements) is less than 0.05% of the pile diameter.

3 Numerical Modeling

This section provides information about the numerical model being proposed to predict the dynamic response of monopiles in sand. The model was applied to the field lateral load tests that were conducted on Mustang Island in 1967. The tests conducted on Mustang Island formed the original basis for the sand p-y curves in the current design practice.

3.1 Soil Dynamic Models

A soil constitutive model of sand is proposed in this research based on the theory of dynamic soil behavior. According to the observations of soil dynamic behavior, the stiffness of the sand increases with the confining pressure and decreases non-linearly with increasing shear strain. As can be seen in Figure 3.1, the normalized shear modulus G/G_{max} vs. shear strain γ relationship of sand is separated into four strain ranges: (1) linear, (2) nonlinear elastic, (3) moderately nonlinear, and (4) highly nonlinear parts. The relationship can be referred to as degradation curve of shear stiffness.
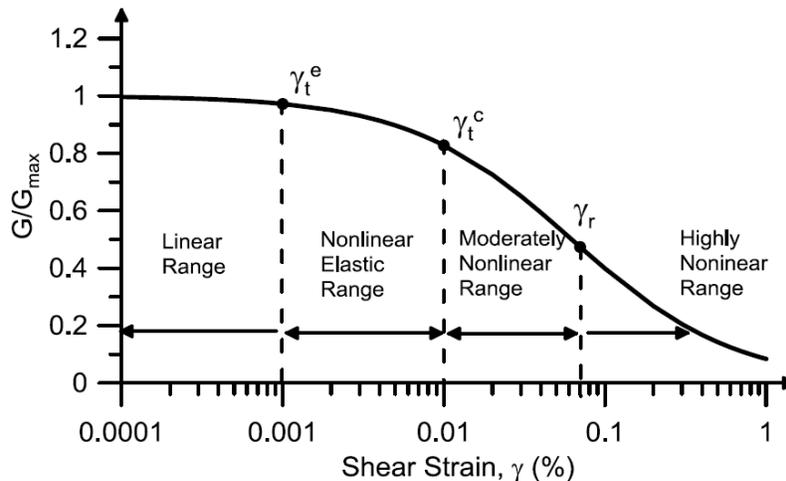
Figure 3.1 $G/G_{max} - log\ \gamma$ curve with the linear, nonlinear elastic, moderately nonlinear, and highly nonlinear ranges (PLAXIS Material Manual)

In the linear range, the shear modulus, G, is independent of the value of the shear strain, γ_t^e, and G is denoted as G_{max}. An elastic threshold value of shear strain, γ_t^e, is defined to represent the shear strain value beyond which the stress-strain response becomes strain-dependent. Above γ_t^e, G decreases with increase in shear strain and the stress-strain relationship is nonlinear. In the nonlinear elastic range, dynamic laboratory testing methods, such as the torsional shear and resonant column tests, allow the investigation of linear and nonlinear behavior of granular soils over a wide range of shear strains.

The well-known soil constitutive model, Mohr-Coulomb model, is a simple and well-known linearly-elastic perfectly-plastic model. In general, the parameters of the linear elastic part of the Mohr-Coulomb model are obtained by conventional soil tests in which the soil stiffness is often decreased to less than half its initial value. The proposed soil constitutive model captures the change of stiffness with the change of confining pressure and the shear strain.

The following sections represent four different models to represent the non-linear stiffness of sand: Menq (2003), Hardin and Drnevich (1972), Ishibashi (1993), and Santo and Correla (2001).

3.1.1 Menq (2003)

To calculate the shear modulus, G, the small-strain shear modulus G_{max} and the normalized shear modulus degradation curve G/G_{max} must be known for a level of shear strain, γ. A series of studies were conducted by Menq (2003) at The University of Texas at Austin to provide the empirical equations for G_{max} and G/G_{max}.

3.1.1.1 Small-Strain Shear Modulus, G_{max}

Menq (2003) studied the effects of mean effective stress, σ_0, void ratio, e, coefficient of uniformity, C_u, median grain size, D_{50}, water content, w and measurement frequency, f_m, on small-strain shear modulus. Menq (2003) found that the small-strain shear modulus, G_{max}, could be expressed as a function of the mean effective stress, σ_0, coefficient of uniformity, C_u, median grain size, D_{50} and void ratio, e. Also, his study demonstrated that the small-strain shear modulus, G_{max}, of granular soil at a mean effective confining pressure, σ_0, of one atmosphere, C_{G1}, was a function of void ratio, e, and gradation characteristics.

Menq (2003) proposed an expression of G_{max} as a function of the modulus at the mean effective confining pressure σ_0 of one atmosphere, C_{G1}, and a power of the normalized mean effective pressure as:

$$G_{max} = C_{G1} \left(\frac{\sigma_0}{P_a} \right)^{n_G}$$

(3.1)

$$C_{G1} = C_{G3} \times C_u^{b1} \times e^x$$

(3.2)

C_{G3} = 67.1 MPa

C_u = coefficient of uniformity

D_{50} = median grain size (in mm)

b1 = -2.0

e = void ratio

$x = -1 - (\frac{D_{50}}{20})^{0.75}$

n_G = $0.48 C_u^{0.09}$

3.1.1.2 Nonlinear Shear Modulus Reduction Curve

The modified hyperbolic model proposed by Darendeli (2001) was utilized herein to express the dynamic soil properties in terms of normalized shear modulus. Darendeli (2001) suggested the modified hyperbolic model as:

$$\frac{G}{G_{max}} = \frac{1}{1 + \left(\dfrac{\gamma}{\gamma_r}\right)^a} \tag{3.3}$$

where, γ_r = reference strain at $\dfrac{G}{G_{max}} = 0.5$,

      a = curvature coefficient, and,

      G = shear modulus at a shear strain value of γ.

Menq (2003) proposed the following relationships that can be used to estimate γ_r and a for nonplastic granular soil:

$$\gamma_r = 0.12 \times C_u^{-0.6} \times \left(\frac{\sigma_0}{P_a}\right)^{0.5 \times C_u^{-0.15}} \tag{3.4}$$

$$a = 0.86 + 0.1 \times \log(\frac{\sigma_0}{P_a}) \tag{3.5}$$

C_u = uniformity coefficient

σ_0 = effective confining pressure

P_a = atmospheric pressure

Because the shape of the G/G_{max} - $\log \gamma$ curve may need to be modified based on dynamic laboratory tests, the Equation (3.4) and (3.5) have following alternative formats:

$$\gamma_r = C_1 \times (\frac{\sigma_0}{P_a})^{C_2} \tag{3.6}$$

$$a = C_3 + C_4 \log(\frac{\sigma_0}{P_a}) \tag{3.7}$$

Parameters C_1, C_2, C_3, and C_4 provide more freedom to change the shape of the G/G_{max} - $\log \gamma$ curve.

3.1.2 Hardin & Drnevich (1972)

Hardin & Drnevich (1972) thought shear stress – strain relationship was the most important part for the critical soil properties. After they investigated the data from measurements of the shear modulus for a wide variety of clean sands and cohesive soils, they proposed a simple shear stress – strain relationship.

Hardin & Drnevich (1972) developed following expression for the shear stiffness in small strain:

$$G_{max} = 1230 \frac{(2.973-e)^2}{1+e} (OCR)^K \sigma_0^{1/2} \qquad (3.8)$$

where, e   = void ratio,

        OCR = overconsolidation ratio

        σ_0 = mean principal effective stress

Table 3.1 Value of K (Hardin & Drnevich 1972)

PI (Plasticity Index)	K
0	0
20	0.18
40	0.30
60	0.41
80	0.48
>=100	0.50

Hardin & Drnevich (1972) developed following expression for the nonlinearity of the soil:

$$\frac{G}{G_{max}} = \frac{1}{1+\gamma_h} \qquad (3.9)$$

$$\gamma_h = \frac{\gamma}{\gamma_r}[1 + ae_{xp}^{-b(\gamma/\gamma_r)}] \qquad (3.10)$$

$$\gamma_r = \frac{\tau_{max}}{G_{max}} \qquad (3.11)$$

$$\tau_{max} = \left\{ \left[\frac{(1+K_0)}{2} \sigma_v \sin\varphi + c\cos\varphi \right]^2 - \left[\frac{(1+K_0)}{2} \sigma_v \right]^2 \right\}^{1/2} \qquad (3.12)$$

where, K_0 = coefficient of lateral stress

        σ_v = vertical effective stress

        c and φ = static strength parameters in terms of effective stress

Table 3.2 Values of a and b (Hardin & Drnevich, 1972)

Soil type (1)	Modulus or damping (2)	Value of a (3)	Value of b (4)
Clean dry sands	Modulus	$a = -0.5$	$b = 0.16$
	Damping[b]	$a = 0.6(N^{-1/6}) - 1$	$b = 1 - N^{-1/12}$
Clean saturated sands	Modulus[b]	$a = -0.2 \log N$	$b = 0.16$
	Damping[b]	$a = 0.54(N^{-1/6}) - 0.9$	$b = 0.65 - 0.65N^{-1/12}$
Saturated cohesive soils	Modulus	$a = 1 + 0.25 \ (\log N)$	$b = 1.3$
	Damping	$a = 1 + 0.2(f^{1/2})$	$b = 0.2f\left(e_{xp}^{-\bar{\sigma}_0}\right) + 2.25\bar{\sigma}_0 + 0.3 \ (\log N)$

ª f is in cycles per second and $\bar{\sigma}_0$ is in kilograms per square centimeter.
b These values for modulus and damping of clean sands are for less than 50,000 cycles of loading. Beyond 50,000 cycles the damping begins to increase with number of cycles, possibly due to fatigue effects (2). The behavior of modulus for saturated sands beyond 50,000 cycles is not yet established.

3.1.3 Ishibashi (1993)

Ishibashi (1993) carried out and formulated many experimental investigations of soils for general use. Experimental data on dynamic shear moduli and damping ratio was available for various soils including non-plastic sands to highly plastic clays. In this report, only the development of shear moduli for sand of Ishibashi (1993) was introduced.

Ishibashi (1993) proposed the shear modulus (G) is generally expressed in the form:

$$G = K(\gamma)f(e)\sigma_0'^{m(r)} \tag{3.13}$$

Where, $K(\gamma)$ is a decreasing function of cyclic shear strain amplitude γ, and is unity at very small γ ($\leq 10^{-6}$), $f(e)$ is a function of void ratio e, σ_0' is the mean effective confining pressure, and power m(γ) is an increasing function of γ. G_{max}, the maximum dynamic shear modulus is the maximum value of G and is usually obtained at $\gamma = 10^{-6}$ or less. Therefore G_{max} is:

$$G_{max} = K_0 f(e)\sigma_0'^{m_0} \tag{3.14}$$

where, $K_0 = K(\gamma \leq 10^{-6}) = 1.0$, and,

$$m_0 = m(\gamma \leq 10^{-6}).$$

From Equation 3.13 and Equation 3.14, Ishibashi (1993) obtained:

$$\frac{G}{G_{max}} = K(\gamma)\sigma_0'^{m(\gamma)-m_0} \tag{3.15}$$

where,

$$K(\gamma) = 0.5\left[1 + \tanh\left\{\ln\left(\frac{0.000102}{\gamma}\right)^{0.492}\right\}\right] \tag{3.16}$$

$$m(\gamma) - m_0 = 0.272 \left[1 - \tanh \left\{ \ln\left(\frac{0.000556}{\gamma}\right)^{0.4} \right\} \right] \tag{3.17}$$

$K(\gamma)$ and $m(\gamma) - m_0$ values were regressed on experimental data for variant kinds of sand and developed specifically for $\sigma_0' = 1.0 kN/m^2$. σ_0' was the only parameter influencing the shape of the $G/G_{max} - log\gamma$ curve.

3.1.4 Santo & Correla (2001)

Santo & Correla (2001) proposed a key parameter called "threshold" shear strain ($\gamma_{0.7}$). This parameter was defined as the shear strain for a stiffness degradation factor of $G/G_o = 0.7$ in which G_o was the initial shear modulus for very small strain ($\gamma \approx 10^{-6}$) and G is the secant modulus of soil. The finite element software PLAXIS uses Santo & Correla (2001) in the Hardening Soil Model with Small-Strain Stiffness (HSSMALL) constitutive model to capture the nonlinearly of soil stiffness decay.

Santo & Correla (2001) suggested the following stiffness decay with respect to strain:

$$\frac{G}{G_0} = \frac{1}{1 + a\left|\frac{\gamma}{\gamma_{0.7}}\right|} \tag{3.18}$$

where, $a = 0.385$

In fact, using a = 0.385 and $\gamma = \gamma_{0.7}$ gives $G/G_0 = 0.722$. Hence, the formulation "about 70%" should be interpreted more accurately as 72.2%.

3.1.5 Comparison of Different Soil Dynamic Models

To investigate the precision of the different soil dynamic models, $G/G_{max} - \gamma$ curves predicted from the different soil dynamic models were compared to the curves measured in a soil dynamic laboratory. Two kinds of sand were used in comparison, one was the All-Purpose Sand purchased from Home Depot and sand collected from Mustang Island. The $G/G_{max} - \gamma$ curves were measured under two confining pressures of 4 psi and 16 psi for All-Purpose Sand and 3 psi and 12 psi for Mustang Island Sand.

Table 3.3 Characteristics of All-Purpose Sand

D50 (mm)	Void Ratio	Cu
0.67	0.37	4.6
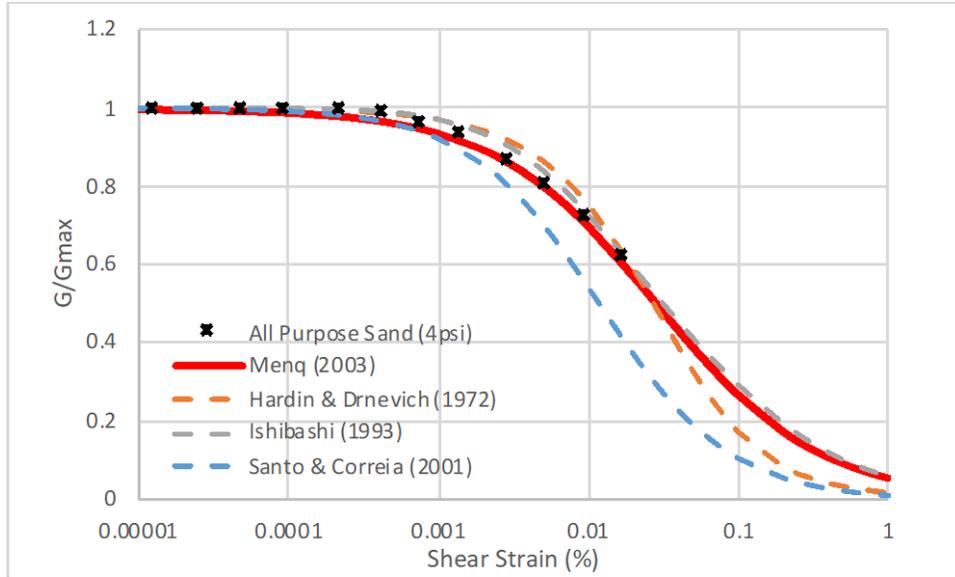
Figure 3.2 Comparison for All-Purpose Sand under 4 psi confining pressure
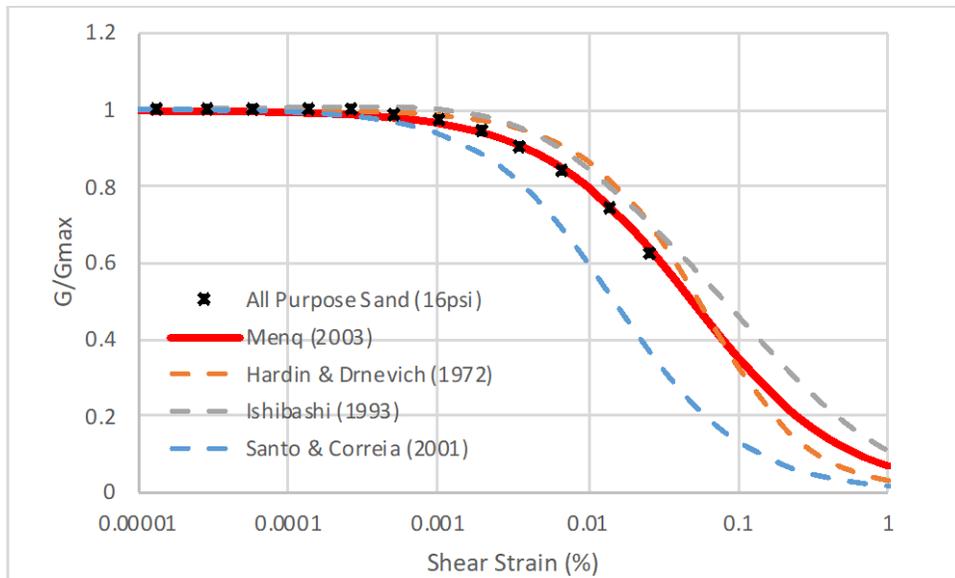
Figure 3.3 Comparison for All-Purpose Sand under 16 psi confining pressure

Table 3.4 Characteristics of Mustang Island Sand

D50 (mm)	Void Ratio	Cu
0.14	0.67	1.31
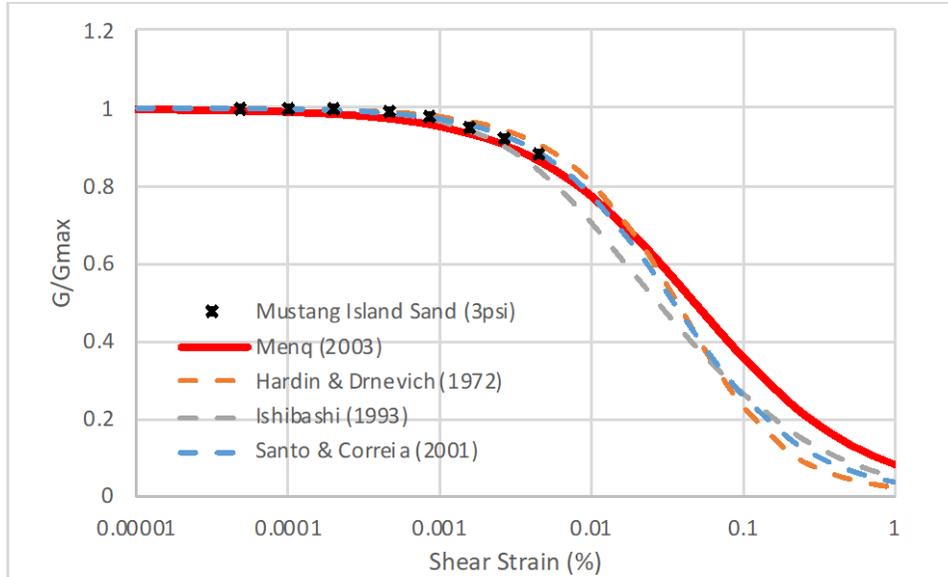
Figure 3.4 Comparison for Mustang Island Sand under 3 psi confining pressure
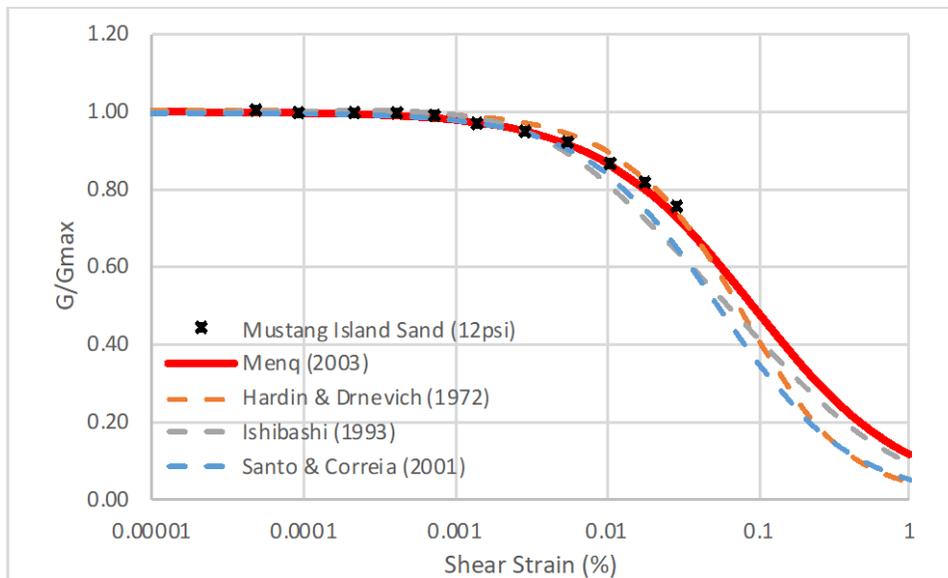
Figure 3.5 Comparison for Mustang Island Sand under 12 psi confining pressure

Figures 3.2 to 3.5 show that the dynamic soil model of Menq (2003) has the best fit with the measured $G/G_{max} - \gamma$ curves for different sand under different confining pressures. Menq (2003) matches well with the measured curve from the linear range to the moderately nonlinear range. Hardin & Drnevich (1972) has good fit with the measured curve in the linear elastic range, but it overestimates the normalized shear modulus from nonlinear elastic range to moderately nonlinear range and it underestimates the normalized shear modulus in highly nonlinear range. Ishibashi (1993) overestimates the shear stiffness for All-Purpose Sand and underestimates the normalized shear stiffness for Mustang Island sand. The deviation for Ishibashi (1993) was because Ishibashi (1993) used a regression curve for variant kinds of

sand with different uniformity coefficients. Santo & Correia (2001) has a good fit of the measured curve in the linear range, but it underestimates the normalized shear stiffness from nonlinear elastic range to highly nonlinear range. Therefore, the Menq (2003) approach provides the best fit to the measurements.

3.2 Development of the Soil Constitutive Model

This section presents the progress in developing the soil constitutive model. The soil constitutive model combines the form of the orthotropic material and the theory of Menq (2003). The soil constitutive model adds Masing's Rule to simulate the unloading and reloading behavior of the soil material.

3.2.1 Orthotropic

The soil constitutive model represents orthotropic linear elastic behavior and strain-induced anisotropy. An orthotropic linear elastic material is one that has three orthogonal planes of microstructural symmetry. The stiffness matrix has nine independent elastic constants:

$$
\begin{bmatrix} \sigma_{11} \\ \sigma_{22} \\ \sigma_{33} \\ \sigma_{23} \\ \sigma_{13} \\ \sigma_{12} \end{bmatrix} = \begin{bmatrix} C_{11} & C_{12} & C_{13} & & & \\ & C_{22} & C_{23} & & & \\ & & C_{33} & & & \\ & & & C_{44} & & \\ & & & & C_{55} & \\ & & & & & C_{66} \end{bmatrix} \begin{bmatrix} \varepsilon_{11} \\ \varepsilon_{22} \\ \varepsilon_{33} \\ 2\varepsilon_{23} \\ 2\varepsilon_{13} \\ 2\varepsilon_{23} \end{bmatrix} \tag{3.19}
$$

Expressing the coefficients C_{ij} in terms of Young's modulus, E, Poisson's ratio, ν, and shear modulus, G, these equations can be inverted:

$$
\begin{bmatrix}
\varepsilon_{11} \\
\varepsilon_{22} \\
\varepsilon_{33} \\
2\varepsilon_{23} \\
2\varepsilon_{13} \\
2\varepsilon_{12}
\end{bmatrix}
=
\begin{bmatrix}
\dfrac{1}{E_1} & -\dfrac{v_{21}}{E_2} & -\dfrac{v_{31}}{E_3} & & & \\
-\dfrac{v_{12}}{E_1} & \dfrac{1}{E_2} & -\dfrac{v_{32}}{E_3} & & & \\
-\dfrac{v_{13}}{E_1} & -\dfrac{v_{23}}{E_2} & \dfrac{1}{E_3} & & & \\
& & & \dfrac{1}{G_{23}} & & \\
& & & & \dfrac{1}{G_{13}} & \\
& & & & & \dfrac{1}{G_{12}}
\end{bmatrix}
\begin{bmatrix}
\sigma_{11} \\
\sigma_{22} \\
\sigma_{33} \\
\sigma_{23} \\
\sigma_{13} \\
\sigma_{12}
\end{bmatrix}
\tag{3.20}
$$

The nine independent constants are:

E_i is Young's modulus of the material in direction $i = 1,2,3$; for example, $\sigma_{11} = E_1\varepsilon_{11}$ for uniaxial tension in the direction 1.

v_{ij} is Poisson's ratio representing the ratio of transverse strain to the applied strain in uniaxial tension; for example, $v_{12} = -\varepsilon_{22}/\varepsilon_{11}$ for uniaxial tension in direction 1.

G_{ij} are the shear moduli representing the shear stiffness in the corresponding plane; for example, G_{12} is the shear modulus for shearing in the $1-2$ plane.

From the symmetry of the stiffness matrix,

$$
v_{23}E_3 = v_{32}E_2, \quad v_{13}E_3 = v_{31}E_1, \quad v_{12}E_2 = v_{21}E_1
$$

If we assume that all values of Poisson's Ratio are equal to, say, v,

$$
E_1 = E_2 = E_3 = E
$$

The compliance matrix can be written in simpler form in terms of five independent elastic constants:

$$
\begin{bmatrix} \varepsilon_{11} \\ \varepsilon_{22} \\ \varepsilon_{33} \\ 2\varepsilon_{23} \\ 2\varepsilon_{13} \\ 2\varepsilon_{12} \end{bmatrix} = \begin{bmatrix} \dfrac{1}{E} & -\dfrac{v}{E} & -\dfrac{v}{E} & & & \\ -\dfrac{v}{E} & \dfrac{1}{E} & -\dfrac{v}{E} & & & \\ -\dfrac{v}{E} & -\dfrac{v}{E} & \dfrac{1}{E} & & & \\ & & & \dfrac{1}{G_{23}} & & \\ & & & & \dfrac{1}{G_{13}} & \\ & & & & & \dfrac{1}{G_{12}} \end{bmatrix} \begin{bmatrix} \sigma_{11} \\ \sigma_{22} \\ \sigma_{33} \\ \sigma_{23} \\ \sigma_{13} \\ \sigma_{12} \end{bmatrix}
\tag{3.21}
$$

Substituting γ_{23} for $2 \cdot \varepsilon_{23} = \varepsilon_{23} + \varepsilon_{32}$, γ_{13} for $2 \cdot \varepsilon_{13} = \varepsilon_{13} + \varepsilon_{31}$ and γ_{12} for $2 \cdot \varepsilon_{12} = \varepsilon_{12} + \varepsilon_{21}$, Menq (2003) expresses the shear moduli as:

$$
\frac{G_{ij}}{G_{max}} = \frac{1}{1 + \left(\dfrac{\gamma_{ij}}{\gamma_r}\right)^a}
\tag{3.22}
$$

$$
G_{max} = C_{G3} \times C_u^{b1} \times e^x \times \left(\frac{\sigma_0}{P_a}\right)^{n_G}
\tag{3.23}
$$

$$
\sigma_0 = (\sigma_{11} + \sigma_{22} + \sigma_{33})/3
\tag{3.24}
$$

Poisson's ratio v can be assumed to be a reasonable constant value based on experience and experiment.

To obtain the relationship between Young's modulus, E, and Shear modulus, G, the octahedral shear strain is introduced into the model. The octahedral shear strain, γ_{oct}, is a measure of overall distortion:

$$
\Upsilon_{oct} = \frac{2}{3}\sqrt{(\varepsilon_{11} - \varepsilon_{22})^2 + (\varepsilon_{11} - \varepsilon_{33})^2 + (\varepsilon_{22} - \varepsilon_{33})^2 + 6(\varepsilon_{12}^2 + \varepsilon_{13}^2 + \varepsilon_{23}^2)}
\tag{3.25}
$$

Replacing γ_{ij} in equation (3.22) with γ_{oct}, we can calculate an "octahedral" shear modulus G_{oct}:

$$
\frac{G_{oct}}{G_{max}} = \frac{1}{1 + \left(\dfrac{\gamma_{oct}}{\gamma_r}\right)^a}
\tag{3.26}
$$

So, Young's modulus, E, can be estimated as:

$$
E = 2G_{oct}(1 + v)
\tag{3.27}
$$

To summarize, five independent elastic constants of the compliance matrix in Equation (3.21) can be calculated based on confining pressure and strain level.

The effective confining pressure, σ_0, must be positive in the equations proposed by Menq (2003). To avoid substitution of negative confining pressure in equation (3.23), the definition of the confining pressure, σ_0, should be modified. (Note that compression is assumed positive and tension negative.)
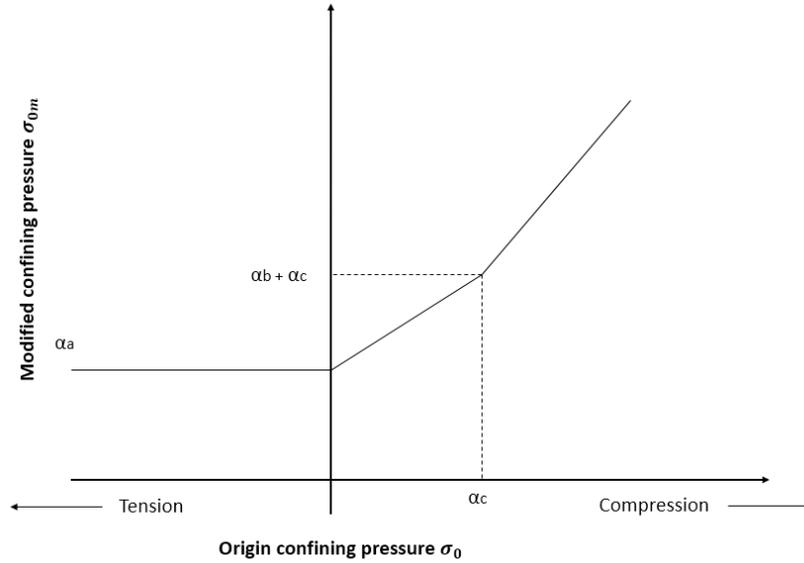
Figure 3.6 Relationship between origin and modified confining pressures

$$\sigma_{0m} = \begin{cases} \alpha_a & \text{for } \sigma_0 < 0 \\ \alpha_a + \dfrac{\alpha_b + \alpha_c - \alpha_a}{\alpha_c} \sigma_0 & \text{for } 0 \le \sigma_0 \le \alpha_c \\ \alpha_b + \sigma_0 & \text{for } \sigma_0 > \alpha_c \end{cases} \tag{3.28}$$

α_a, α_b, and α_c are the parameters necessary to control the relationship between σ_0 and σ_{0m}.

α_a is the parameter that maintains a low stiffness when the material is in tension. Also, it can prevent unrealistically small stiffness when the effective confining pressure is low, for example, near ground surface.

α_b is the parameter that prevents unrealistically small stiffness when the effective confining pressure is low.

α_c is the parameter allowing the σ_{0m} to change smoothly from tension to compression.

3.2.2 Masing's Rule

When subjected to cyclic shear loading, the soil constitutive model must be modified to show typical hysteretic behavior as depicted in Figure 3.7.
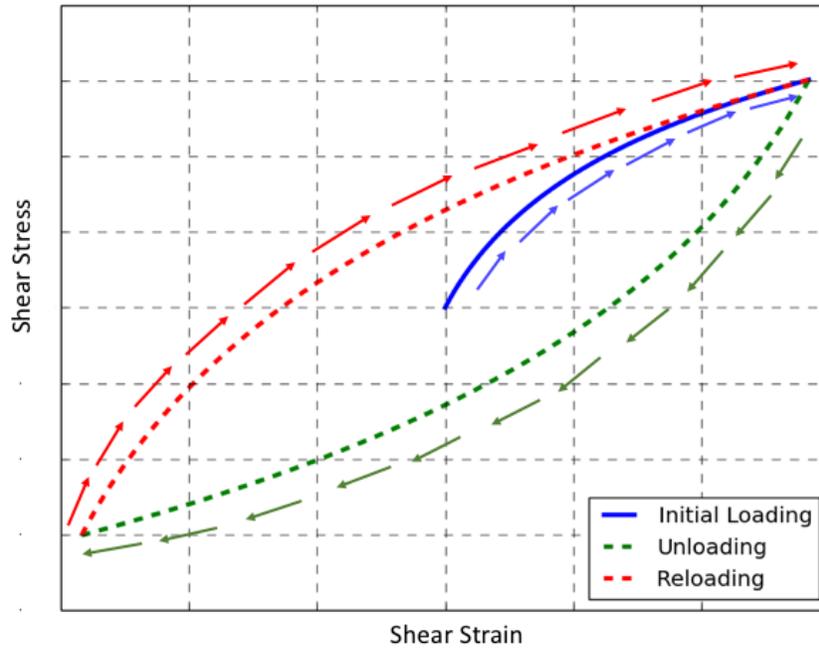
Figure 3.7 Hysteretic behavior of soil under cyclic shear loading

Starting from the small-strain shear stiffness, G_0 (G_{max}), the actual stiffness will decrease with increasing shear strain as shown in Figure 3.1. Upon load reversal, the stiffness will restart from G_0 and will decrease again until the next load reversal.

Masing (1926) described the hysteretic behavior of materials in unloading/reloading cycles according to the following rules:

- The shear modulus in unloading is equal to the initial tangent modulus of the loading curve.
- The shape of the unloading and reloading curves is the same as the shape of the loading curve, but the size in terms of stress is double. In terms of the above introduced threshold shear strain γ_r (Equation (3.4)) used in Equation (3.3), Masing's rule can be fulfilled by the following setting in the Hardin-Drnevich relation:

$$\gamma_{r\_un/re-loading} = 2\gamma_{r\_virgin-loading} \tag{3.29}$$

The hysteresis effect described in Masing's second rule can be easily incorporated in both models using the expression:

$$\varepsilon_0 - \varepsilon_R = f\left(\frac{\sigma_0 - \sigma_R}{L}\right) \tag{3.30}$$

with shape factor L = 1 in primary loading and L = 2 in unloading and reloading. In Equation (3.30), $f(\sigma)$ represents the monotonic stress-strain relationship $\varepsilon = f(\sigma)$. The strain and stress levels ε_0 and σ_0 denote the last load reversal point in stress-strain space, where ε_R and σ_R specify the current strain and stress, respectively. Masing's rule is just to simulate the stiffness of the model during unloading/reloading but not for calculating damping.

Lablance et al. (2010) did the cyclic load tests on the monopile in sand and indicated that the pile stiffness evolved approximately logarithmically with cyclic number. Lablance et al. (2010) suggested that the evolution of the pile stiffness can be approximately by

$$\tilde{k}_N = \tilde{k}_0 + A_k \ln(N) \tag{3.31}$$

Where A_k is a dimensionless constant; N is the number of cyclic; $\tilde{k}_0$ is the pile stiffness when cyclic number $N = 1$; $\tilde{k}_N$ is the pile stiffness after N cyclic.
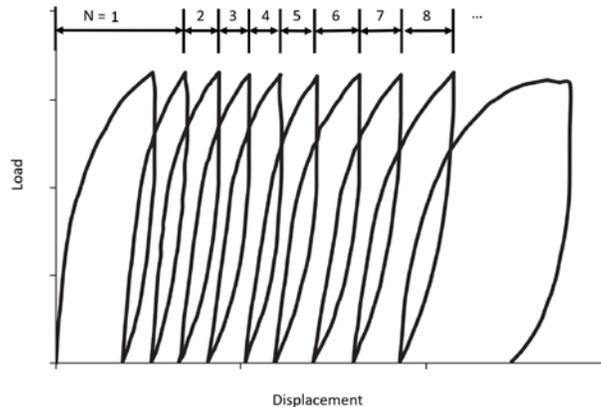
Figure 3.8 Number of cyclic loading

By imitating the format of the Equation (3.31), we can have Equation (3.32):

$$G_N = G_0 + A_G \ln(N) \tag{3.32}$$

Where A_k is a dimensionless constant; N is the number of cyclic; G_0 is the original maximum shear stiffness at the reversal point for each cycle; G_N is the stiffened maximum shear stiffness at the reversal point for each cycle. An additional term dependent on the number of cyclic '$\ln(N)$' is added on the original maximum shear stiffness to get the stiffened maximum shear stiffness for each cycle.

A further advancement of the constitutive model is needed to represent the change in volume, and therefore permanent displacement, associated with a change in stiffness. Work on this aspect of the constitutive model will continue after completion of this project.

3.3 Element Test

The element test is the verification and validation process of the soil constitutive model that makes use of triaxial, torsional shear test data readily available in the literature and in the laboratory tests. In the numerical element tests, the secant method and Newton-Raphson method are used as the root-finding algorithm to calculate the relationship between stress and strain. In the self-design python program, the numerical element tests are written and analyzed by the secant method. In Abaqus, the numerical element tests are written and analyzed by Newton-Raphson method. The results of the numerical element tests are compared with the measurements.

3.3.1 Second Method

In numerical analysis, the secant method is a root-finding algorithm that uses a succession of roots of secant lines to better approximate a root of a function f. The secant method is a finite difference approximation of Newton's method which serves as the basis of the incremental-iterative solution technique used in Abaqus/Standard. The recurrence relation defines the secant method:

$$x_n = x_{n-1} - f(x_{n-1}) \frac{x_{n-1} - x_{n-2}}{f(x_{n-1}) - f(x_{n-2})} = \frac{x_{n-2} f(x_{n-1}) - x_{n-1} f(x_{n-2})}{f(x_{n-1}) - f(x_{n-2})} \tag{3.33}$$

x is the root of the equation $f(x) = 0$ that is to be solved.

To find the root of the equation $f(x) = 0$, the secant method requires two initial values, x_0 and x_1, which should be ideally chosen to lie close to the root. As can be seen in Figure 3.8, a line is constructed though the points $(x_0, f(x_0))$ and $(x_1, f(x_1))$. The equation of the line is:

$$y = \frac{f(x_1) - f(x_0)}{x_1 - x_0} (x - x_1) + f(x_1) \tag{3.34}$$

And the solution be found by setting $y = 0$:

$$x = x_1 - f(x_1) \frac{x_1 - x_0}{f(x_1) - f(x_0)} \tag{3.35}$$

We then use the new value of x as x_2 and repeat the process using x_1 and x_2 instead of x_0 and x_1. We continue this process, solving for x_3, x_4, etc., until we reach an acceptable precision (a sufficiently small difference between x_n and x_{n-1}).
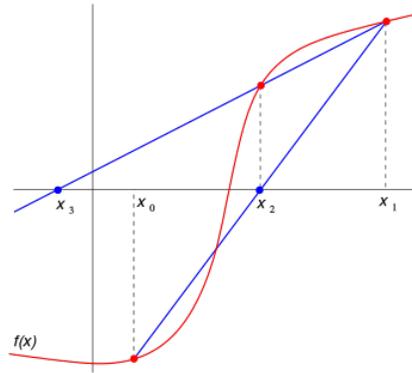
Figure 3.9 The first two iterations of the secant method

3.3.2 Element Test in Axial Direction

To find the deviatoric stress $\Delta\sigma$ corresponding to the applied deviatoric strain $\Delta\varepsilon$ in axial direction, we need to build the equilibrium function $f(\Delta\sigma) = 0$ for the axial loading element. The following explains the procedure to obtain the equilibrium function $f(\Delta\sigma) = 0$ to how to use the secant method to find the numerical solution for $\Delta\sigma$:

(1) Define the stress tensor and strain tensor at initial and final states. We assume the confining pressure at the initial state is σ_c, the deviatoric stress at the final state is $\Delta\sigma$, the deviatoric strain at the final state is $\Delta\varepsilon$, and the loading direction is along direction 2.

$$\text{initial stress tensor} = \begin{bmatrix} \sigma_{11} \\ \sigma_{22} \\ \sigma_{33} \\ \sigma_{23} \\ \sigma_{13} \\ \sigma_{12} \end{bmatrix} = \begin{bmatrix} \sigma_c \\ \sigma_c \\ \sigma_c \\ 0 \\ 0 \\ 0 \end{bmatrix} \tag{3.36}$$

$$\text{final stress tensor} = \begin{bmatrix} \sigma_{11} \\ \sigma_{22} \\ \sigma_{33} \\ \sigma_{23} \\ \sigma_{13} \\ \sigma_{12} \end{bmatrix} = \begin{bmatrix} \sigma_c \\ \sigma_c + \Delta\sigma \\ \sigma_c \\ 0 \\ 0 \\ 0 \end{bmatrix} \tag{3.37}$$

38

$$\text{initial strain tensor} = \begin{bmatrix} \varepsilon_{11} \\ \varepsilon_{22} \\ \varepsilon_{33} \\ \varepsilon_{23} \\ \varepsilon_{13} \\ \varepsilon_{12} \end{bmatrix} = \begin{bmatrix} 0 \\ 0 \\ 0 \\ 0 \\ 0 \\ 0 \end{bmatrix} \tag{3.38}$$

$$\text{final strain tensor} = \begin{bmatrix} \varepsilon_{11} \\ \varepsilon_{22} \\ \varepsilon_{33} \\ \varepsilon_{23} \\ \varepsilon_{13} \\ \varepsilon_{12} \end{bmatrix} = \begin{bmatrix} -v\Delta\varepsilon \\ \Delta\varepsilon \\ -v\Delta\varepsilon \\ 0 \\ 0 \\ 0 \end{bmatrix} \tag{3.39}$$

(2) Calculate Young's modulus E at the specified values of strain and stress. First, we know that the relationship between the deviatoric stress and strain is:

$$\Delta\sigma = E\Delta\varepsilon \tag{3.40}$$

For homogeneous isotropic materials, Young's modulus E is a function of the shear modulus G and Poisson's ratio v:

$$E = 2G(1+v) \tag{3.41}$$

Poisson's ratio v is a constant value. The shear modulus G can be obtained by re-writing Equation (3.26):

$$G = G_{\max} \frac{1}{1 + (\frac{\gamma_{oct}}{\gamma_r})^a} \tag{3.42}$$

Substitute Equation (3.42) and (3.41) into Equation (3.40) to obtain:

$$\Delta\sigma = 2G_{\max}(1+v)\frac{1}{1 + (\frac{\gamma_{oct}}{\gamma_r})^a}\Delta\varepsilon \tag{3.43}$$

(3) According to Equations (3.1), (3.4), (3.5), and (3.25), G_{max}, γ_r and a are the functions of mean effective stress σ_0 and γ_{oct} is the function of the strain tensor. The mean effective stress σ_0 can be obtained by the confining pressure σ_c and the deviatoric stress $\Delta\sigma$. The mean effective stress σ_0 must be modified by Equation (3.26). The deviatoric strain $\Delta\varepsilon$ is the known value to find the unknown value $\Delta\sigma$.

The mean effective confining pressure σ_0 at the final state is:

39

$$\sigma_0 = \sigma_c + \frac{\Delta\sigma}{3} \tag{3.44}$$

Equations (3.1), (3.4), (3.5) and (3.25) can be re-written in the simplified format:

$$G_{max} = \text{gmax}(\Delta\sigma) \tag{3.45}$$

$$\gamma_r = r(\Delta\sigma) \tag{3.46}$$

$$a = a(\Delta\sigma) \tag{3.47}$$

$$\gamma_{oct} = roct(\Delta\varepsilon) \tag{3.48}$$

Then, we substitute Equations (3.45), (3.46), (3.47) and (3.48) into Equation (3.43) and find:

$$\Delta\sigma = 2 \cdot \text{gmax}(\Delta\sigma) \cdot (1+v) \cdot \frac{1}{1 + (\frac{roct(\Delta\varepsilon)}{r(\Delta\sigma)})^{a(\Delta\sigma)}} \cdot \Delta\varepsilon \tag{3.49}$$

Because $\Delta\varepsilon$ is the known value, Equation (3.49) can be re-written in the simplified format:

$$\Delta\sigma = g(\Delta\sigma) \tag{3.50}$$

Then, the equilibrium function $f(\Delta\sigma) = 0$ can be written as:

$$f(\Delta\sigma) = g(\Delta\sigma) - \Delta\sigma = 0 \tag{3.51}$$

The numerical solution of $\Delta\sigma$ can be found using the secant method:

$$\Delta\sigma_n = \Delta\sigma_{n-1} - f(\Delta\sigma_{n-1})\frac{\Delta\sigma_{n-1} - \Delta\sigma_{n-2}}{f(\Delta\sigma_{n-1}) - f(\Delta\sigma_{n-2})} = \frac{\Delta\sigma_{n-2}f(\Delta\sigma_{n-1}) - \Delta\sigma_{n-1}f(\Delta\sigma_{n-2})}{f(\Delta\sigma_{n-1}) - f(\Delta\sigma_{n-2})} \tag{3.52}$$

3.3.3 Element Test in Shear Direction

In the torsional shear test, the confining pressure is constant while shear modulus G, calculated by Equation (3.42), is the secant shear modulus between shear strain and shear stress. Thus, the secant method is not needed to find the solution. The following describes how to obtain the relationship between the shear stress and shear strain in the torsional shear test:

(1) Define the stress tensor and the strain tensor at the initial and final states. Direction 13 is assumed as the shear direction.

$$\text{initial stress tensor} = \begin{bmatrix} \sigma_{11} \\ \sigma_{22} \\ \sigma_{33} \\ \sigma_{23} \\ \sigma_{13} \\ \sigma_{12} \end{bmatrix} = \begin{bmatrix} \sigma_c \\ \sigma_c \\ \sigma_c \\ 0 \\ 0 \\ 0 \end{bmatrix} \tag{3.53}$$

$$\text{final stress tensor} = \begin{bmatrix} \sigma_{11} \\ \sigma_{22} \\ \sigma_{33} \\ \sigma_{23} \\ \sigma_{13} \\ \sigma_{12} \end{bmatrix} = \begin{bmatrix} \sigma_c \\ \sigma_c \\ \sigma_c \\ 0 \\ \Delta\tau \\ 0 \end{bmatrix} \tag{3.54}$$

$$\text{initial stress tensor} = \begin{bmatrix} \varepsilon_{11} \\ \varepsilon_{22} \\ \varepsilon_{33} \\ \varepsilon_{23} \\ \varepsilon_{13} \\ \varepsilon_{12} \end{bmatrix} = \begin{bmatrix} 0 \\ 0 \\ 0 \\ 0 \\ 0 \\ 0 \end{bmatrix} \tag{3.55}$$

$$\text{initial stress tensor} = \begin{bmatrix} \varepsilon_{11} \\ \varepsilon_{22} \\ \varepsilon_{33} \\ \varepsilon_{23} \\ \varepsilon_{13} \\ \varepsilon_{12} \end{bmatrix} = \begin{bmatrix} 0 \\ 0 \\ 0 \\ 0 \\ \Delta\gamma \\ 0 \end{bmatrix} \tag{3.56}$$

(2) Calculate the shear modulus G based on Equation (3.41) using $\Delta\gamma$.

$$G = G_{max} \frac{1}{1 + (\dfrac{\Delta\gamma}{\gamma_r})^a} \tag{3.57}$$

(3) The shear stress will be:

$$\Delta\tau = G\Delta\gamma \tag{3.58}$$

41

3.3.4 Verification of Subroutine Written for Abaqus

The subroutine of the soil constitutive model written for Abaqus was tested under axial loading. The Newton-Raphson method was used by Abaqus to solve the equation iteratively and to find an approximate solution that minimizes residuals. The results solved by the subroutine of Abaqus were compared with the results solved by secant method written by Python.

As shown in Figure 3.10, an incremental prescribed axial displacement along the Y-direction with ultimate strain 0.01 was applied on the top four nodes with a $1 \times 1 \times 1$ geometry. The bottom face of the cube body was restrained from movement in the Y-direction. The faces on the X-Y plane were restrained from movement in the Z-direction. The faces on the Y-Z plane were restrained from movement in the X-direction.
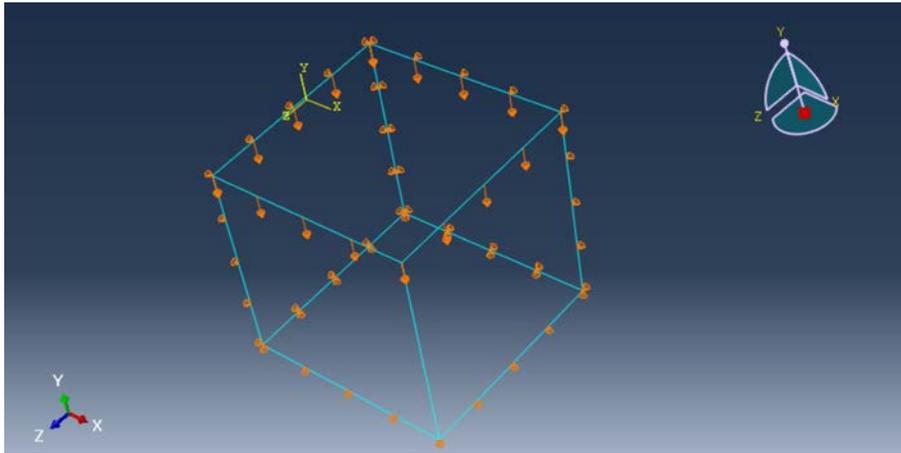
Figure 3.10 Axial loading tests in Abaqus

Two simulations using Abaqus and Python with different sand properties under different confining pressures were carried out. The properties of the sand are listed in Table 3.5. C_{G1} and n_g are the parameters in Equation (3.1). C_1, C_2, C_3, and C_4 are the parameters in Equation (3.6) and (3.7). As seen in Figure 3.11 and 3.12, the two solutions have small difference. It is caused by the geostatic step in Abaqus applying confining pressure on the element. After the geostatic step, the initial strain of the element is around 0.001% before loading, which results in a mild decrease of the initial stiffness according to the theory of $G/G_{max} - \log\gamma$ curve. So, the solution of Abaqus is slightly lower than the solution of Python. However, it still can be concluded that the subroutine of the soil constitutive model works correctly in monotonic loading.

Table 3.5 Parameters of sand used in element tests

Test #	Test 1	Test 2
C_{G1} (psi)	15068	12375
n_g	0.45	0.32
$C_1(\%)$	0.106	0.043
C_2	0.311	0.406
C_3	0.854	0.943
C_4	0.311	0.1

Test #	Test 1	Test 2
α_a	0.1	1.0
α_b	0	1.0
α_c	0.1	1.0
Poisson's ratio	0.3	0.3
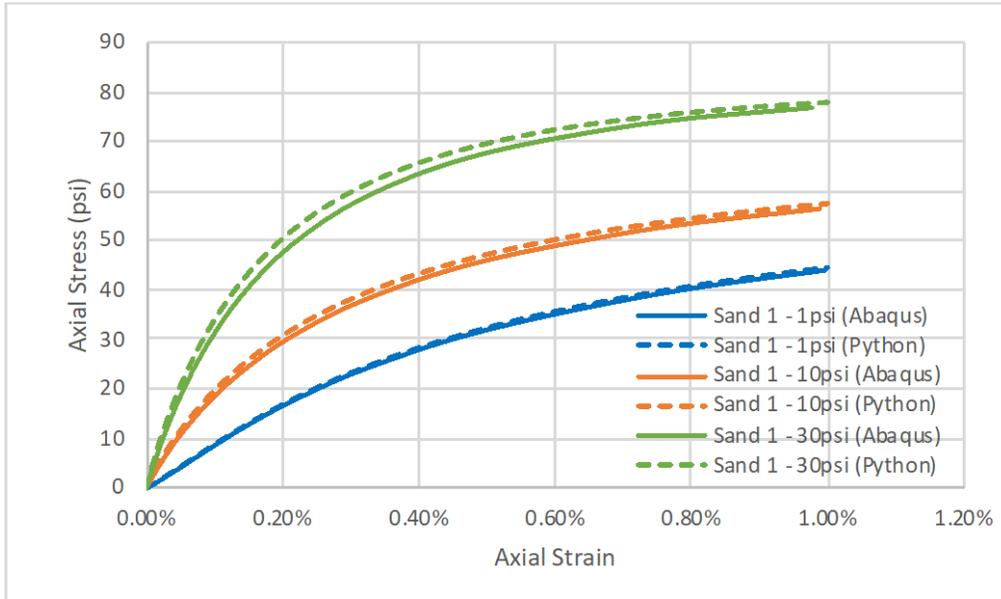
Figure 3.11 Verification of Subroutine of Abaqus (Test 1)
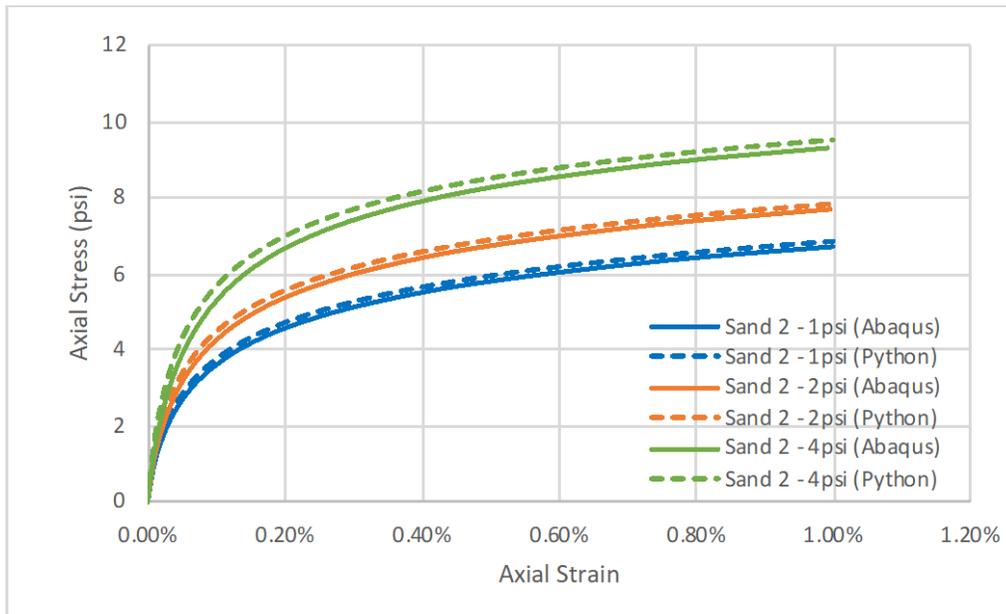
Figure 3.12 Verification of Subroutine of Abaqus (Test 2)

3.3.5 Comparison between Predictions and Measurements

The comparison includes the dynamic triaxial tests and the torsional shear tests on several kinds of sand. The actual triaxial test data was obtained from dynamic tests which were carried out at Tokyo University under the JSSMFE Standard. The data of the torsional shear tests was obtained from the database of the soil dynamic laboratory at The University of Texas at Austin.

3.3.5.1 Dynamic Triaxial Tests

Tatsuoka et al. (1995) presented Young's modulus, E, measured by dynamic triaxial test (cyclic triaxial test) on Toyoura sand and Ticino sand where the axial strain was smaller than 0.1%. In dynamic triaxial tests, Young's modulus, E, was measured at different levels of axial strain. The deviatoric stress was calculated by multiplication of Young's modulus and axial strain. We compared the results of the stress-strain curve obtained from the dynamic triaxial test and the numerical element tests. The results show good agreement.

Table 3.6 shows the physical properties of the sands and the confining pressure in the dynamic triaxial tests.

Table 3.6 Physical properties of Toyoura and Ticino Sand (Tatsuoka et al., 1995)

Sand	G_s	$D_{50}(mm)$	D_{60}/D_{10}	e	$\sigma_c\,(kPa)$	v
Toyoura	2.65	0.18	1.30	0.70	78.5	0.3
Ticino	2.65	0.55	1.57	0.64	49.0	0.3

Figures 3.13 and 3.14 show the stress-strain curves measured in dynamic triaxial tests and predicted by the numerical element tests. The prediction was calculated by Menq (2003) based on the properties of the sand and the specified confining pressure. The measurement results were obtained from dynamic tests using local deformation transducers (LDT) and proximeters. For Toyoura sand, the predictions are in good agreement with the measurement from LDT and slightly higher than the measurement from the proximeter. For Ticino sand, the predictions had a good fit with the measurement from LDT at low strains but were higher than the measurements when the strain was increased.
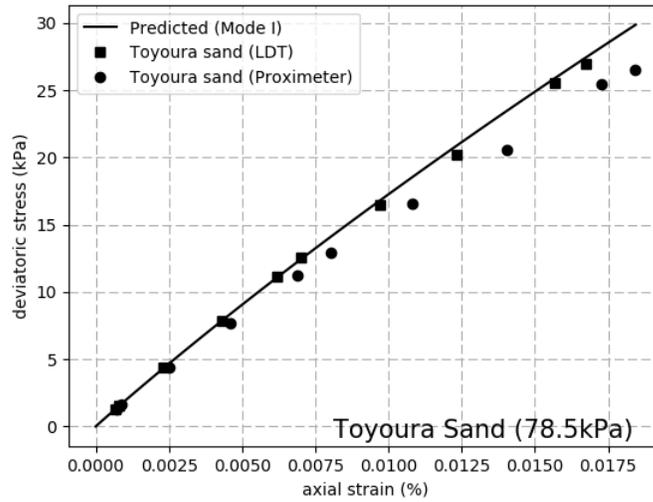
Figure 3.13 Preliminary comparison between the prediction and measurement (Toyoura Sand)
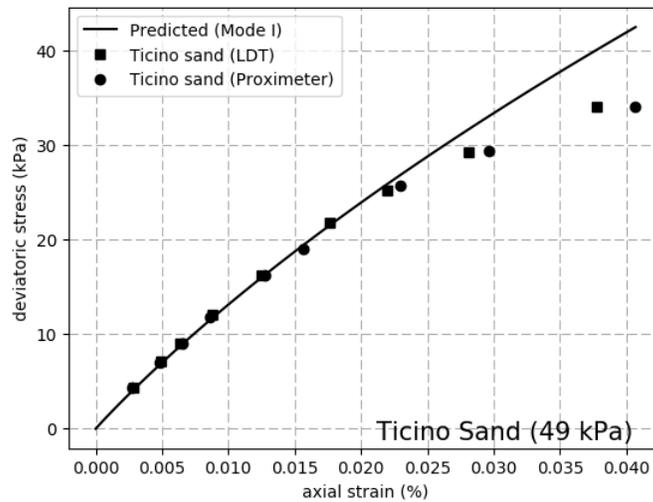
Figure 3.14 Preliminary comparison between the prediction and measurement (Ticino Sand)

Though the predictions based on Menq (2003) empirical equation and measurement from laboratory tests have good agreement, the value of G_{max} and the degradation curve of G/G_{max} must be modified by dynamic laboratory tests of torsional shear and resonant column.

Based on the dynamic laboratory tests, Tatsuoka, Kohata and Presti (1995) developed a relationship between the mean effective stress and the normalized small-strain shear modulus for Toyoura Sand while Presti (1993) gave the relationship for Ticino Sand.

For Toyoura Sand, the dependence of the small-strain shear modulus on void ratio and mean effective stress was defined in the following manner:

$$G_{\max} = 900 \times (2.27 - e)^2 / (1+e) \times \sigma_0^{0.4} \times P_a^{0.6} \qquad (3.59)$$

The unit of Equation (3.59) is bar. The void ratio (e) equaled 0.7, so Equation (44) can be re-written as:

$$G_{\max} = 114397 \times (\sigma_0 / P_a)^{0.4} \qquad (3.60)$$

The unit of Equation (3.60) is kPa.

For Ticino Sand, the dependence of the maximum shear modulus on void ratio and mean effective stress was defined in the following manner:

$$G_{\max} = 710 \times (2.27 - e)^2 / (1+e) \times \sigma_0^{0.43} \times P_a^{0.57} \qquad (3.61)$$

The unit of Equation (3.61) is bar. The void ratio (e) is equal to 0.7, Equation (46) can be re-written as:

$$G_{\max} = 101297 \times (\sigma_0 / P_a)^{0.43} \qquad (3.62)$$

The unit of Equation (3.62) is kPa.

Tatsuoka, Kohata and Presti (1995) and Iwasaki, Tatsuoka and Takagi (1978) gave the degradation curves of G measured in torsional shear and resonant column tests for Toyoura Sand and Ticino Sand. The degradation curve measured by the torsional shear tests was higher than the measurement by the resonant column test. The modifications of the degradation curves of G/G_{max} based on the two tests are shown in Figure 3.15 – 3.16.
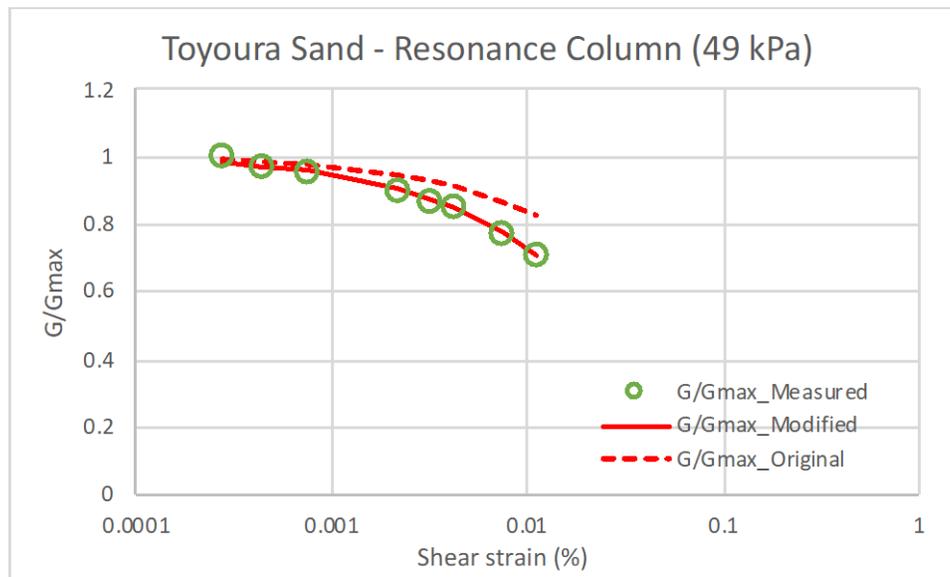
Figure 3.15 Modification of G/G_{max} based on resonance column test for Toyoura Sand

46
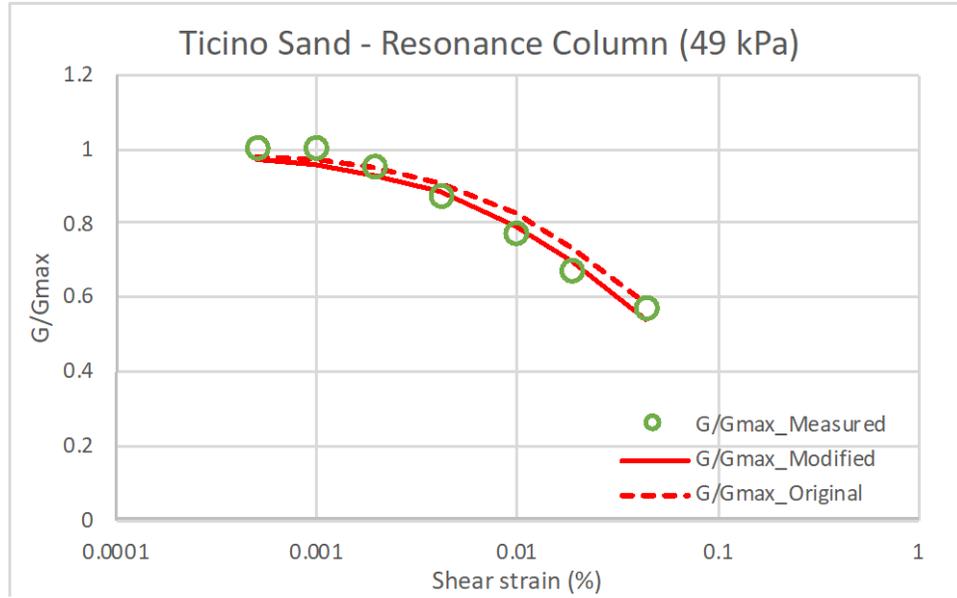
Figure 3.16 Modification of G/G_{max} based on resonance column test for Ticino Sand

For the resonant column tests for Toyoura Sand and Ticino Sand under confining pressure of 49 kPa, the parameters used in Equation (3.3) were modified to:

Table 3.7 Parameters of Sand used in Element Tests

Sand	Toyoura	Ticino
C_{G1} (kPa)	114397	101297
n_g	0.40	0.43
$C_1(\%)$	0.043	0.065
C_2	0.353	0.280
C_3	0.854	0.823
C_4	0.099	0.100
α_a	0.001	0.001
α_b	0.0	0.0
α_c	0.001	0.001
$Poisson's\ ratio$	0.3	0.3

Figure 3.17 and 3.18 show the modified prediction curves compared to the measurement from the dynamic laboratory tests. For both sands, the predictions based on resonance column tests slightly overestimate the stiffness of the sand during axial loading. This is due to the octahedral shear strain, which is smaller than the actual shear strain along the main loading direction. So, the decay of the G/G_{max} is slower than in reality, which results in the overestimation of the shear stiffness during monotonic loading.
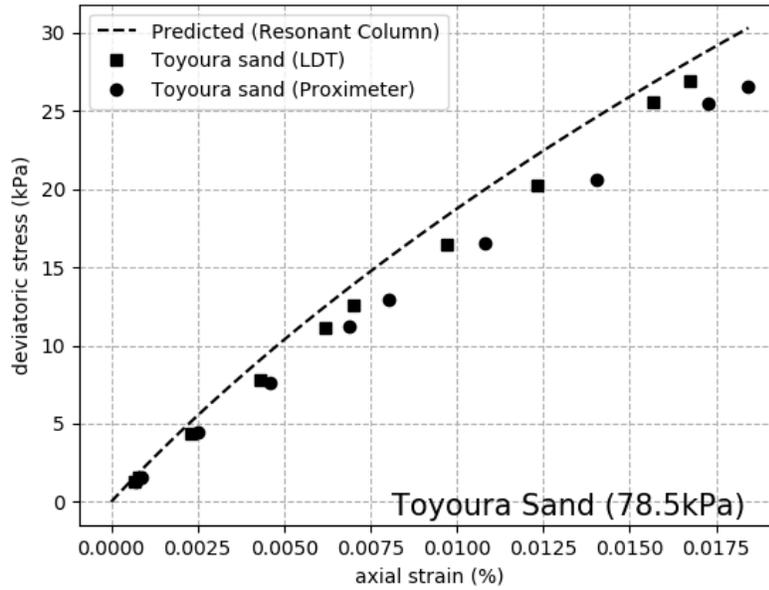
Figure 3.17 Complete comparison between the prediction and measurement (Toyoura Sand)
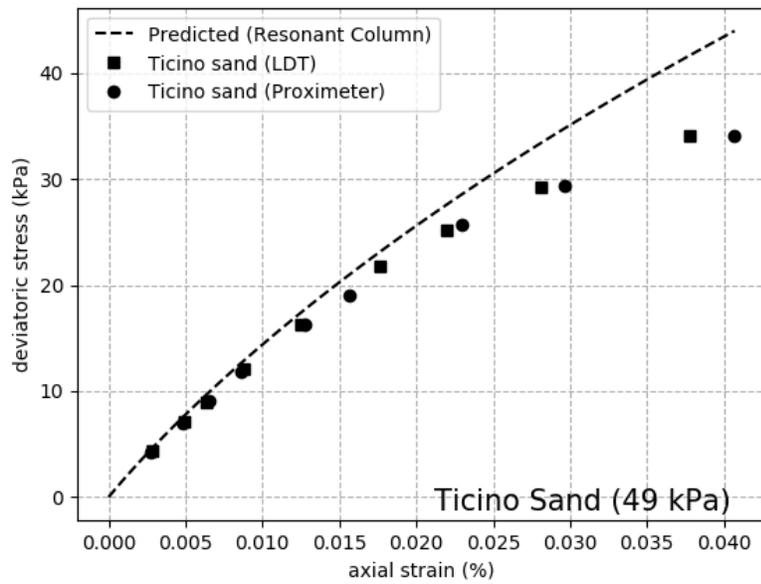
Figure 3.18 Complete comparison between the prediction and measurement (Ticino Sand)

3.3.5.2 Pure Shear Test

This section compares the shear stress versus shear strain from torsional shear tests to numerical predictions for All-Purpose Sand (Appendix D). In torsional shear tests, the shear modulus was measured at different levels of shear strain. The shear stress was obtained by multiplication of the shear strain by the shear modulus.

The All-Purpose Sand was purchased at Home Depot. The properties of All-Purpose Sand in torsional shear test are summarized in Table 3.8.

Table 3.8 Properties of All-Purpose Sand in torsional shear tests

C_u	G_s	$Void\ Ratio$	$D_{50}\ (mm)$
4.6	2.65	0.56	0.67

Figure 3.19 shows the modification of the relationship between the confining pressure and G_{max} based on laboratory tests.
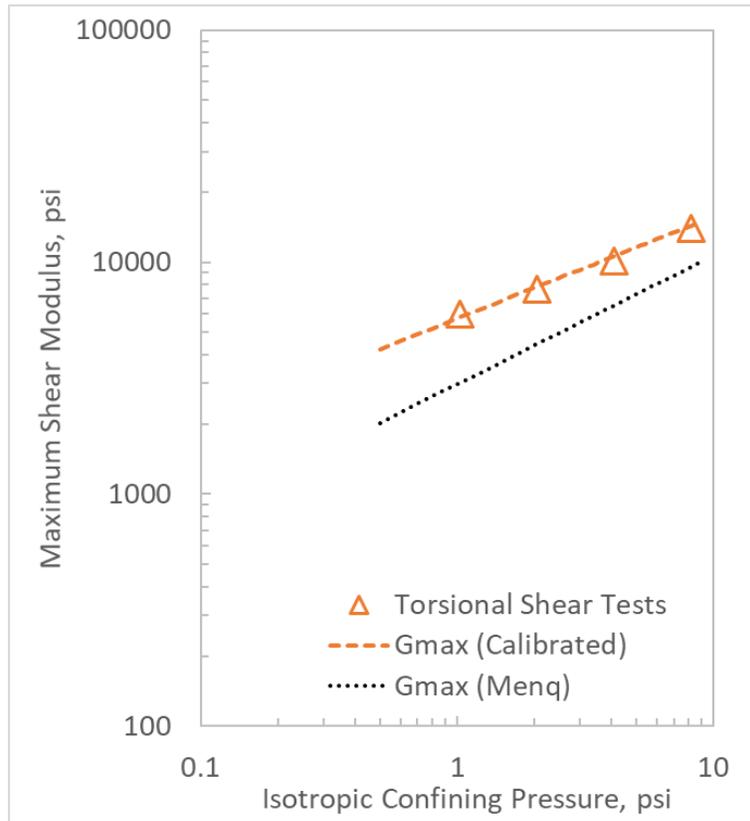
Figure 3.19 Modification of the relationship between confining pressure and G_{max}

Figure 3.20 shows the modification of the relationship between the shear strain and G/G_{max} based on laboratory tests.
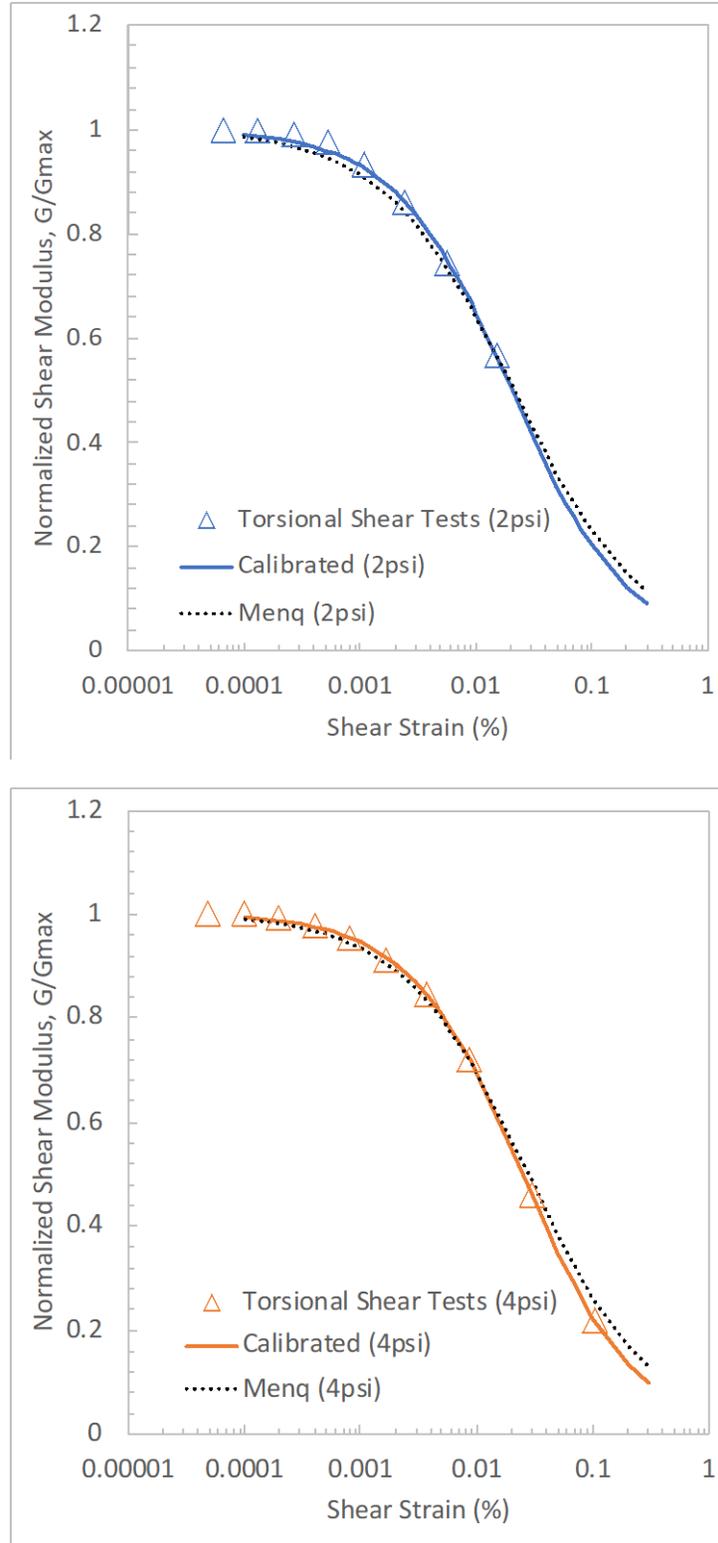
Figure 3.20 Modification of the relationship between shear strain and G/G_{max}

Table 3.9 shows the input parameters for the soil constitutive model calibrated by the laboratory tests.

Table 3.9 Soil parameters for pure shear element test

C_{G1} (psi)	n_G	C_1 (%)	C_2	C_3	C_4
18652	0.44	0.036	0.296	0.95	0.1

Figure 3.21 and 3.22 show the comparison between the measurement and the prediction under confining pressure of 2 psi and 4 psi for the All-Purpose Sand. We can see that the prediction before calibration underestimated the stiffness of the sand during loading, which occurred because Menq (2003) underestimated the value of G_{max} as shown in Figure 3.19. After modifying the value of G_{max} based on laboratory tests, predictions after calibration agreed well with the stiffness of the sand.
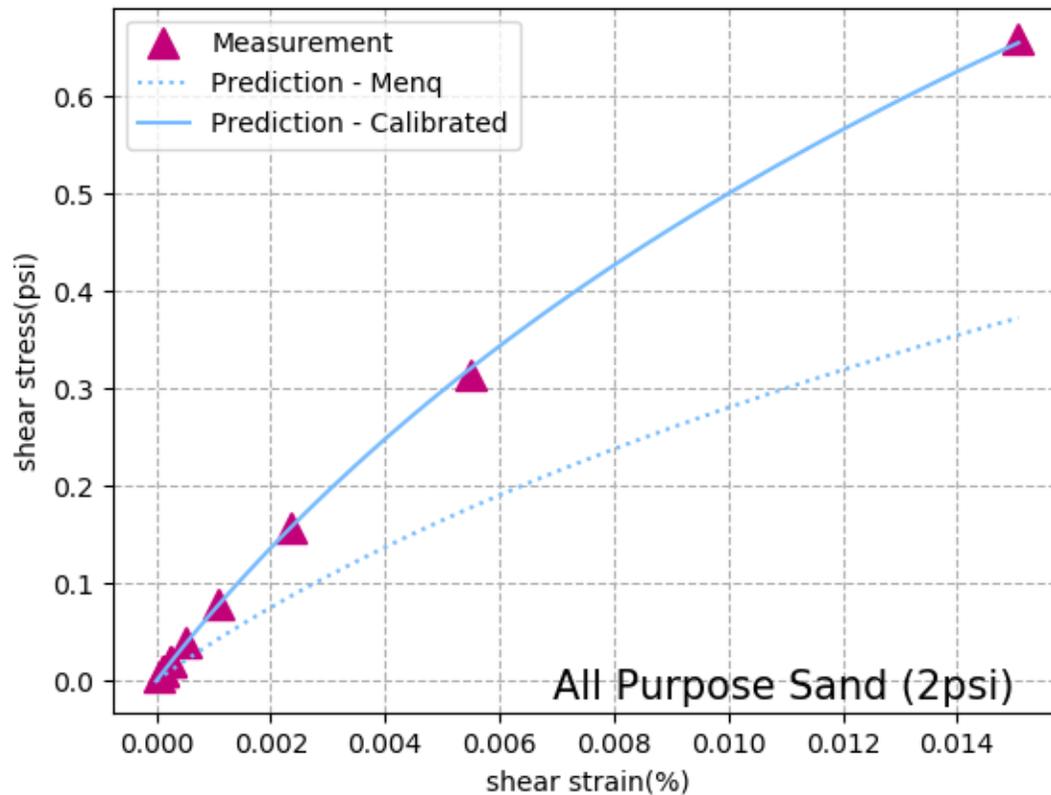
Figure 3.21 Comparison of the prediction and measurement for shear stress versus shear strain (2psi)
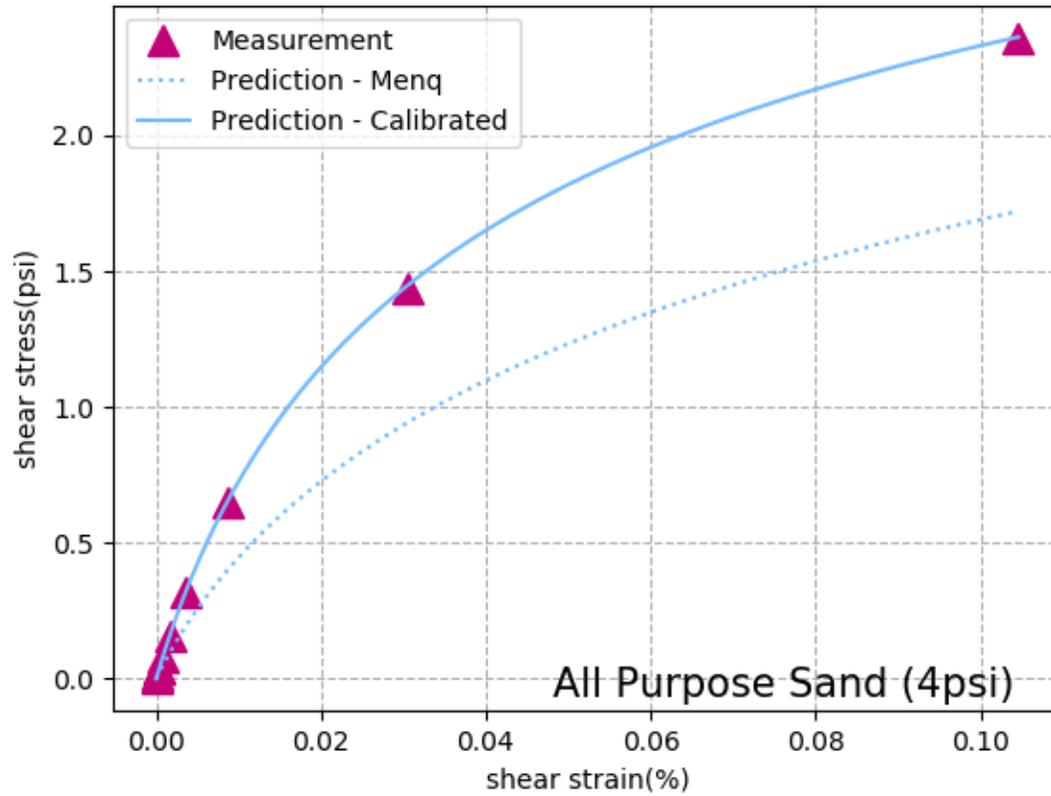
Figure 3.22 Comparison of the prediction and measurement for shear stress and shear strain (4psi)

To investigate the hysteretic behavior simulated by the soil constitutive model using Masing's Rule, we compared the hysteretic loop measured in the torsional shear tests with the predicted hysteretic loop. Figures 3.23 – 3.26 show different hysteretic loops measured at different levels of strain under a confining pressure of 4 psi. From Figures 3.22 – 3.25, the predicted loops have a good fit with the measured loops when the maximum shear strain is lower than 0.02%.
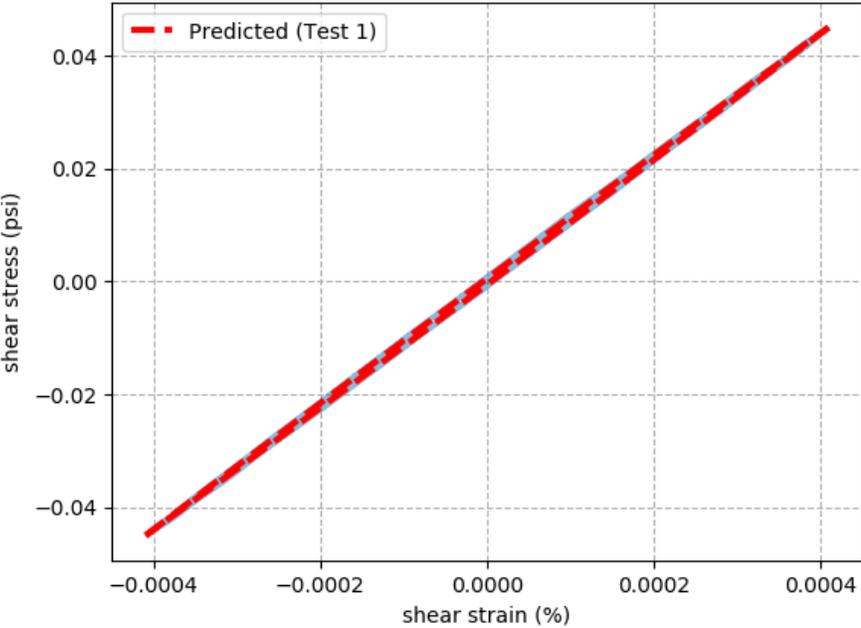
Figure 3.23 Hysteretic behavior (Test 1)
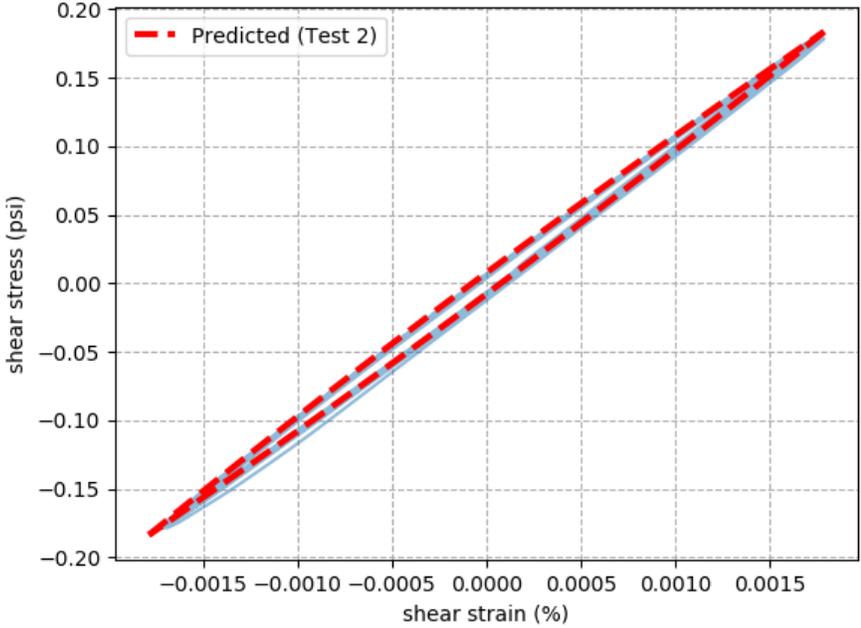
Figure 3.24 Hysteretic behavior (Test 2)
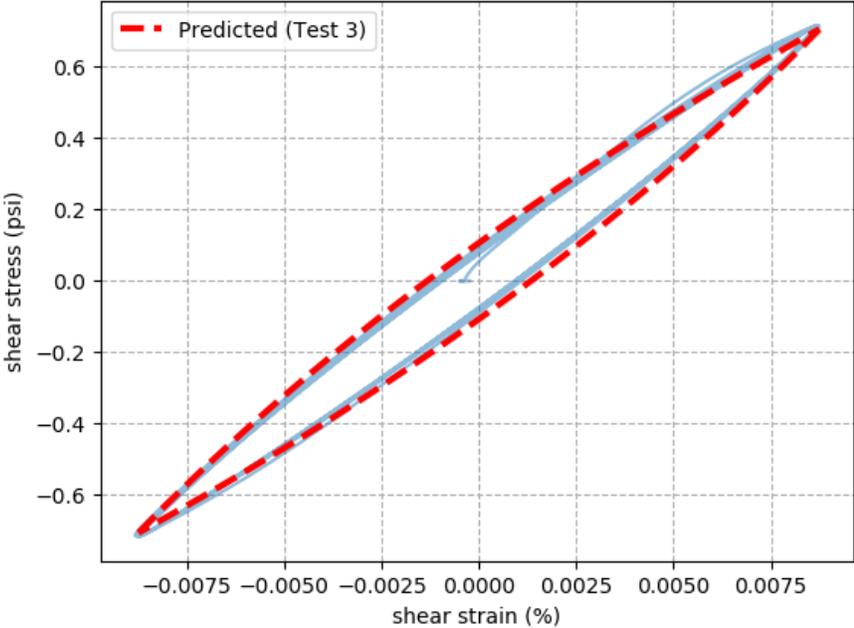
Figure 3.25 Hysteretic behavior (Test 3)
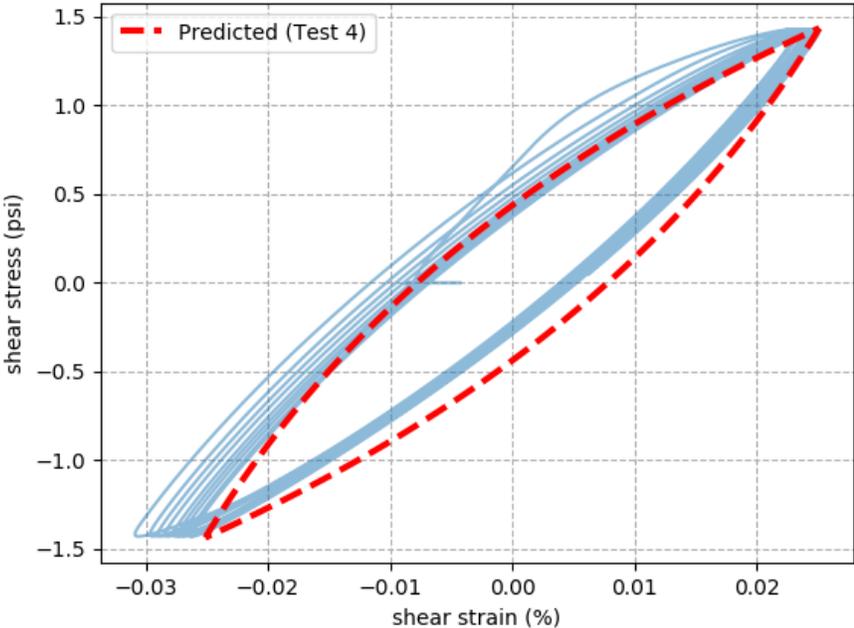
Figure 3.26 Hysteretic behavior (Test 4)

3.3.6 Brief Summary of the Element Test

The following major conclusions can be drawn from the element tests.

1. The soil constitutive model is in good agreement with the actual data from laboratory tests including dynamic triaxial tests.
2. To be more credible, the value of G_{max} and the degradation curve of G/G_{max} must be modified based on resonance column tests.
3. Based on the modified G_{max} and G/G_{max} curve, the soil constitutive model may overpredict the stiffness of the sand. This is due to the use of octahedral shear strain instead of the true shear strain.
4. At relatively low strain levels, the prediction of hysteretic behavior of the soil constitutive model has a good match with the actual data from torsional shear tests.

3.4 Abaqus Analysis of Mustang Island Tests

This section presents the summary of the original Mustang Island test conducted in the 1970s and the dynamic field test conducted by UT Austin in 2017. A 3-D finite element model is established based on the information from original information and the input from the dynamic field test. The result of the finite element model is compared to the field measured lateral load versus displacement curve and shows good agreement.

3.4.1 Introduction

In the 1970s, a series of lateral load tests on two 0.6 m (24-in.) long piles in sand conducted by Reese, Cox, and Grubbs (1974) to develop criteria for the design of laterally loaded piles in sand under static and cyclic loads. The site was selected in the northern part of Mustang Island State Park, on privately held land, see Figure 3.27. Two soil borings were made at the test site. A comprehensive series of field tests was performed to collect data during lateral loading of two test piles installed at the site where soils consisted of clean fine silty fine sand. Laboratory tests were performed on samples that were obtained by piston sampler in a nearby boring. The p-y curves derived from these field tests became the criteria for the design of laterally loaded piles, which is still being used today.

To supplement these field tests, additional field tests were conducted in August 2017 and laboratory tests were being conducted on soil samples from the site. Field seismic testing using the SASW method was performed at three locations near the original test site. Professor Kenneth Stokoe led the field seismic team. In addition, combined resonant column and torsional shear (RCTS) tests were being conducted in the soil dynamic laboratory in The University of Texas at Austin to measure the small-strain and non-linear shear modulus of sand.

Figure 3.27 Location of the field testing of laterally loaded piles at Mustang Island (Google Maps)

3.4.2 Review of Soil Properties

The soil profile reported by Reese, Cox, and Grubbs (1974) is shown in Figure 3.28. Based on the boring tests at the site, soil in the top 42 ft was classified as fine sand. According to standard and wire-line penetration tests, the sand from 0 to 20 ft was classified as medium dense, 20 to 40 ft as dense, and 50 to 70 ft as dense. In the lateral loading tests, the water table was maintained above the ground surface during loading to simulate conditions which was similar to an offshore condition. Figure 3.29 shows three grain-size distribution curves of samples recovered from depths of 3, 10, and 15.5 ft. The curves show that the cohesionless materials were poorly graded sands with percentage of fines passing the number 200 sieve varying from 0 to 10 percent. The sand particles were found to be subangular with a large percentage of flaky grains. In the computations of p-y curves, Reese, Cox, and Koop (1974) used the friction angle (φ) of 39° and a submerged unit weight of about 66 pcf.
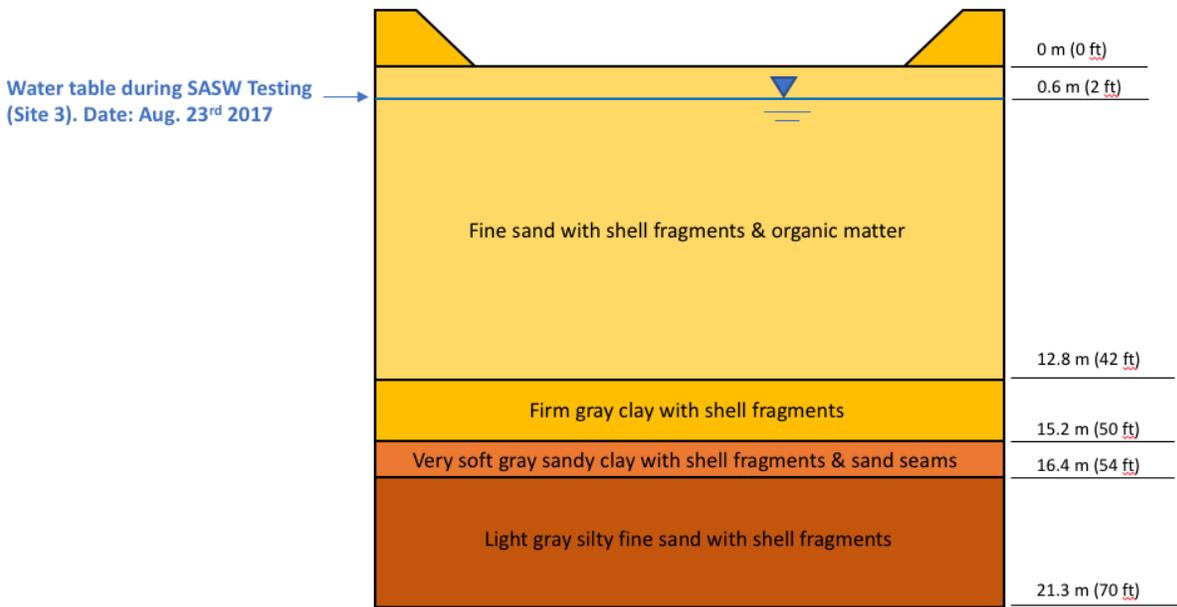
Figure 3.28 Soil types and layer depth at the locations of field testing (Reese, Cox, and Grubbs 1974)
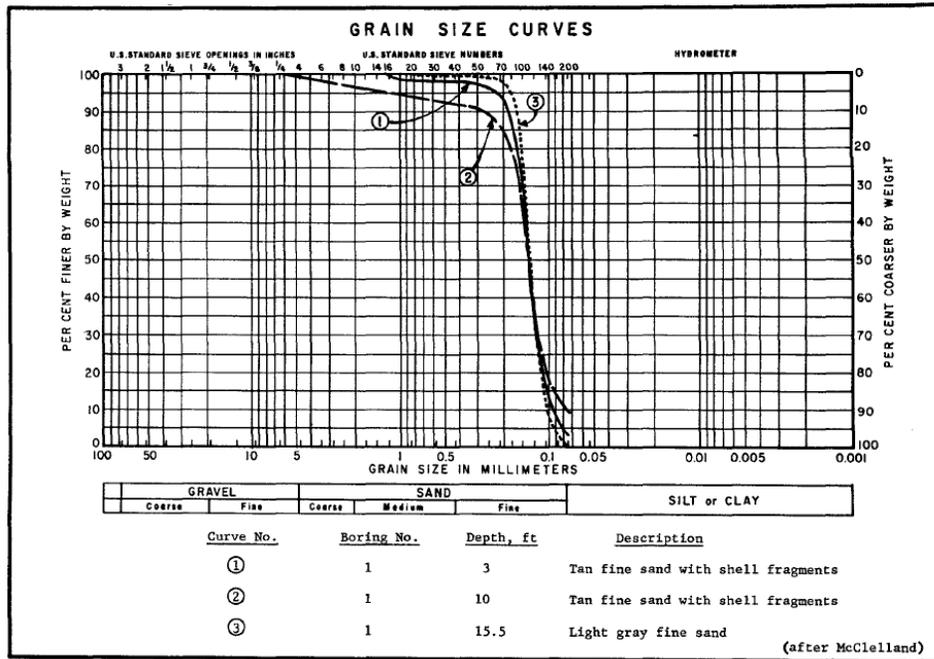
Figure 3.29 Grain-size distribution curves from the boring: sample depths equal 3, 10, and 15.5 ft (Reese, Cox, and Grubbs 1974)

Table 3.10 Sand properties read from grain-size distribution curves

	Depth = 3 ft	Depth = 10 ft	Depth = 15.5 ft
D60 (mm)	0.15	0.15	0.15
D50 (mm)	0.14	0.14	0.14
D30 (mm)	0.13	0.13	0.13
D10 (mm)	0.1	0.08	0.11
Cu	1.50	1.88	1.36

3.4.3 Review of Pile Properties

The test piles were 24-inch diameter with a wall thickness of 0.375 inch. The material of the steel of the pile was A-53 grade-B seamless steel. The density of the steel was assumed to be 503 pcf and the Young's modulus of the steel was assumed to be 29,000,000 psi. The embedment depth was 69 ft. The connecting flange, where the load to the free-head pile was applied at, was located 1 ft above the mudline.

3.4.4 Dynamic Field Test and Dynamic Laboratory Measurement Conducted in 2017

The soil dynamic tests include the field dynamic test and the laboratory dynamic test. The field dynamic test determines the basic trend and magnitude of the shear wave velocity profile. The laboratory dynamic test gives the relationship between the shear wave velocity versus confining pressure and the degradation curves of normalized shear modulus versus shear strain.

3.4.4.1 Dynamic Field Test

To obtain the in-situ relationship between the shear velocity and the depth (stress state) of the soil at the test site, Professor Kenneth Stokoe and his soil dynamic team performed spectral-analysis-of-surface-wave (SASW) tests along two lines near test site and one line at the test site. The results from SASW, cross-hole tests, and RCTS tests were combined to best estimate the shear wave velocity profile. The SASW tests conducted along Line #1 and Line #2 were used to evaluate the shear wave velocity at deeper depths by using long waves. The seismic waves were Rayleigh-type surface waves generated by the shaker truck named "Thumper" (Figure 3.31). The SASW tests conducted along Line #3 were at the original test site and this testing was focused on the shear wave velocity of shallower depths near the ground. The wave was generated by a sledgehammer impacting a steel plate on the ground surface. Figure 3.33 shows the best-fit V_s profile from SASW tests and the resonant column tests.

Figure 3.30 Location of the three SASW test arrays at the Mustang Island Site

Figure 3.31 Shaker truck "Thumper" used in in-situ dynamic tests (Site 1 and Site 2)

Figure 3.32 Generating waves using sledgehammer at Site 3
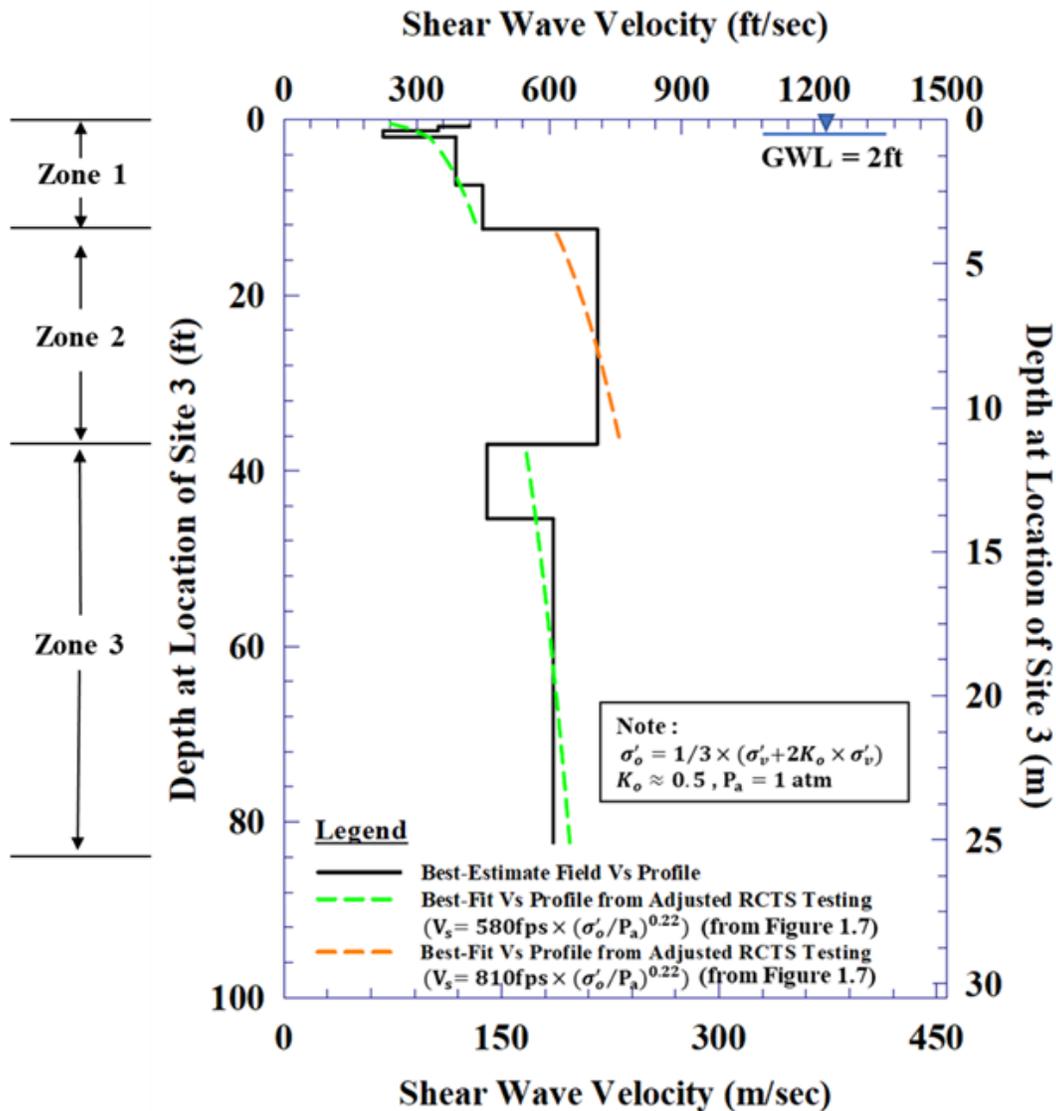
Figure 3.33 Comparison of the best-estimate field Vs profile from SASW testing and two adjusted best-fit curves using a Vs profiles determined by laboratory RCTS testing

Figure 3.33 shows the best-estimate field shear velocity profile from SASW testing and two adjusted best-fit curves using a shear velocity profiles determined by laboratory dynamic testing (resonant column test). The best-estimate shear wave velocity profile was determined by the SASW tests along Line #1, Line #2, and Line #3. The shear wave velocity profile at Zone 1 was determined by SASW tests along Line #3 using short waves. The shear wave velocity profiles at Zone 2 and Zone 3 were determined by SASW tests along Line #1 and Line #2. The parabolic dashed lines were the shear wave velocity profiles predicted by the dynamic properties of the sand and the effective confining pressure with the increase of depth. The green dashed lines better represent the shear wave velocity profiles in Zone 1 and Zone 3. The orange dashed line better represents the shear wave velocity profile in Zone 2. More detail about the best-estimate shear velocity profile is addressed in Appendix A.

3.4.4.2 Dynamic Laboratory Test

Low-amplitude resonant column (RC-LA) tests and high-amplitude resonant column (RC-HA) tests were performed to evaluate the dynamic properties of the sand collected at the Test Site. The detailed results of the tests are attached in Appendix B.

Six levels of the confining pressures were selected for the sand specimens; 1.5, 3, 6, 12, 24, and 48 psi. There are two parts of the resonant column procedure: (1) the initial loading RC tests and (2) the unloading RC tests. In the initial loading RC-LA, the confining pressures were increased in steps following the six confining pressure levels. At each confining pressure, RC-LA tests were performed for about 65 minutes to obtain the variation of dynamic properties with time. After RC-LA testing was completed at the highest confining pressure of 48 psi, the confining pressure applied to the specimen was unloaded in steps from 48 psi to 1.5 psi. RC-LA tests were again performed at each unloading of the specimen for about 35 minutes. RC-HA tests were performed to investigate the nonlinear behavior of the specimen. The RC-HA tests were conducted after the RC-LA tests at 100 minutes. RC-HA tests were performed at 3 confining pressure levels: 3, 12, and 48 psi. At the three confining pressures, the RC-HA tests were conducted at reloading and unloading.

3.4.4.3 Modification of G_{max} and $G/G_{max} - \log \gamma$ relationships in Abaqus (Mustang Island Sand)

To better simulate the specific behavior of Mustang Island Sand, the empirical equations provided by Menq (2003) need to be modified based the results of the RCTS tests. The R-squared method was used in the regression analysis to get the best-fit curve between the measured and numerical G_{max} and G/G_{max} - $\log \gamma$ relationships.

For G_{max}:

$$G_{\max} = 15068 \times \left(\frac{\sigma'_0}{14.7} \right)^{0.452} \quad \text{(psi)}$$
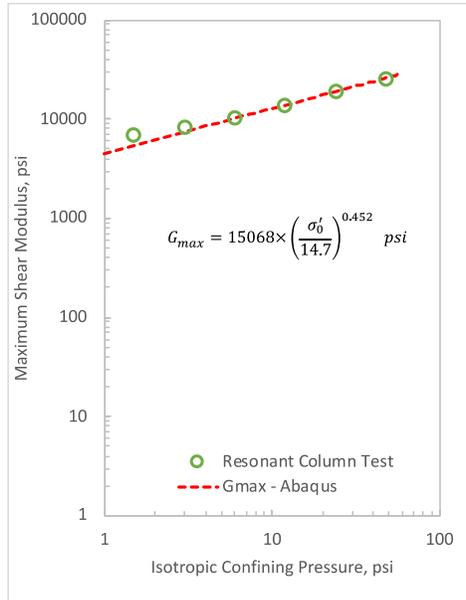
Figure 3.34 Calibrated relationship between G_{max} and isotropic confining pressure (Mustang Island Sand)

For G/G_{max} - $\log \gamma$:

$$\gamma_r = 0.106 \times \left(\frac{\sigma_0'}{14.7} \right)^{0.311}$$

$$a = 0.854 + 0.0896 \times \log(\frac{\sigma_0'}{14.7})$$
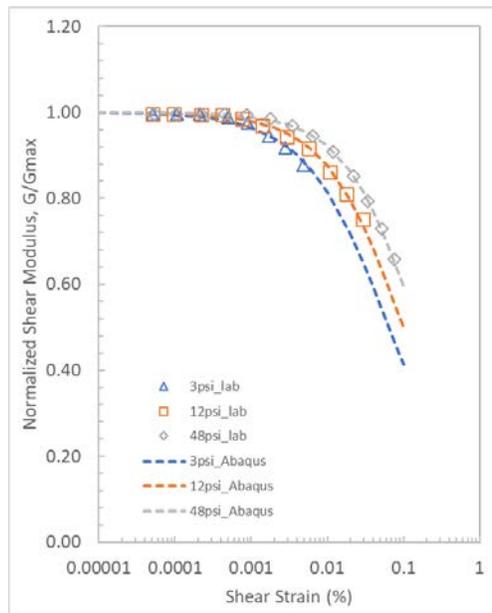
Figure 3.35 Calibrated relationship of $G/G_{max} - \log \gamma$ (Mustang Island Sand)

63

Table 3.11 summarizes the input parameter for Mustang Island Sand in Abaqus.

Table 3.11 Input parameters for Abaqus of Mustang Island Sand

C_{G1} (psi)	n_G	C_1 (%)	C_2	C_3	C_4	α_a	α_b	α_c	υ
15068	0.452	0.106	0.311	0.854	0.0896	0.001	0.000	0.001	0.33

3.4.5 Analysis of the Relationship between Lateral Load and Lateral Displacement

In this section, lateral load versus lateral displacement curves predicted by the soil constitutive model in Abaqus are compared with the lateral tests conducted in the field of Mustang Island. The preliminary interested displacement is determined through analyzing the operating wind turbine in Belwind.

3.4.5.1 3-D Finite Element Modeling with Operating Wind Turbine in Belwind

A 3-D finite element model was created in Abaqus to study the interested displacement of the monopile at mudline. The soil profile was assumed based on the sand properties collected from Mustang Island as shown in Table 3.10. According the design reports for Belwind Offshore Wind Farm, the typical dimensions of the monopile were 195-inch diameter, 780-inch embedment depth, and 2.4-inch wall thickness. The Young's modulus of the steel was assumed to be 29,000,000 psi. The overturning moment on the monopile at mudline was 266,000,000 lbs-inch and the horizontal force was 69,700 lbs based on the wind speed 39 ft/sec. The interface between the pile and soil was assumed to be frictionless.
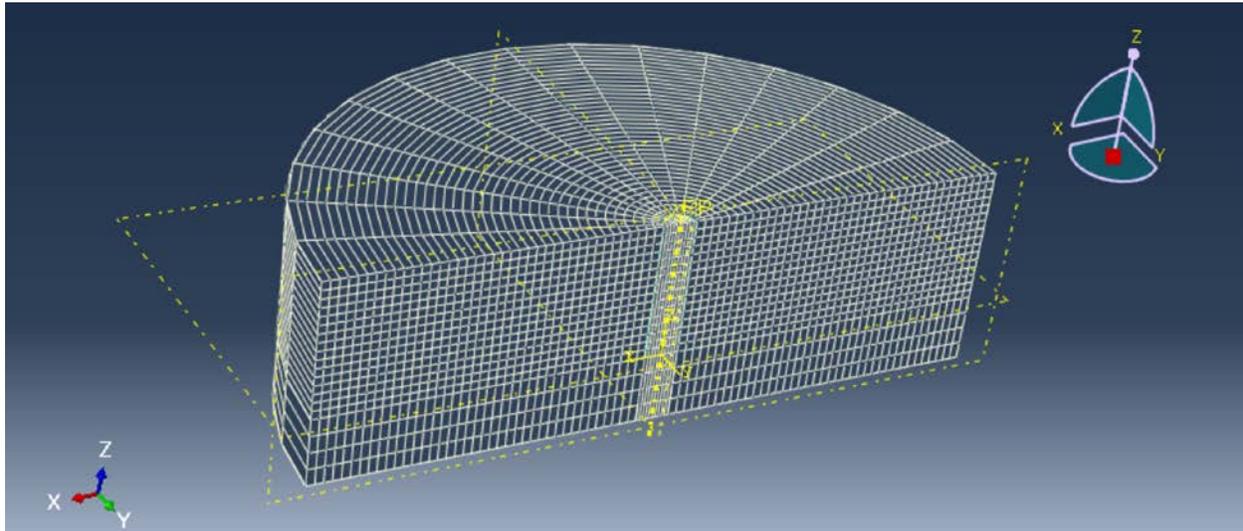
Figure 3.36 Monopile model based on Belwind

The predicted displacement at the mudline was 0.4 inch or 0.2% of the monopile diameter. The largest shear strain in all the soil elements was 0.8%. However, the largest shear strain in the resonance column test was up to 0.1%. To complement the shape of the $G/G_{max} - \log\gamma$ curve larger than 0.1%, three conventional triaxial tests under low confining pressures were done to calibrate the curve.

Before calibrating the $G/G_{max} - \log\gamma$ curve, by using the parameters in Table 3.10, the comparison between the 1-D element axial loading tests and the triaxial tests was shown in Figure 3.37. The numerical modeling overestimated the stiffness of the sand.
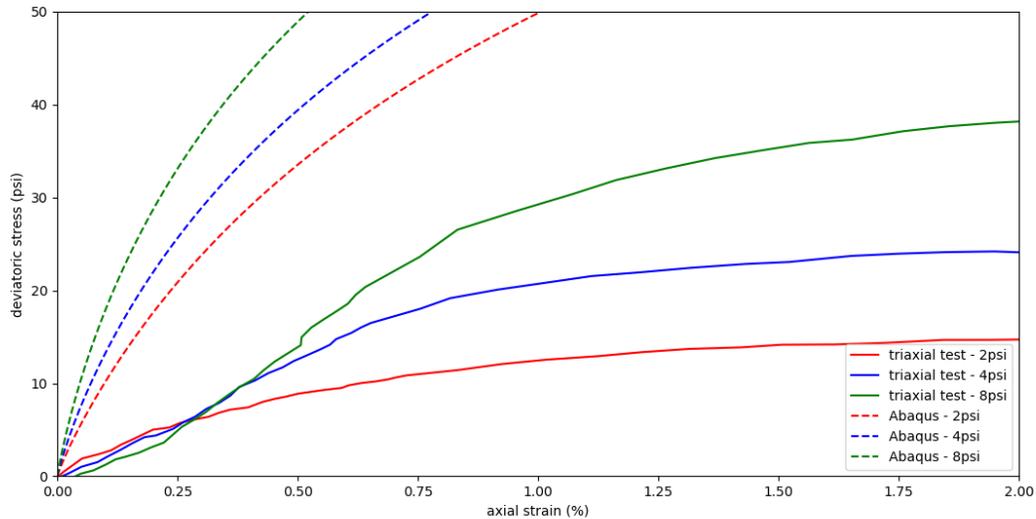
Figure 3.37 Comparison between the 1-D element axial loading tests and triaxial tests (before calibration)

The calibrated properties of Mustang Island Sand are listed in Table 3.12. Figure 3.38 shows the comparison between the numerical modeling and the measurement after calibration. The predicted curves have a good agreement with the measurement when the strain is larger than 1%. Because the conventional triaxial tests have poor capability to capture the stiffness of the soil in the small strain, the predicted curves have poor fit with the measurement in the small strain as expected.

The calibrated $G/G_{max} - \log\gamma$ curves are shown in Figure 3.39. The calibrated curves still have a good fit with the measurement of resonance column tests under shear strain 0.1%, so the calibration had little influence on the stiffness in the small shear strain. This made the $G/G_{max} - \log\gamma$ curve perform better in the large shear strain.

Table 3.12 Input parameters for Abaqus of Mustang Island Sand (after calibration)

C_{G1} (psi)	n_G	C_1 (%)	C_2	C_3	C_4	α_a	α_b	α_c	υ
15068	0.452	0.078	0.400	0.950	0.00	0.001	0.000	0.001	0.33
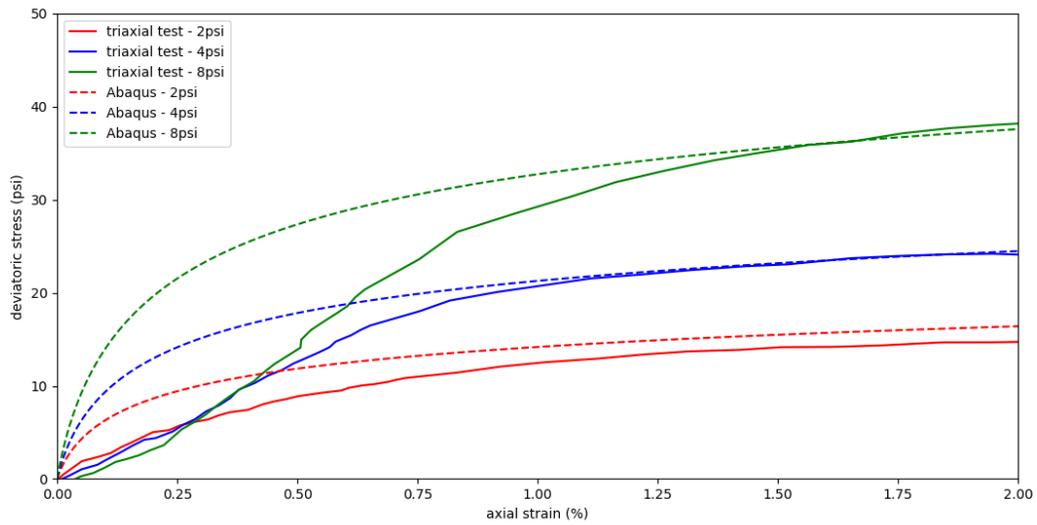
Figure 3.38 Comparison between the 1-D element axial loading tests and triaxial tests (after calibration)
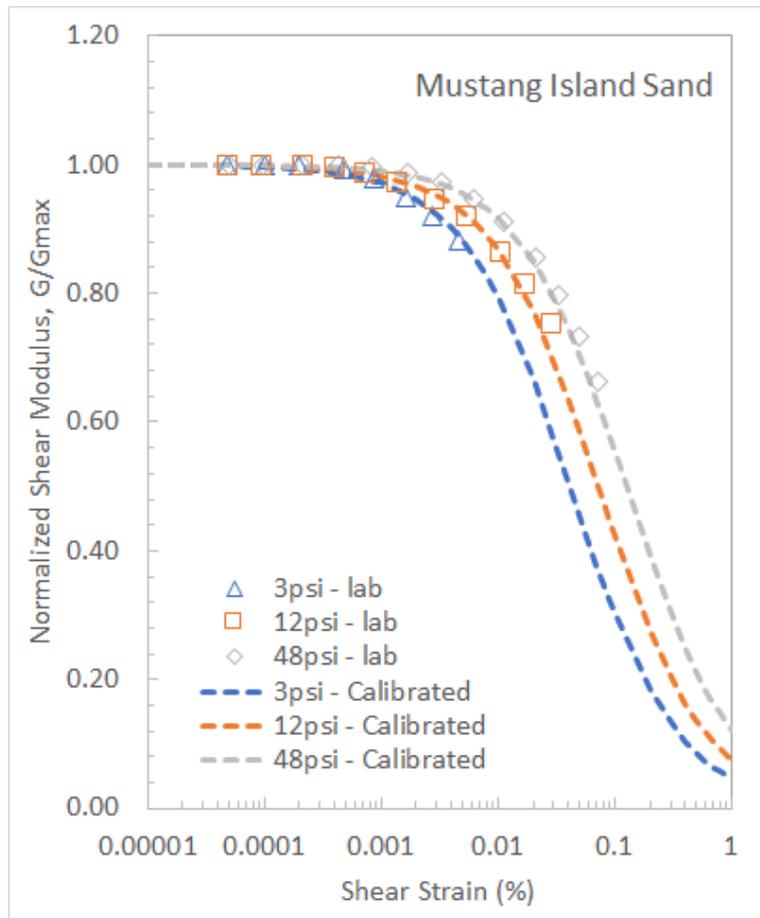
Figure 3.39 Calibrated relationship of $G/G_{max} - \log\gamma$ (Mustang Island Sand, after calibration)

After the soil profile was updated by the calibrated soil properties in Table 3.11, the updated predicted displacement of the monopile at mudline was 0.55 inch, or 0.3% of the monopile diameter.

3.4.5.2 3-D Finite Element Modeling with Mustang Island Test

A finite element analysis in Abaqus was carried out to predict the behavior of the pile under the lateral load.

In the 3-D finite element model, the diameter of the pile was modeled as 24 inches, which is the same as the diameter of the pile in field test. The length of the pile below the soil surface in the modeling was 406 inches, which is less than the real length of the pile used in the field test. The reasons for just using half of the pile length in the modeling are:

1) For small lateral displacement of the slender pile, the soil near the surface contributes most to the response of the lateral displacement on the pile and;
2) For simulating the soil with half length, the thickness of the sand was half compared to it in the modeling with full length of pile, reducing the calculation effort needed for Abaqus.

Horizontally, the soil extended 10 diameters from the edge of the pile with 8-node linear brick elements.
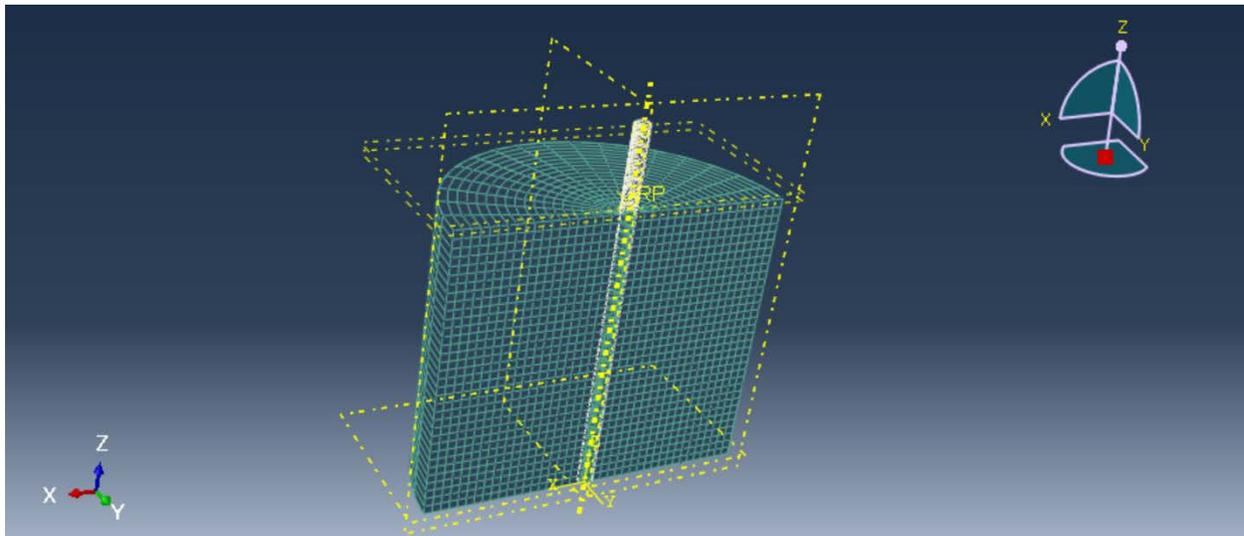
Figure 3.40 Slender pile model in Abaqus for Mustang Island Test

The pile was modeled as hollow pile with a diameter of 24 in, wall thickness of 0.375 in, and an elastic modulus of 29,000,000 psi. The pile was assumed to have a unit weight equal to 0.3 pci and a Poisson's ratio equal to 0.3. The soil-pile interface was assumed to be frictionless. The pile loading was displacement controlled with the displacement applied to the pile in the horizontal direction 1 ft above the ground line. The displacement applied at the loading point was 1% of the diameter of the pile.

According to the dynamic laboratory report attached in Appendix B, the total unit weight of the sand was equal to 119 pcf, the uniformity coefficient C_u was equal to 1.31, the void ratio was 0.67, and the Poisson's ratio was 0.33. The in-situ mean effective stress (σ_0') was estimated with:

$$\sigma_0' = \frac{\sigma_v' + 2\sigma_v' K_0}{3}$$

where, K_0 is determined by $K_0 = v/(1 - v)$ and v is Poisson's ratio. So for this model, K_0 is equal to 0.49.

The shear velocity profile in Figure 3.41 needs to be converted to a shear stiffness profile. First, the shear velocity profile was digitized in the spreadsheet and plotted in Figure 3.40. Zone 1 and Zone 2 were two different kinds of sand. The normalized confining pressure index 0.22 was obtained from RC tests. The shear velocity at 1 atm was assumed as 560 fps in Zone 1 and 818 fps in Zone 2 to best-fit the field measurement.
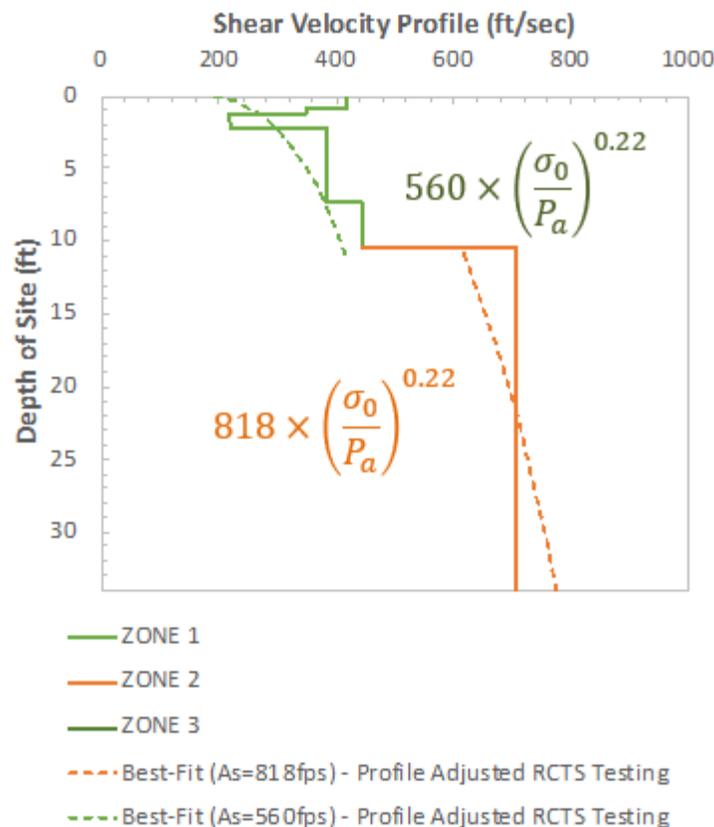
Figure 3.41 Digitized shear wave velocity profile for Mustang Island Test

During the dynamic field testing, the water table was 2 feet below the sand surface. However, Figure 3.42 showed that during the lateral load tests, the water table was maintained at the sand surface. Before the lateral load tests, the site was excavated about 5.5 feet of material to reach the water table. In addition, 2.5 ft of clay was removed and sand was filled in to bring the soil surface back up to the water table (Reese, Cox, and Grubbs, 1974). So, the soil surface during the dynamic field testing was higher than the surface during lateral load tests. It was suspected that 2 feet of sand was backfilled after the complete of the

lateral load tests. Therefore, the 2 feet of sand needed to be removed from the shear velocity profile. Figure 3.43 showed the modification on the shear velocity profile by removing the 2 feet of the sand at top.
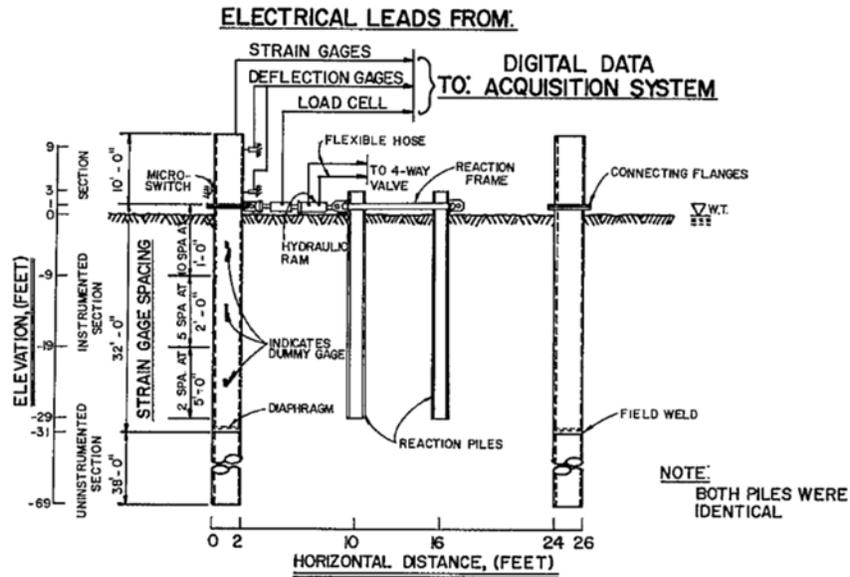
Figure 3.42 Test setup of lateral load tests (Reese, Cox, and Grubbs 1974)
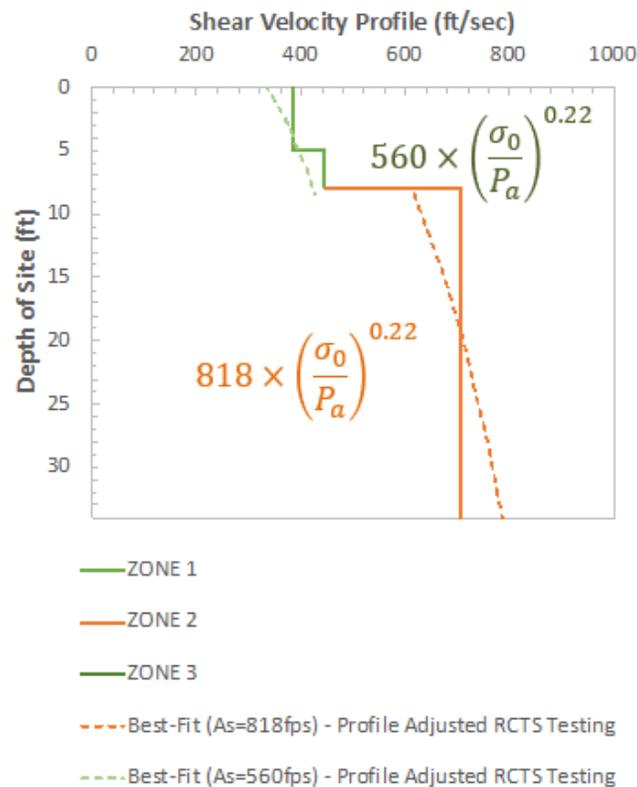
Figure 3.43 Digitized shear wave velocity profile for Mustang Island Test (modification-a)

Because the water table was at the soil surface and the sand was cohesionless, the shear velocity at the surface should be very small. The shear velocity profile in Zone 1 was updated to make the shear velocity at the surface close to zero (Figure 3.44).
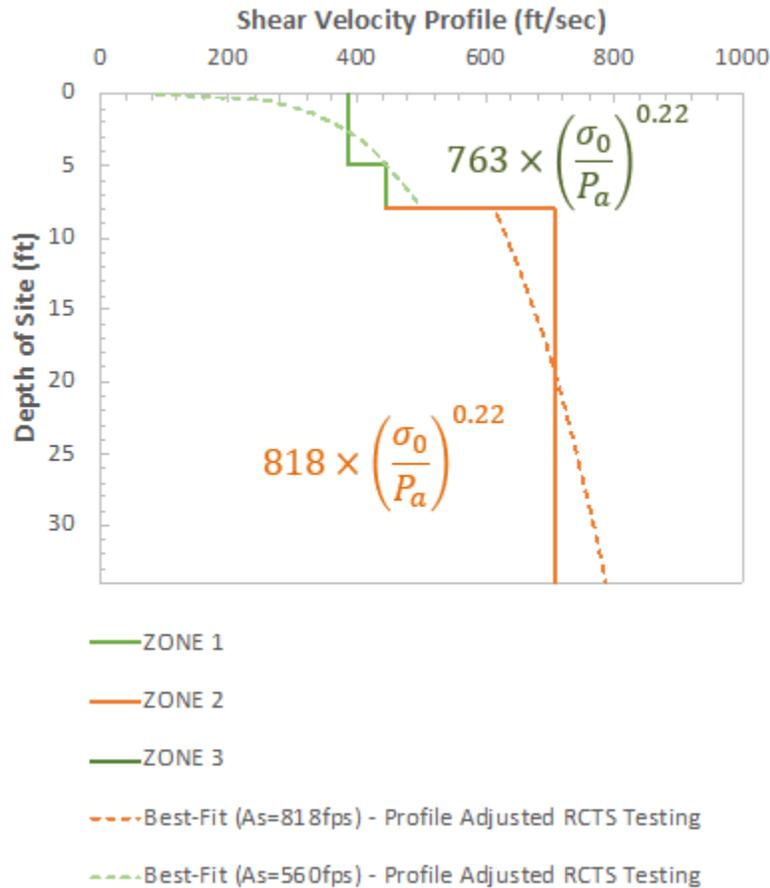
Figure 3.44 Digitized shear wave velocity profile for Mustang Island Test (modification-b)

The relationship between the maximum shear stiffness G_{max}, shear velocity V_s, and density ρ_s is $G_{max} = \rho V_s^2$. The total unit weight of the sand was assumed to be 0.694 pci. The shear velocity profile in Figure 3.44 was converted to the maximum shear stiffness profile in Figure 3.45. Table 3.12 summarizes the input parameters for the sand in Abaqus based on the shear stiffness profile and the laboratory tests.
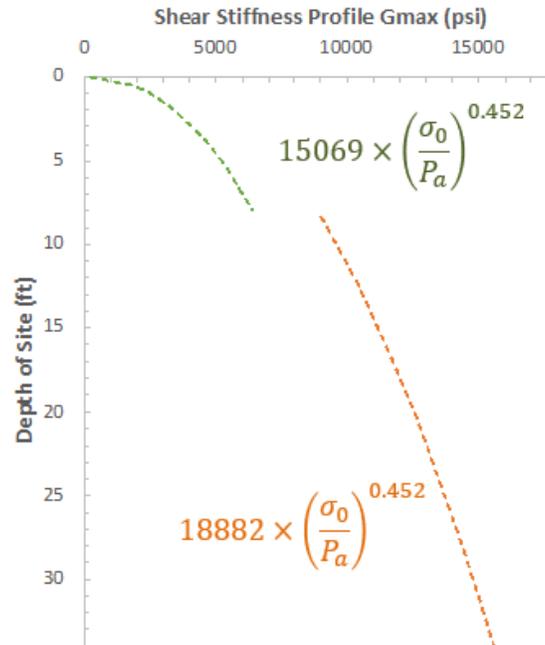
Figure 3.45 Digitized maximum shear stiffness profile for Mustang Island Test

Table 3.13 Input parameters of Mustang Island Sand in Abaqus

	Zone 1	Zone 2
C_{G1} (psi)	15069	18882
n_G	0.452	0.452
$C_1(\%)$	0.078	0.078
C_2	0.4	0.4
C_3	0.95	0.95
C_4	0.0	0.0
α_a	0.001	0.001
α_b	0	0
α_c	0.001	0.001
γ' (pci)	0.0333	0.0333

Figure 3.46 shows the comparison between the lateral load versus the load point displacement curve predicted using the soil parameters listed in Table 3.13. The predicted load-displacement curve captures the non-linearity at small displacements and has a good agreement with the field measurement.
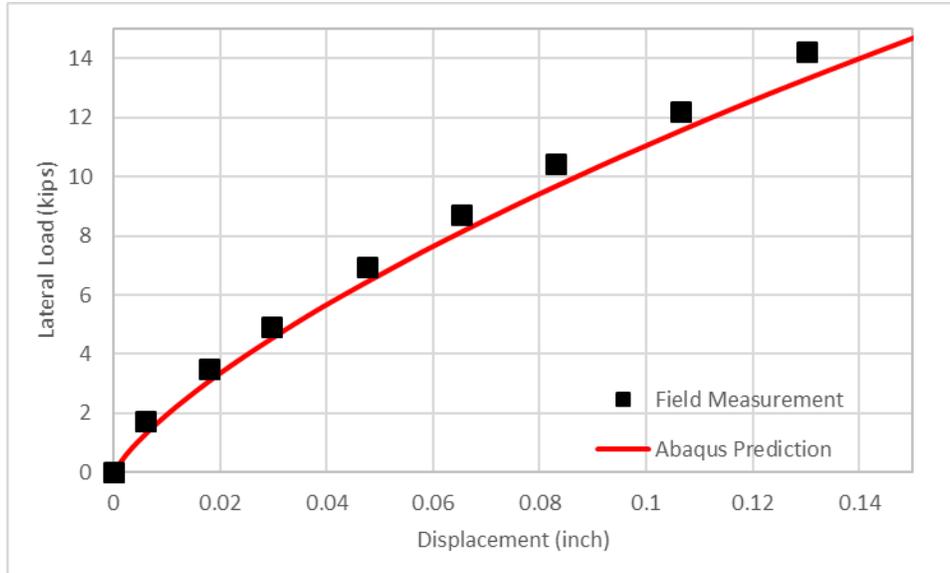
Figure 3.46 The comparison between the Abaqus prediction and field measurement

3.4.5.3 LPILE Analysis with Traditional Properties of Sand

LPILE is a program used in practice to predict the response of the piles under lateral loading conditions. LPILE has a database of p-y curves for a variety of soil types: the "API" p-y curve was chosen in the LPILE analysis to simulate the behavior of the pile under lateral loading.

The pile dimensions and the properties of the sand are the same as the description in Reese, Cox, and Grubbs (1974).

3.4.5.4 Comparison of the Numerical Modeling Results

Figure 3.47 shows the comparison between the Abaqus prediction and the LPILE prediction. The range of the displacement is 0.5% of the diameter of the pile. The prediction from LPILE based on API p-y method underestimates the stiffness in the range of the small displacement and does not predict the non-linearity of the response. The prediction from Abaqus has a good agreement with the field measurement and captures the well the decrease of the pile stiffness with increasing lateral displacement. As further check of the numerical model, the full range of displacement is shown in Figure 3.48; the Abaqus prediction matches well with the measurements at both small displacements (Figure 3.47) and large displacements (Figure 3.48).
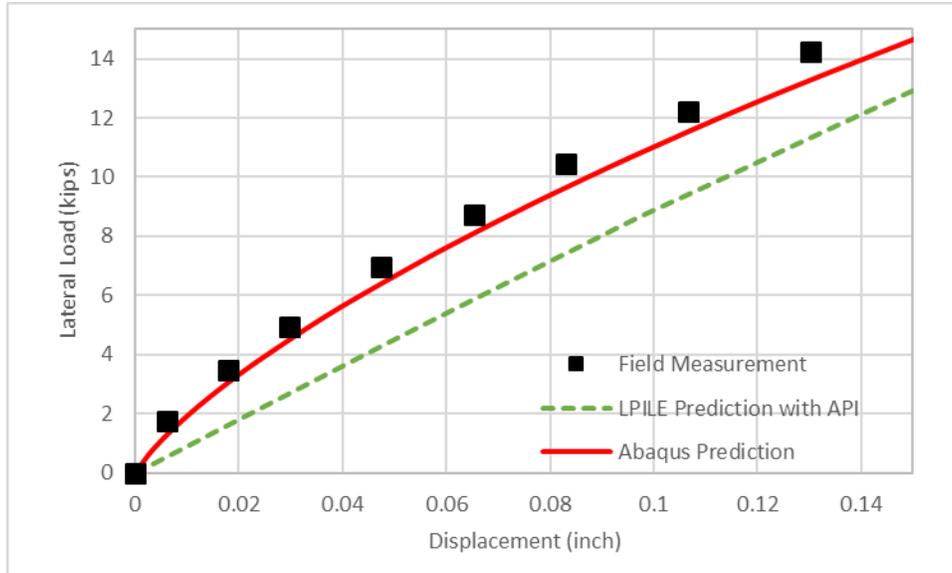
Figure 3.47 Comparison of the numerical modeling results (displacements less than 0.5% diameter of the pile)
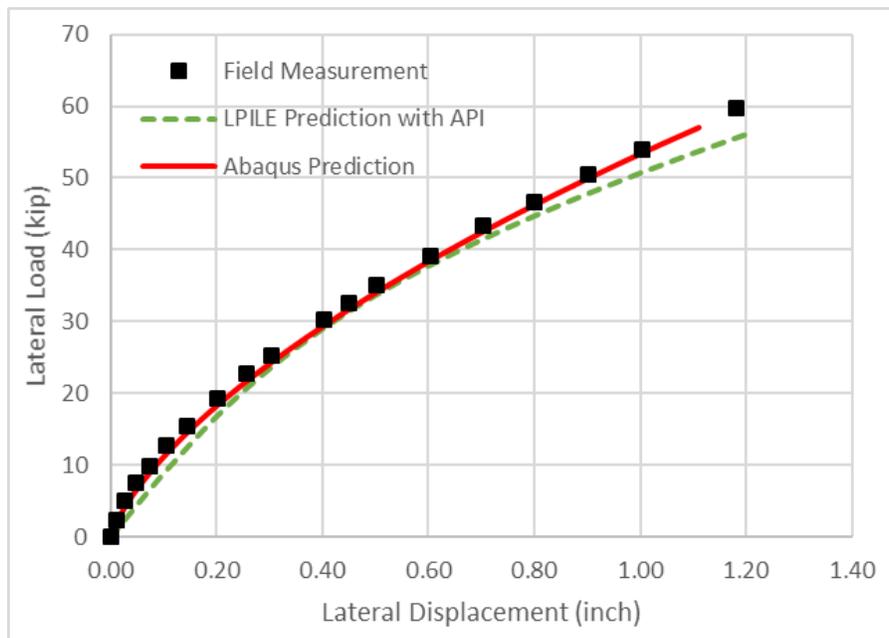
Figure 3.48 Comparison of the numerical modeling results (full range of displacements)

3.4.5.5 Influence of Tip Resistance on Lateral Response

A series of 3-D finite element models with different L/D ratios was performed to study the influence of the base shear on the lateral load response at the top of the pile. The diameter of the pile was 236 inches and the length changed with the L/D ratio. The soil was modeled using the subroutine of the proposed soil constitutive model and the sand properties were the same as the Mustang Island soil.

The tip resistance begins to play a role when the L/D ratio is less than 8 (Figure 3.48); this conclusion is consistent with PISA project results and recommendations (Byrne et al. 2017). For the lateral displacement level associated with the Belwind offshore turbines under service loading conditions (less than 0.05%), the tip resistance contributes very little even for L/D ratios as low as five (Figure 3.48).
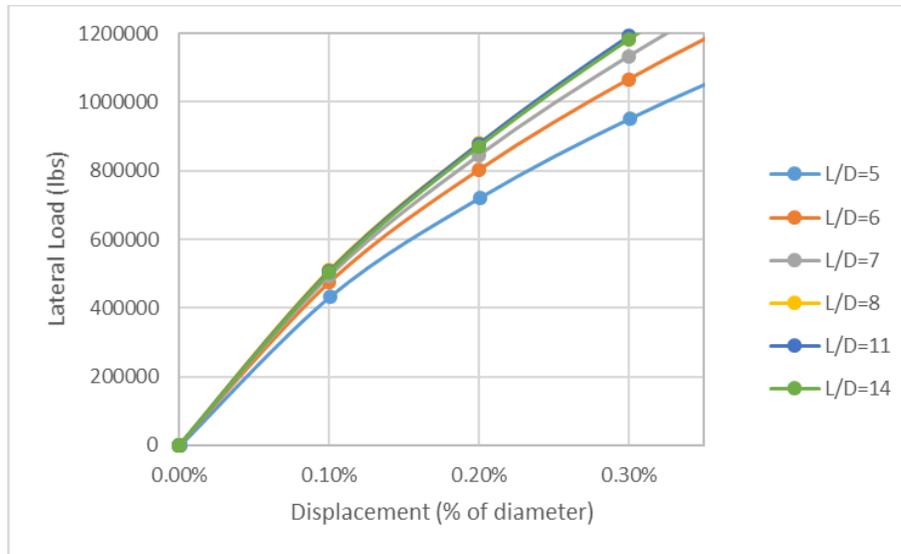
Figure 3.49 Finite element model results with laterally loaded 236-inch diameter monopiles in Mustang Island Sand

3.5 Conclusions

1. The proposed constitutive model for sand (Menq 2003) matches the nonlinearity of the sand stiffness at small strains based on dynamic laboratory tests conducted on two different samples of sand, (1) the sand used in laboratory model tests and (2) the sand from Mustang Island.
2. The proposed constitutive model for sand allows for changes in stiffness (and in future work the volume) to occur with cyclic loading.
3. The numerical model does well at predicting laboratory element tests in static and cyclic loading (e.g., torsional shear and dynamic triaxial tests).
4. In the analysis of the Mustang Island lateral load field tests, the predicted response of the pile matches well with the measured results from the field-measured shear velocity and resonant column and torsional shear tests on laboratory specimens. The conventional p-y method underestimates the pile stiffness in the range of the small displacement and does not predict the non-linearity of the response.
5. Based on a parametric study, the tip resistance at the base of a monopile in sand plays a role for lateral displacements up to 0.25% of the pile diameter when the ratio of the length to the diameter of the pile (L/D) is less than about 8. However, for the small lateral displacements associated with service loading conditions for the Belwind offshore wind turbines (less than 0.05% of the pile diameter), the tip resistance is negligible even for L/D ratio less than 5.

4 Lateral Load Model Tests

Laboratory model tests are being conducted to better understand the soil-structure interaction for a monopile in sand. The objective is to gain insight into behavior of the sand, but not to directly represent the performance of a full-scale pile driven in sand due to the difference of scale, stress state, and installation between a model and the field. To simplify the structure part of the problem, a sphere is being used to load the sand.

Laboratory testing consists of grain size analyses, torsional shear tests, dynamic testing using geophones to capture P-wave and S-wave velocities, and horizontal pushing test on the sphere. The following sections describe the details of the tests.

4.1 Properties of All-Purpose Sand

Sieve analysis, torsional shear tests, and triaxial tests were carried out to determine the properties of All-Purpose Sand. All the results from the tests were converted into the input parameters used for 3-D finite element modeling.

4.1.1 Sieve Analysis

The medium dense siliceous sand test bed was prepared in the tank using All-Purpose Sand. The grain size analysis of the sand presented in Table 4.1, Table 4.2, and Figure 4.1 shows that the grain size of the sand is fairly uniform.

Table 4.1 Sieve analysis on All-Purpose Sand

Sieve #	Opening (mm)	Wo (g)	Wf (g)	Wsoil (g)	Cum. Retained (g)	Passing
4	4.75	762.8	766.2	3.4	3.4	100%
8	2.3600	682.8	866.4	183.6	183.6	91%
20	0.8500	588.8	1263.6	674.8	858.4	59%
30	0.6000	609	914.4	305.4	1163.8	46%
40	0.4250	577.5	850.6	273.1	1436.9	33%
50	0.3000	332.3	595.2	262.9	1699.8	23%
100	0.1500	522.6	929.4	406.8	2106.6	5%
140	0.1060	357.9	416.9	59	2165.6	2%
200	0.0750	341.8	373.8	32	2197.6	1%
Pan	0.0000	383	396.4	13.4	2211	0%
Lid	-	241.9	241.9	0	2211	
Totals		5400.4	7614.8	2214.4		

Table 4.2 Coefficients of uniformity C_u and curvature C_c of All-Purpose Sand

	All-Purpose Sand
D_{10}	0.19 mm
D_{30}	0.38 mm
D_{50}	0.67 mm
D_{60}	0.87 mm
C_u	4.6
C_c	0.92
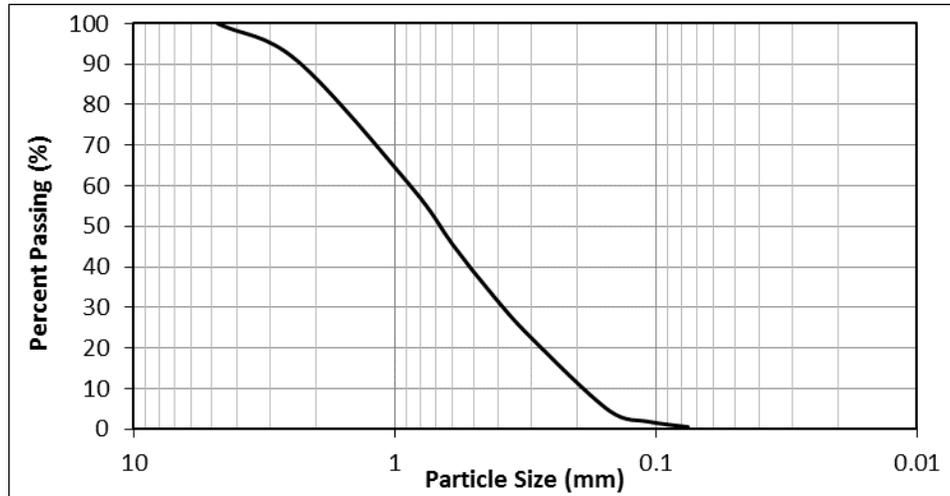
Figure 4.1 Gradation curves of All-Purpose Sand

4.1.2 Torsional Shear Test

The torsional shear test is used to determine shear modulus, G, and the damping ratio, D, at small shear strains. These values are determined by stress and strain levels. The shear modulus and damping ratio are measured by increasing the stress or strain level step-by-step. The test was done on All-Purpose Sand in the Soil Dynamic Laboratory at The University of Texas at Austin. The detailed results of the tests are attached in the Appendix D.

As shown in the element tests, the empirical equations provided by Menq (2003) cannot predict the magnitude of G_{max} and the relationship of $G/G_{max} - log\gamma$ accurately. The empirical equations need to be modified based on torsional shear tests.

R-squared method was used to find the regression lines of G_{max} and $G/G_{max} - \log\gamma$ to best-fit the data measured in the torsional shear tests. Based on a preliminary numerical modeling, the largest stress in the sand caused by pushing the ball is less than 4psi. The regression analysis on the relationship between confining pressure and G_{max} was performed up to the confining pressure (8 psi). The regression analyses on the relationship of the $G/G_{max} - \log\gamma$ curves were performed on the curves with 2 psi and 4 psi confining pressure.

The calibration procedure was shown in section 3.3.5.2 and the soil properties which best-fit the dynamic laboratory tests are listed in Table 4.3 (same as Table 3.9).

Table 4.3 Input parameters for All-Purpose Sand in Abaqus

C_{G1} (psi)	n_G	C_1 (%)	C_2	C_3	C_4
18652	0.44	0.036	0.296	0.95	0.1

4.1.3 Conventional Triaxial Tests

Three additional conventional triaxial tests were carried out to complement the limitation that the largest shear strain in the torsional test was up to 0.1%. The conventional triaxial tests were used to calibrate the 1-D axial loading element tests when the octahedral shear strain was larger than 0.1%. The density and the dimension of the sand sample during triaxial tests were controlled to be the same as in torsional shear tests. The levels of the confining pressures were chosen to be 2 psi, 4psi, and 8psi, which also were the same with the torsional shear tests.

Before calibrating the $G/G_{max} - \log \gamma$ curves, the parameters in Table 4.3 were used in the 1-D axial loading element tests. The comparison between the numerical modeling and the triaxial tests was shown in Figure 4.2. The numerical modeling overestimated the stiffness when the confining pressure was low, but it underestimated the stiffness when the confining pressure went higher.
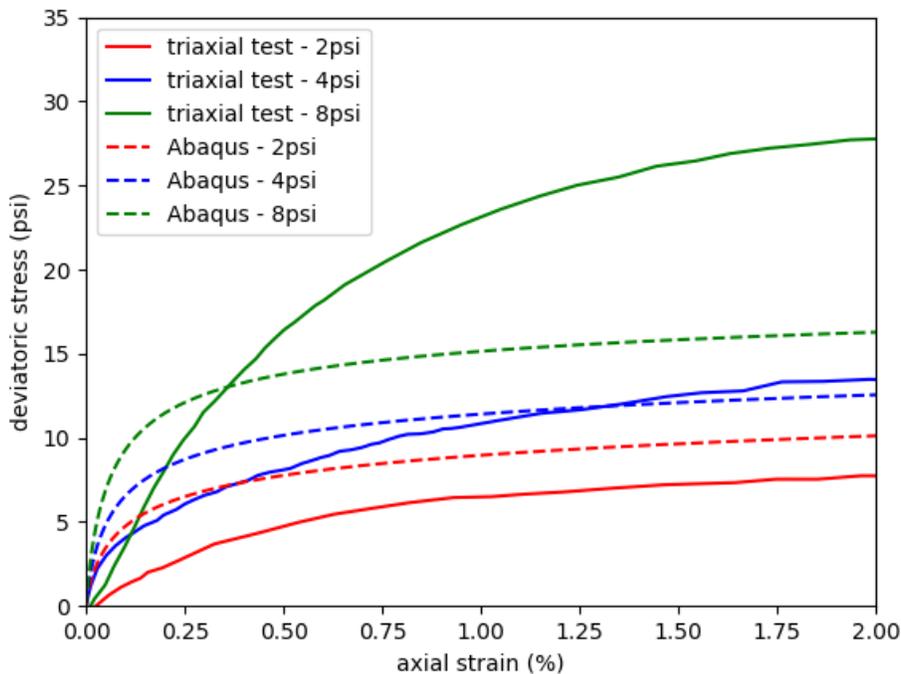
Figure 4.2 Comparison between the 1-D element axial loading tests and triaxial tests (All-Purpose Sand, before calibration)

The calibrated properties of All-Purpose Sand are listed in Table 4.4. Figure 4.3 shows the comparison between the numerical modeling and the measurement after calibration. The results of the 1-D axial loading element tests had good agreements with the triaxial tests when the strain was larger than 1%. The triaxial tests could not measure the stiffness of the sand sample under 1% accurately, so the 1-D axial loading element tests did not try to match the curves in the range of small strain.

Figure 4.4 shows the $G/G_{max} - \log \gamma$ after calibration, the calibrated curves still have good fit with the measurement of the torsional shear tests under shear strain 0.1%. So, the calibration had little influence on the stiffness in the small shear strain and it made the $G/G_{max} - \log \gamma$ curve perform better in the large shear strain.

Table 4.4 Input parameters for All-Purpose Sand in Abaqus (after calibration)

C_{G1} (psi)	n_G	C_1 $(\%)$	C_2	C_3	C_4
18652	0.44	0.062	0.8	1.0	0.13
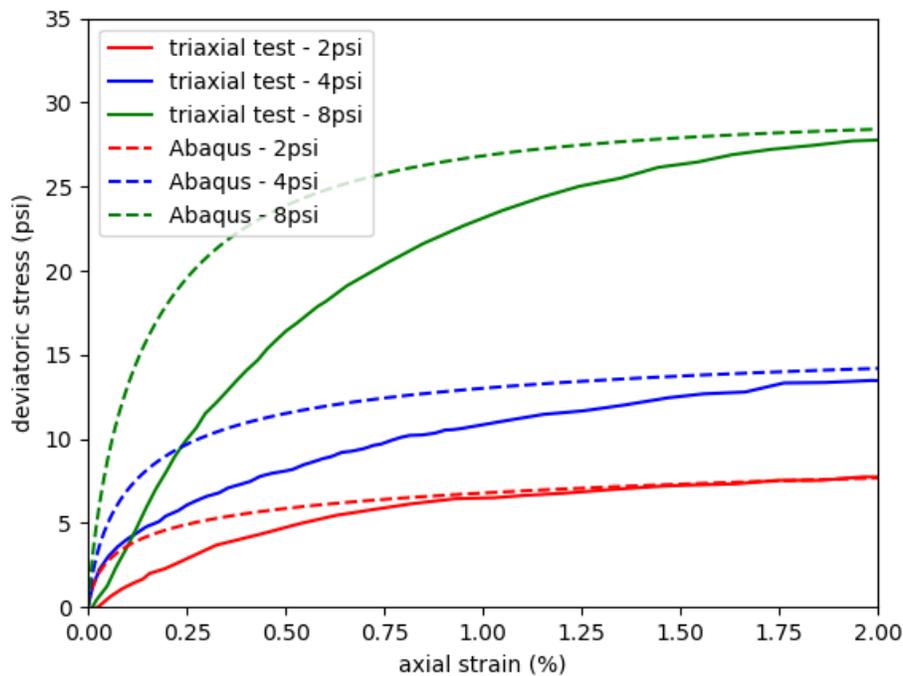
Figure 4.3 Comparison between the 1-D element axial loading tests and triaxial tests (All-Purpose Sand, after calibration)
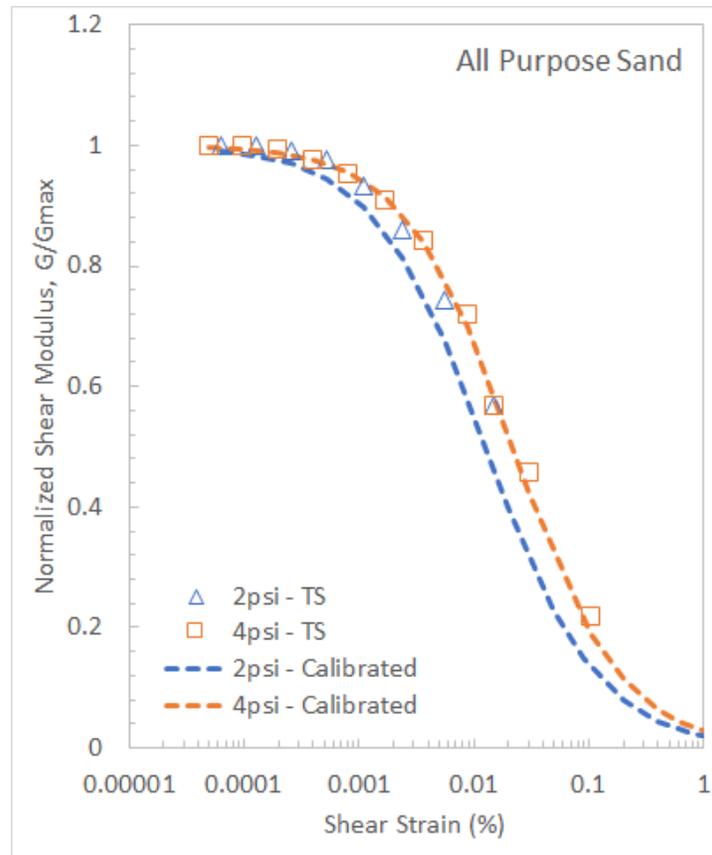
Figure 4.4 Calibrated relationship of $G/G_{max} - \log \gamma$ (All-Purpose Sand)

4.2 Push Tests on Spheres

In the experimental push tests, three different diameters spheres were pushed horizontally into All-Purpose Sand in the wood tank. The spheres were pushed using a long, slender loading rod and the applied force was measured directly behind the spheres. The horizontal displacement was measured directly on the loading rod using a high resolution LVDT. The tests were prepared in a manner simple enough to repeat confidently and conducted precisely. Final tests included monotonic loading tests and cyclic loading tests.

4.2.1 Development of Testing Equipment

4.2.1.1 Sand Tank

The sand tank was built by wood and under three considerations: (1) good interaction of the sand tank with the soil and the testing equipment to minimize the noise especially during seismic wave tests; (2) enough structure capacity with little deformation when filled with sand; (3) requirements on labor, time, and space involved in preparing each experiment. Figure 4.5 shows a rendering of the sand tank used in push tests. The wood tank was built to a modular structure to allow for the creation of different tank dimensions.
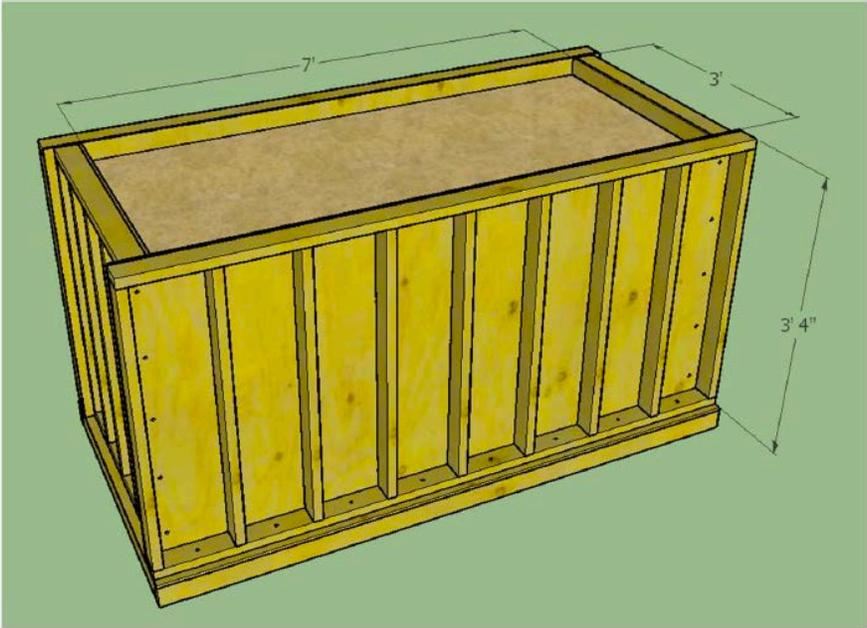
(a)
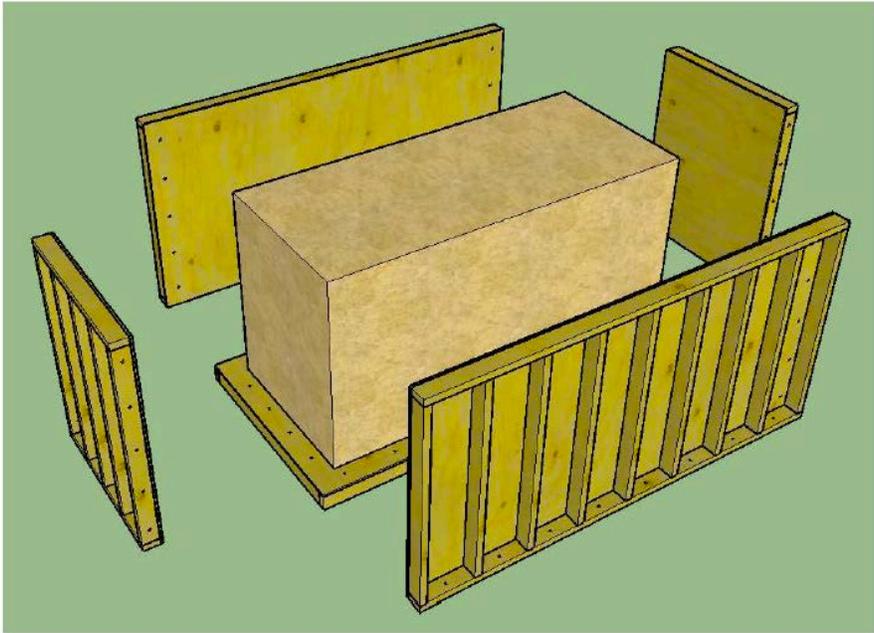
(b)

Figure 4.5 Large, modular soil tank; (a) largest volume configuration, (b) exploded component view

4.2.1.2 Spheres

Spheres of multiple diameters were fabricated from acrylic. The acrylic spheres had a specific gravity of 1.19. Using a material with a specific gravity lower than that of soil body ensured no extra load was applied to the soil body, possibly artificially strengthening the soil before testing.

Figure 4.6 shows the picture of three spheres at 2'', 3'', and 4'' diameters from left to right.

Figure 4.6 Spheres; 2'', 3'', and 4'' diameter

A circular cavity was bored into each sphere to house a load cell. In this cavity a small hole was drilled, into which a small threaded housing was fixed. Recessing the spheres in this manner helped reduce the area of objects in contact with the soil other than the spheres. The cavity and threaded connection machined into each sphere were both shown in Figure 4.7.

Figure 4.7 Sphere recessed cavity and connection to load cell

4.2.1.3 Loading Apparatus

There were four major components of the testing apparatus: (1) a load frame capable of linear displacement at low speeds; (2) a loading rod to transfer motion from the load frame to the sphere; (3) a sphere; and (4) a load cell between the loading rod and the sphere. Figure 4.8 shows an overview of the entire loading system.
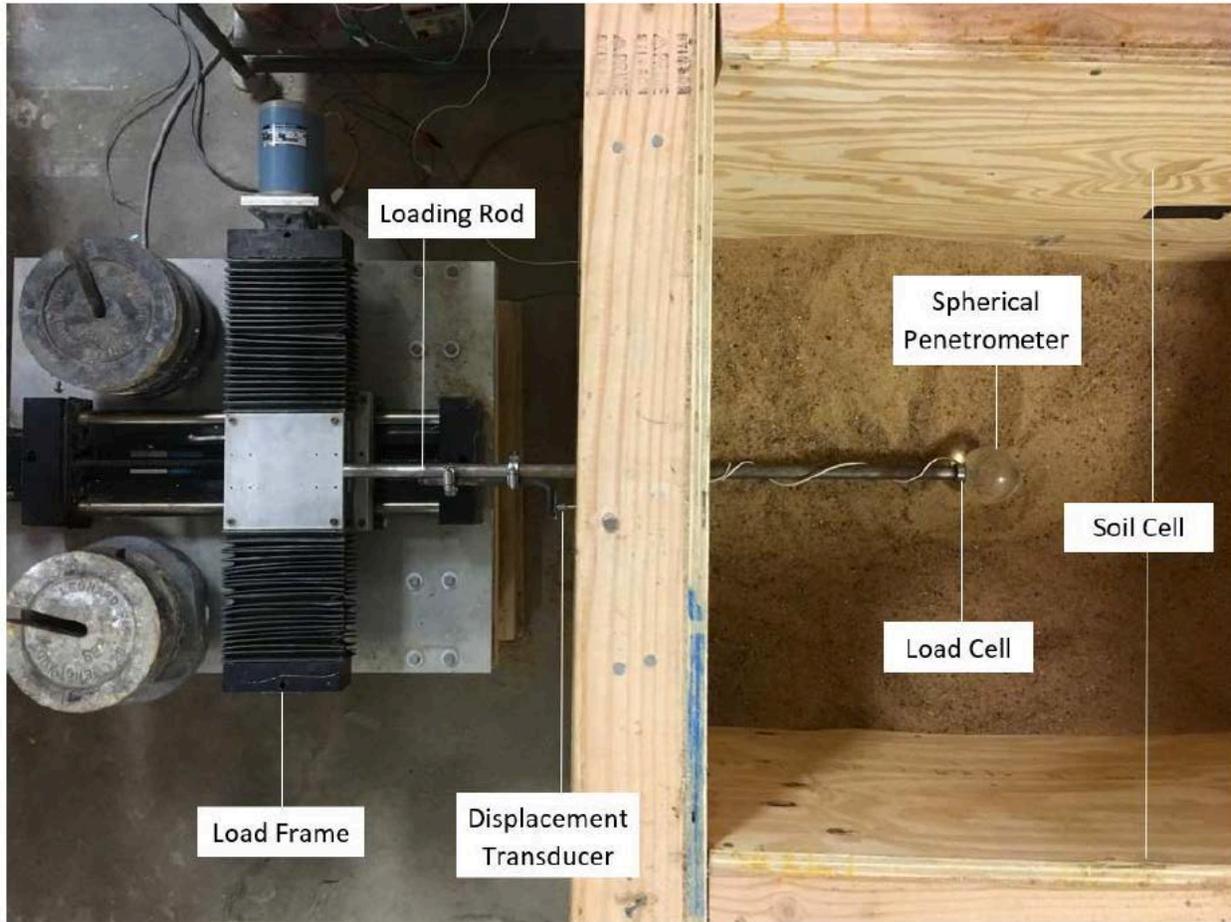
Figure 4.8 Overview of final testing setup

A biaxial load frame with a capacity of 70 pounds and a minimum travel speed of 0.0002 in/s was used to conduct each test. The load cell was connected to both the loading rod and the sphere to measure the load close to the soil-sphere interface. Figure 4.9 shows the detailed plan of the assembly of these three components.
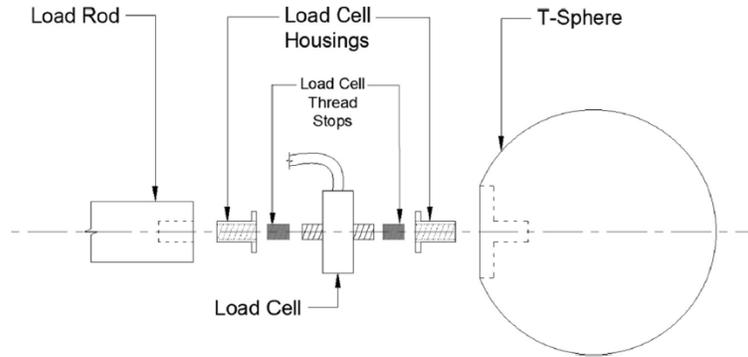
(a)
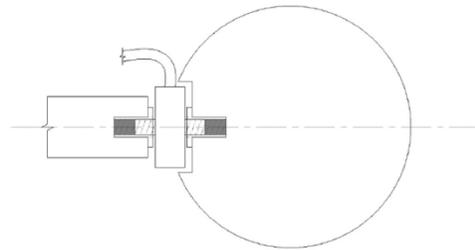
(b)

Figure 4.9 Assembly of loading rod, load cell, and sphere; (a) exploded view, (b) assembly

4.2.2 Sand Placement Procedure for Push Tests

Developing a consistent procedure for the advanced tests was critical in obtaining reliable and repeatable results. The procedure included methods for placing the sand around the sphere but also establishing a method to measure the void ratio of the sand.

The first step in each test was to fill sand to the bottom of the ball and to place an empty container of known weight and volume in the corner of the test to determine the void ratio of the sand. The sand was then pluviated around the sphere and into the container using a funnel. The funnel was used to mitigate separation between larger than smaller particles of sand. This was observed in some of the initial tests, where larger particles tended to roll down sand down while smaller particles would stay on the slopes. This created a distribution of particles, which made it impossible to accurate determine the gradation of the sand. Hence, using the funnel to place the sand around the sphere ensured a consistent gradation of sand particles around the sand. Furthermore, using the funnel to fill the container ensured an accurate void ratio measurement of the sand around the ball.

Once the sphere was buried, additional sand was added to the sand tank using pluviation from 5 gal buckets. The pluviation was done from a constant drop height of approximately 6 in. to ensure a consistent gradation throughout the sand tank. Once the sand reached the top of the sphere, the surface was flattened.

The final step was then to pluviate more sand into the tank to a target embedment depth. Embedment depths for the advanced tests were 10 and 20 in. Once the embedment depth was reached, the push test of the sphere began. Figure 4.10 shows a summary of the procedure for the advanced tests.

1. Fill the sand up to the bottom of the sphere	2. Place the sphere and the loading rod, make sure the bottom of the sphere touches the sand
3. Use a funnel to pluviate the sand around the sphere to the top of the sphere	4. Pluviate the sand from buckets to fill the sand to the top of the sphere and flatten the surface
5. Fill the sand up to the target height using the pluviation from buckets	
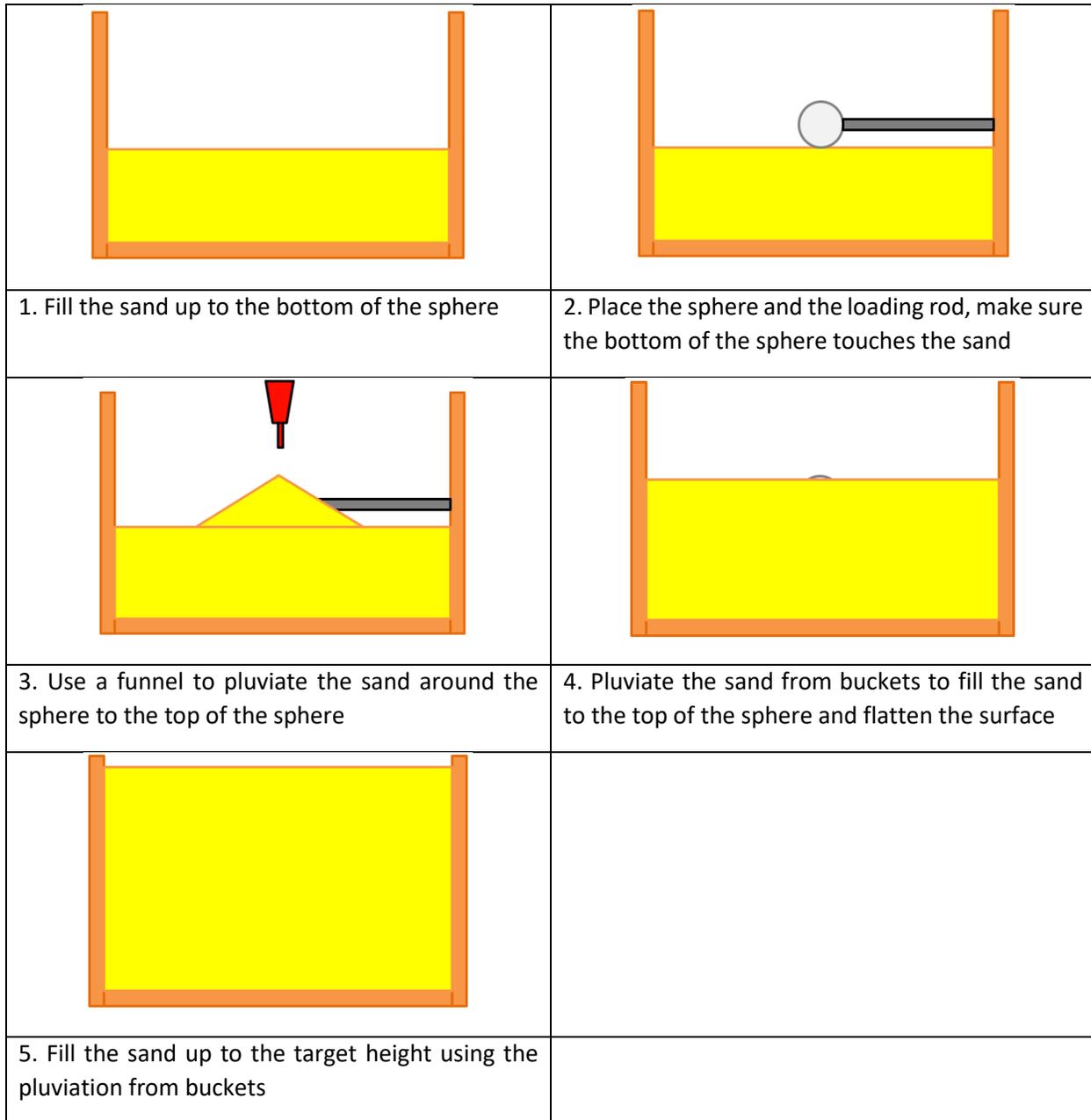
Figure 4.10 Procedure for preparing the sand bed

4.2.3 Geophone Testing

The maximum shear stiffness G_{max} and Poisson's ratio υ of the soil are important inputs of the developed soil constitutive model. Geophone tests were carried out in the sand tank to measure the shear wave (S-

wave) velocity and the confined compression wave (P-wave) velocity. The measured S-wave velocity can be used to calculate G_{max}, and the P-wave velocity along with the S-wave velocity allows the calculation of υ of the soil.

4.2.3.1 Dynamic Tests Equipment

The following equipment was used to perform the dynamic tests:

- 4.5-Hz geophones as sources,
- 28-Hz geophones (GS-14-L3 epoxied inside plastic cases for protection) as receivers,
- BNC cables,
- Function generator (Keysight 33210A) to excite the source geophone, and
- Dynamic signal analyzer (Quattro by Data Physics) to record received signals

Figure 4.11 4.5-Hz geophone

Figure 4.12 28-Hz geophones (GS-14-L3 epoxied inside plastic cases for protection)

Figure 4.13 Function generator (Keysight 33210A)

Figure 4.14 Dynamic signal analyzer (Quattro by Data Physics)

4.2.3.2 Dynamic Tests Set Up

The method used for measuring the S-wave and P-wave velocities in this study was similar in configuration to in-situ cross-hole testing where a source is used in one borehole and two geophone receivers are used in adjacent boreholes. In this test, the sources and receivers were embedded at the required depth (the depth where the push tests were performed) and covered with sand. The sand bed was prepared by the same way as in the push tests to make sure the condition of the sand bed was the same.

Figure 4.15 shows the 3-D layout of the geophones during dynamic tests and Figure 4.16 shows the dimension of geophones and the spacing. The geophones layout consists of two linear arrays, one with vertical geophones for measuring S-wave velocity and the other with horizontal geophones for measuring P-wave velocity. The vertical source geophone was used to generate horizontally propagating vertically polarized S-waves (S_{HV}), while the horizontal source geophone was used to generate horizontally propagating P-waves (P_H).
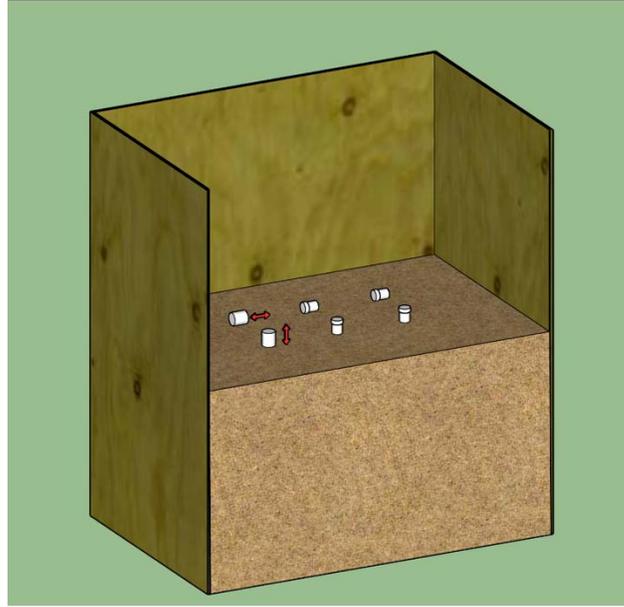
Figure 4.15 3-D Layout of the geophones inside the sand tank (before sand filled to top)
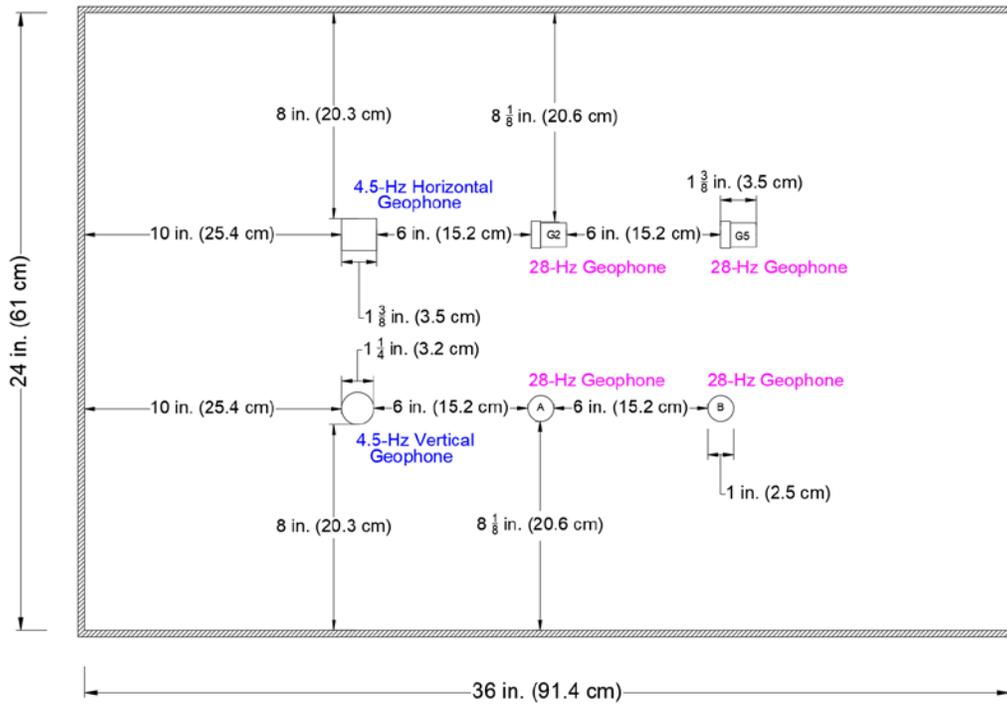
Figure 4.16 2-D Layout of the geophones inside the sand tank
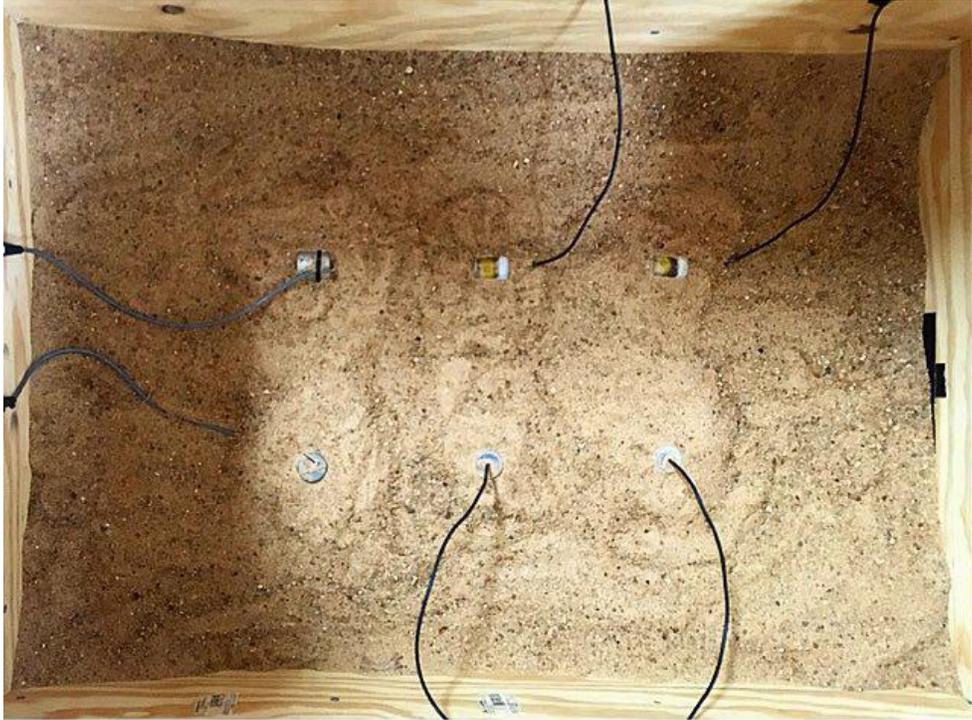
Figure 4.17 Geophones placed inside the sand tank
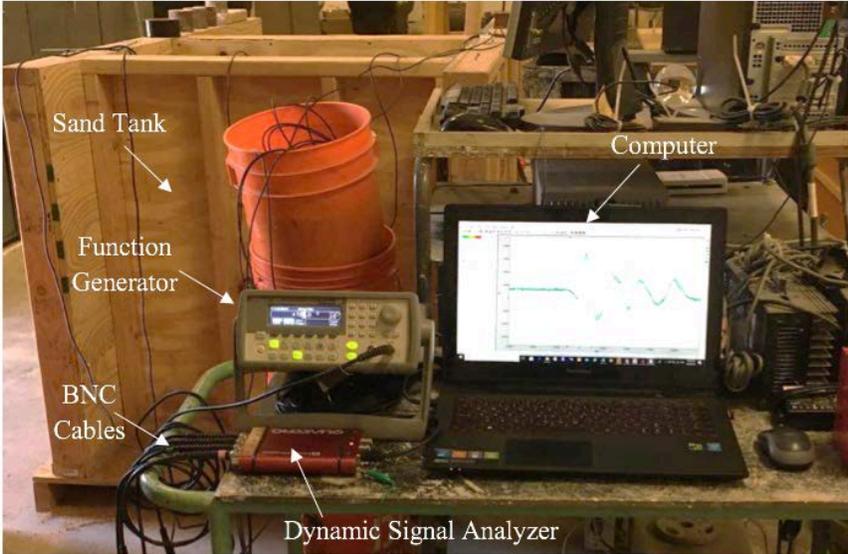
Figure 4.18 Set up used for generating waves and recording the signals

4.2.3.3 Dynamic Tests Procedure

The following steps were taken to prepare the sand bed inside the sand tank:

1. The sand was removed to the required depth
2. The surface at the required depth was leveled
3. The geophones were carefully placed at the proper locations. The distances between the geophones were checked multiple times before continuing the next step.
4. The sand was lightly pluviated using a funnel around the geophones to insure no gap between the geophones and the sand as in the push tests
5. The remaining sand was pluviated up to the required height using buckets (drop height of 6 inches was used just as done in constructing the sand bed in the push tests).

Since the push tests were conducted at two different depths (10 inches and 20 inches), each dynamic test was also carried out in two stages. The measurements at the first stage were done with 10 inches for soil above the geophones, followed by the second stage where 10 more inches of soil was added, and the measurements were carried out for 20 inches embedment depth.

The dynamic test started by using the function generator to trigger the horizontal or the vertical source geophones to generate propagating waves in the soil. The waves were recorded by the receiver geophones. Based on the time difference between the wave arrival at the two receiver phones Δt and the known front-to-front distance between the receiver geophones Δd, the wave velocity was calculated using the basic velocity equation $v = \frac{\Delta d}{\Delta t}$.

4.2.3.4 Dynamic Tests Results

Five independent two-stage (10 inches and 20 inches embedment depths) dynamic tests were conducted to verify the repeatability of the measured values. In each stage, 10 runs were taken for each wave type (i.e. S-wave and P-wave). Table 4.5 summarizes the velocities derived from these tests.

Table 4.5 Results of geophone testing

Derived Parameter	Embedment depth of 10 inches	Embedment depth of 20 inches
VS (fps)	330 ± 10	380 ± 15
VP (fps)	510 ± 15	570 ± 25
v	0.15 ± 0.06	0.12 ± 0.06

The deviation of the measurement was caused by: (1) the uncertainty in picking wave arrival times; (2) the variation in the soil structure around the geophones, geophone spacing, and environmental noise.

4.2.4 Results of Push Tests

The push tests consisted of monotonic loading test and cyclic loading tests. The monotonic loading tests were performed with 2-, 3-, and 4-inch spheres and were embedded either 10 or 20 inches. The cyclic loading tests were performed on 3- and 4-inch spheres and all were conducted at an embedment depth of 20 inches.

4.2.4.1 Monotonic Loading Tests

Three penetrometer diameters and two embedment depths totaled six possible monotonic test scenarios. Figure 4.19 to 4.24 show the tests results of the 2-, 3-, and 4-inch spheres, respectively, at 10 and 20 inches of embedment. The curves have been truncated to 0.25% of the respective sphere diameter. The in-situ void ratio of the sand used for each test was measured. The void ratio was controlled to be approximately 0.56 for each test which was the same in the torsional shear tests and the geophone tests.

All the tests results have fairly good repeatability. The reason that the tests for the 3-inch sphere have the largest deviation is because the 3-inch sphere was used to find the repeatable testing routine that would create consistent results. So, more tests were run on the 3-inch sphere and the other spheres were added later to evaluate the effect of varying sphere diameters. The tests for the 4-inch sphere at the embedment depth of 20 inches have the best repeatability. It is as expected that tests performed with a larger sphere at a deeper embedment depth would have better repeatability.
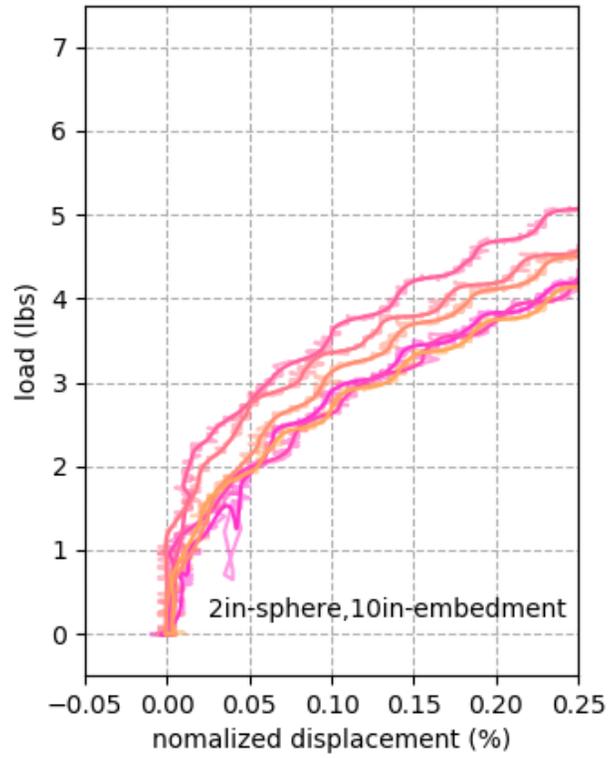
Figure 4.19 Push tests results for 2-in sphere at embedment depth of 10 in
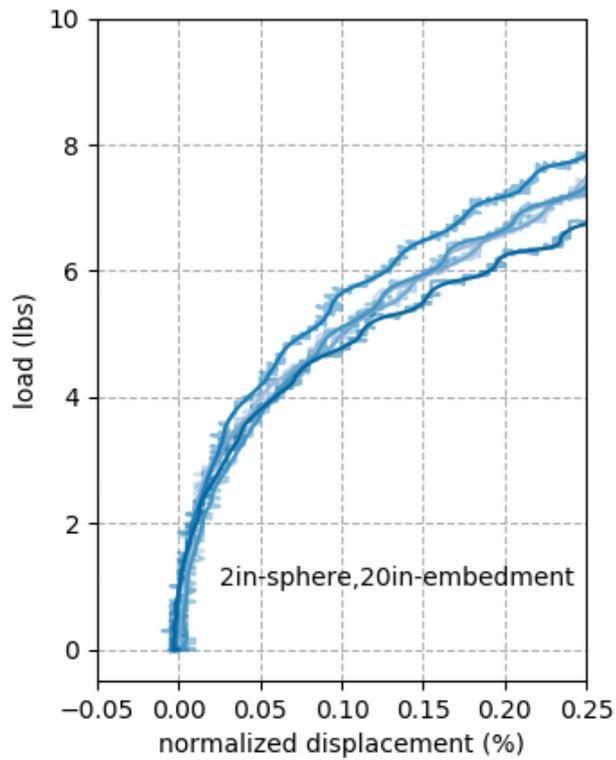
Figure 4.20 Push tests results for 2-in sphere at embedment depth of 20 in
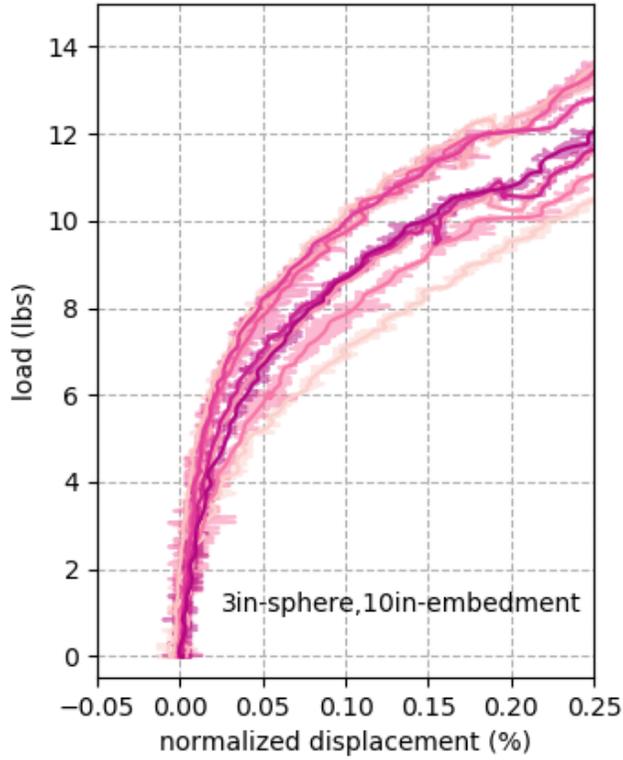
Figure 4.21 Push tests results for 3-in. sphere at embedment depth of 10 in.
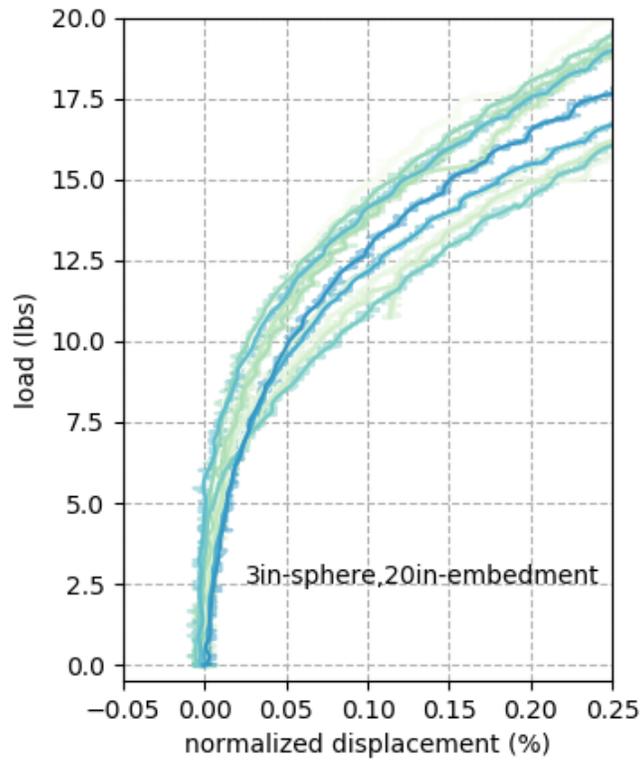
Figure 4.22 Push tests results for 3-in. sphere at embedment depth of 20 in.
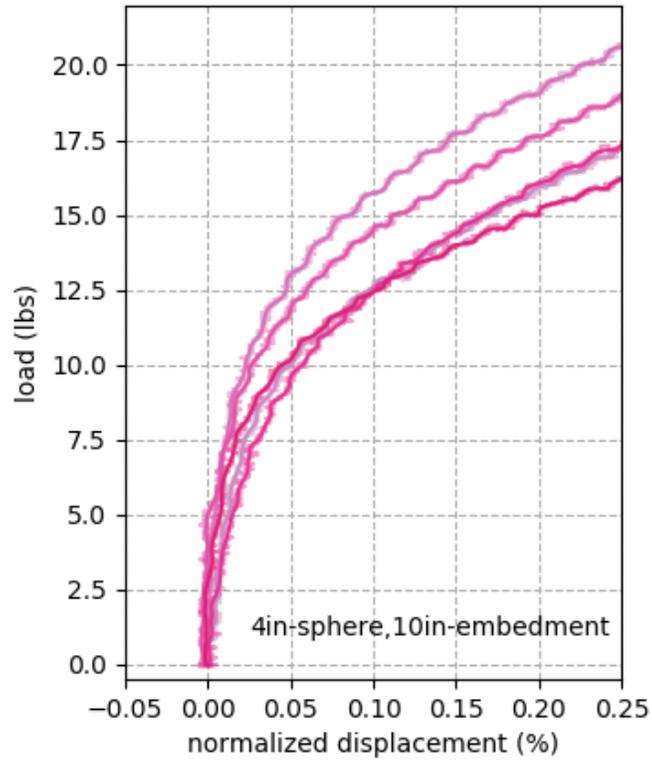
Figure 4.23 Push tests results for 4-in. sphere at embedment depth of 10 in.
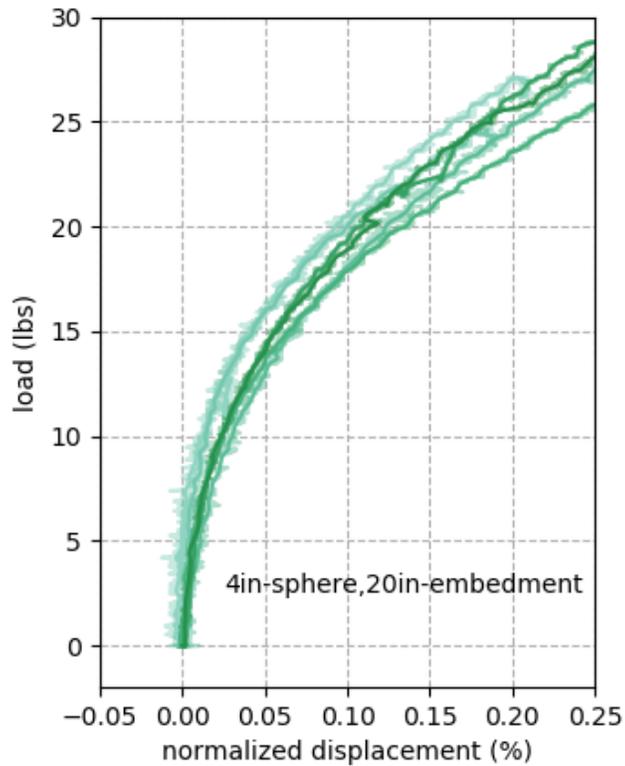
Figure 4.24 Push tests results for 4-in. sphere at embedment depth of 20 in.

4.2.4.2 Cyclic Loading Tests

A total of five cyclic loading tests were conducted, four with the 3-inch sphere and one with the 4 inches penetrometer, all conducted at an embedment depth of 20 inches. Of these, only two of the 3 inches sphere tests yielded intelligible results. Though only two tested produced clear results, there is good cause to believe these tests to be valid. The two valid tests were load-controlled tests.

Figure 4.25 shows the first reliable cyclic loading test on the 3-inch sphere at 20 inches of embedment. The sphere was displaced a nominal amount into the soil, on the order of 0.007 inches, to ensure good contact with the soil before cycling. After this initial displacement, 1,000 cycles of displacing the spheres between an approximately 5-lb range were completed, with an average lateral load 13.5 lb.
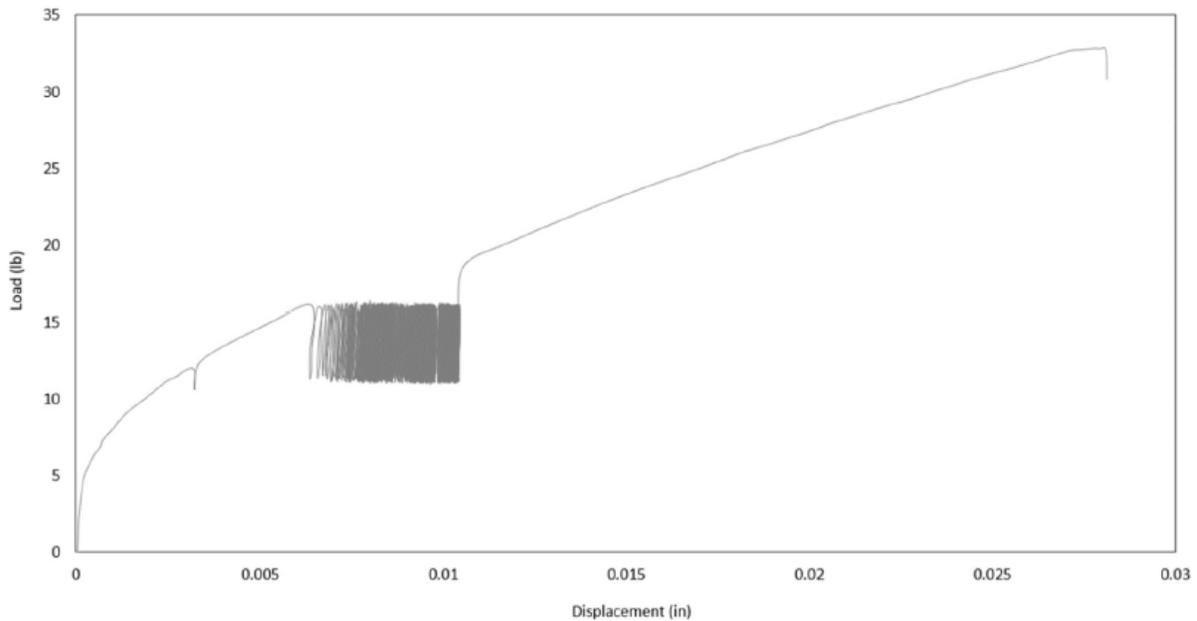
Figure 4.25 Overview of load-controlled cyclic load test; 3-inch sphere at 20 inches of embedment, 1,000 cycles

Figure 4.26 shows the hysteretic trend typical of cyclic tests. The permanent displacement range over an increment of 100 cycles is seen to decrease with the number of cycles completed, indicating the soil is approaching a steady state. Three ranges of 100 cycles are shown, the permanent displacement after the last increment of 100 cycles is over an order of magnitude less than that from the first 100 cycles.
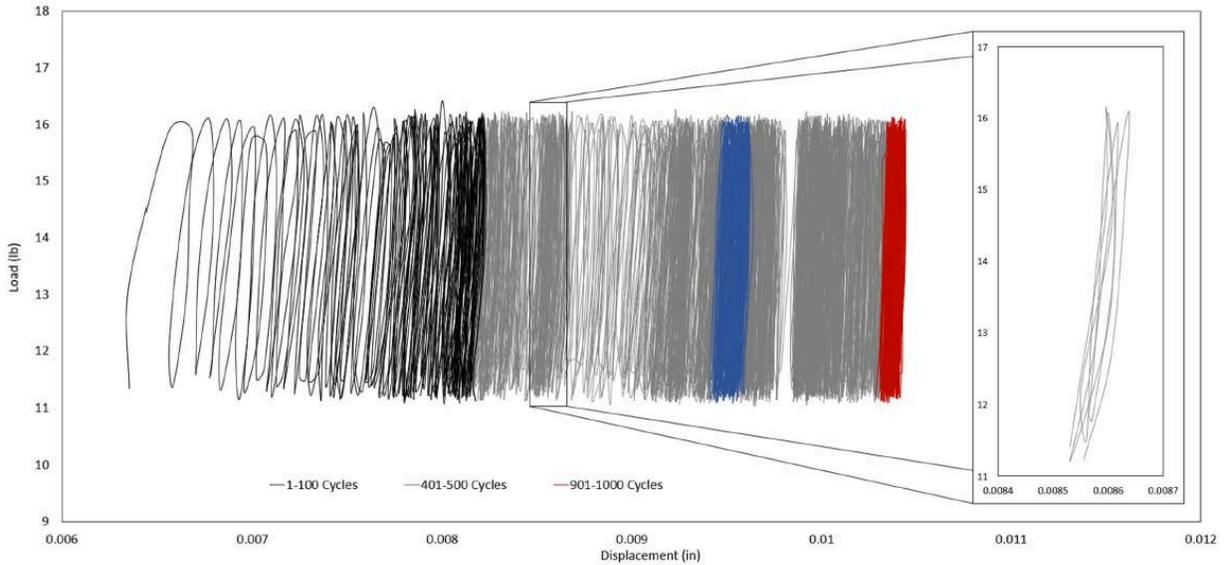
Figure 4.26 3-inch sphere, 20 inches of embedment cyclic test load-displacement trend

The secant stiffness of the push tests response was calculated as follows, $E_1 = \frac{\Delta P_1}{\Delta y_1}$ and $E_2 = \frac{\Delta P_2}{\Delta y_2}$ where $\Delta P_1, \Delta P_2, \Delta y_1,$ and Δy_2 are as defined as shown in Figure 4.27.
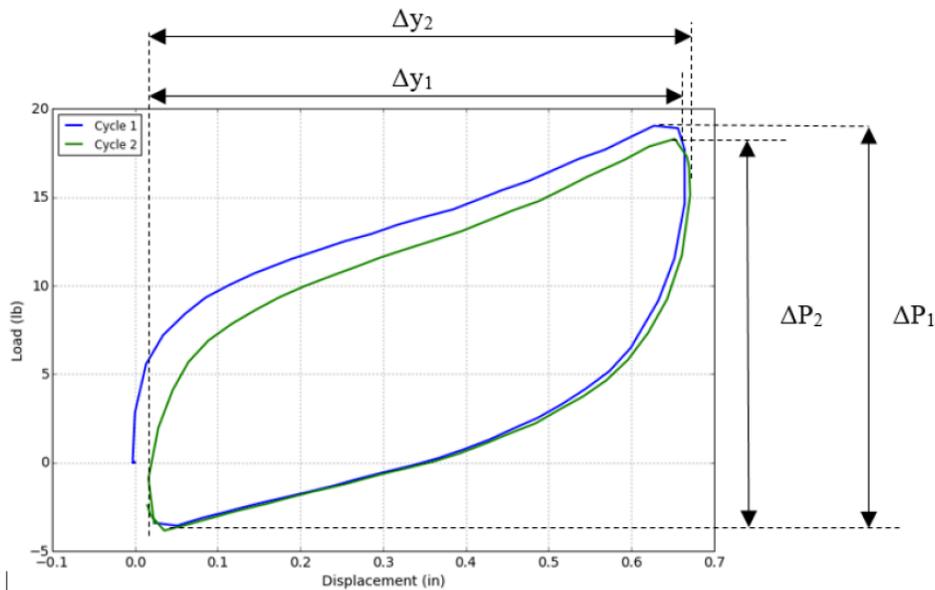
Figure 4.27 Calculation of secant stiffness of push test response (Senanayake 2016)

Figure 4.28 shows the harmonic mean stiffness over sets of 10 cycles for the first 100 cycles. The harmonic mean secant stiffness was used to rather than a simple average to better reduce the effect of the extreme outliers. Secant stiffness generally increases with number of cycles.

95
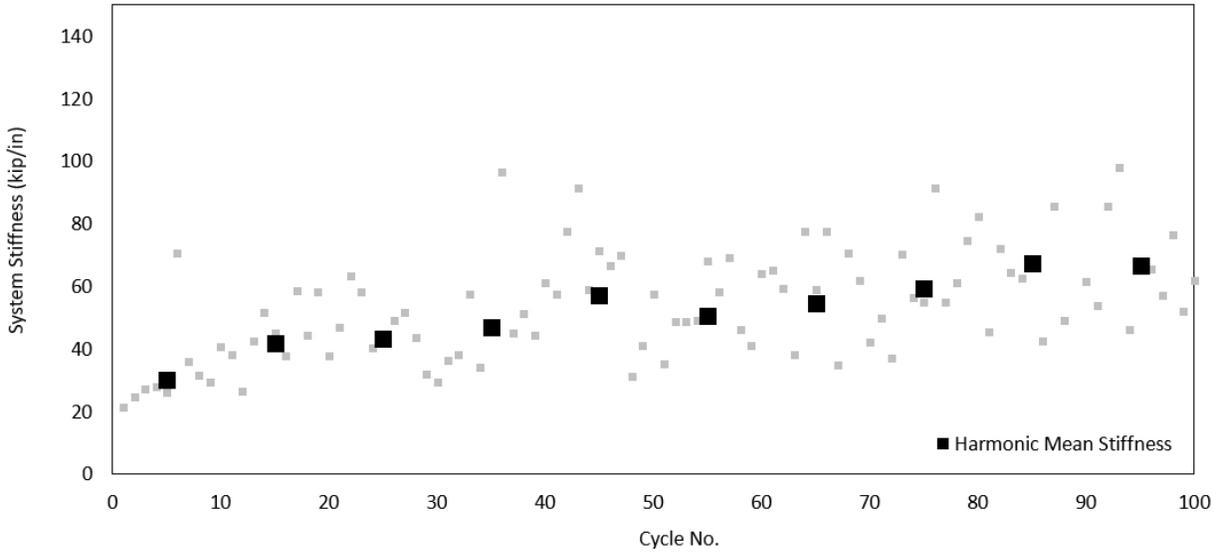
Figure 4.28 Cyclic test harmonic mean secant stiffness per 10 cycles

Figure 4.29 shows the second valid cyclic loading test with the 3-inch sphere at 20 inches of embedment depth. The test consisted of two stages: (1) 300 cycles of a 7.5-lb mean load and a 2.5-lb load amplitude; (2) 300 cycles of a 13.5-lb mean load equaling and a 2.5-lb load amplitude. After the completion of first stage, the sphere was loaded to start of the second stage.
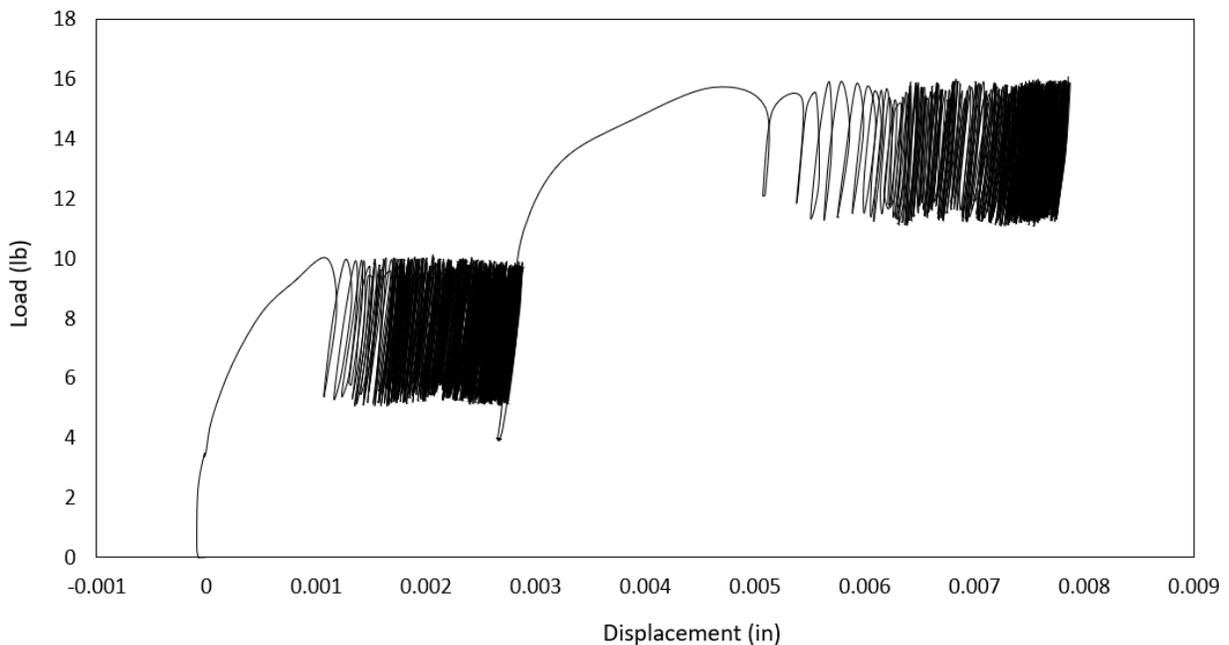
Figure 4.29 Overview of load-controlled cyclic load test; 3 inches spheres at 20 inches embedment, 300+300 cycles

As was previously observed in the first test, the permanent displacement in each hysteretic loop tends to decrease with the number of cycles. It indicates that the soil is stiffening and approaching a steady state. After the soil reaches a steady state at first stage and then the sphere is loaded to second stage, the steady

state is broken and the secant stiffness decreases. The secant stiffness restarts to increase with the number of cycles in the second stage and reaches a steady state again after an amount of cycling.

Figure 4.30 shows the changes of the secant stiffness in the two stages. The most increases of the secant stiffness are seen in the first 50 cycles of the two stages. The overall secant stiffness of the second stage is higher than the first stage. As expected, the second stage has higher mean load, which means the confining pressure of the soil in front of the sphere is higher. So, the second stage should have higher secant stiffness under the same amplitude of load.

4.3 Numerical Modeling of Push Tests

Several numerical models of Abaqus were built to simulate the push tests on the 2-, 3-, and 4-inch spheres at different embedment depths. The results obtained from numerical modeling were than compared to the laboratory tests.
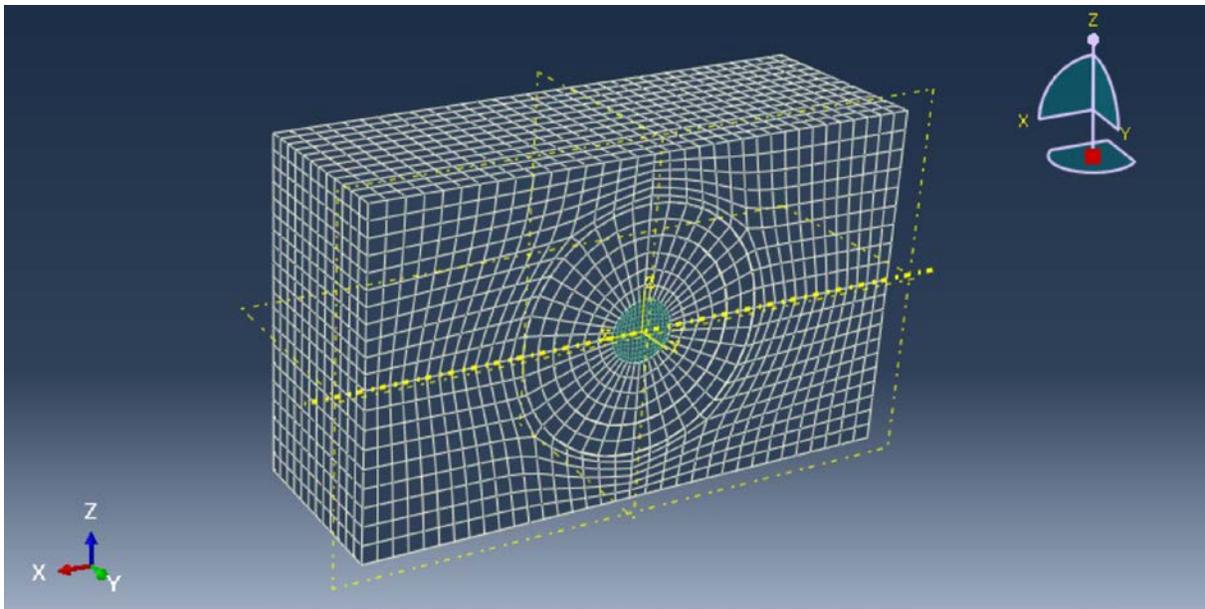
Figure 4.30 Abaqus model of push test on the sphere

The Abaqus model included three different parts: the sand body, the test sphere, and the interface. The horizontal loading on the test sphere implied a plane of symmetry in the problem geometry and therefore, only half of the geometry was discretized into the Abaqus model.

In the Abaqus model, the dimensions of the sand body were 36 inches in length and 12 inches in width. The height of the sand body was dependent on the embedment depth of the laboratory tests. The sphere was at the center of the sand body. At the base of the mesh, all three displacement components in the three-coordinate direction (X, Y, and Z) were set to zero. For the vertical boundaries on the Y-Z plane and the back boundary on the X-Z plane, the X and Y displacements components were set to zero. To ensure that the front boundary on the X-Z plane was a plane of symmetry, the displacement normal to this plane was set to zero. The sand material was modelled with the subroutine of the proposed soil constitutive

model. The input of the properties of the sand were based on the geophone tests, torsional shear tests, and conventional triaxial tests.

The test sphere was modeled as a rigid sphere which cannot deform. The interface between the test sphere and the sand body was defined as frictionless.

4.3.1 Numerical Modeling of Boundary Effect Analysis

Boundary effects are an important issue that need to be addressed in the laboratory model tests. To investigate the influence of boundary effects, four numerical models were created with different boundary dimensions. The diameter of the sphere was 4 inches, which was the largest sphere used in the laboratory tests.

Table 4.6 Boundary dimensions for different models

Model #	Length (inches)	Width (inches)	Height (inches)
1	30	10.5	42
2	30	21	42
3	36	12	42
4	40	21	42
5	50	21	42
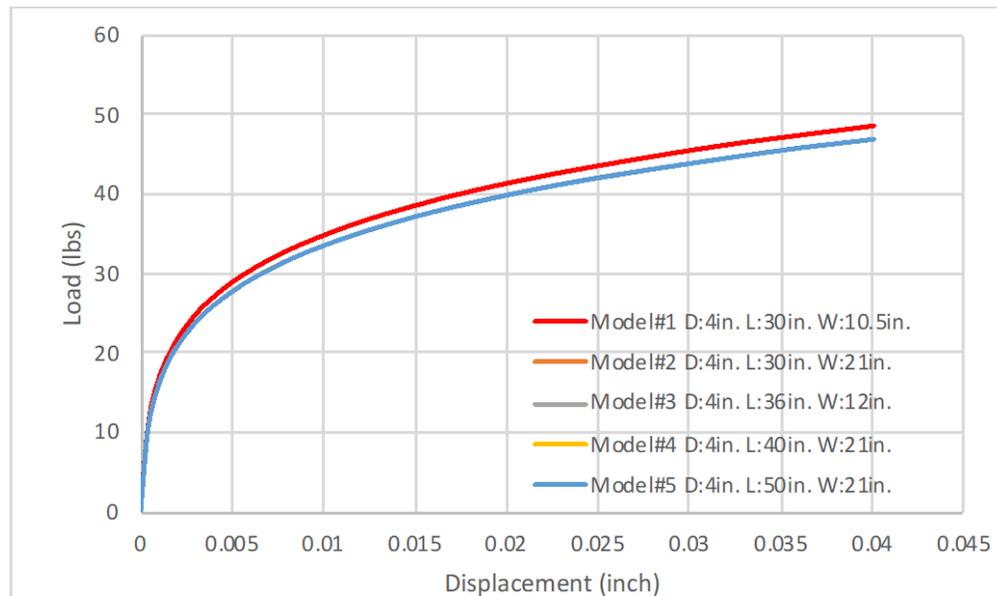
Figure 4.31 Comparison for the analysis of boundary effect

Figure 4.31 shows the comparison between the models with different boundary conditions. The dimension of Model 3 was accepted as the dimension in the numerical modeling of push tests. So, the boundary had little effect on the numerical modeling results.

4.3.2 Numerical Modeling of the Push Tests

The numerical modeling results were obtained by input the parameters describing G_{max} converted from shear wave velocity and the parameters describing the $G/G_{max} - \log\gamma$ relationship into the soil constitutive model. The parameters for the $G/G_{max} - \log\gamma$ relationship were the same for each test. The parameters for G_{max} varied depended on the measured shear velocity.

Table 4.7 shows the basic parameters of the soil for each test. The parameters controlling the shape of the $/G_{max} - \log\gamma$ curves were the same. The log-log slope n_G between the confining pressure and the maximum shear stiffness G_{max} was also same for each test. The maximum shear stiffness at one atmospheric pressure C_{G1} was calculated by the equation $G = \rho V_s^2$ depended on the measurement of the shear velocity. Table 4.8 shows C_{G1} calculated for different measure shear wave velocity at different embedment depths.

Table 4.7 Basic parameters of All-Purpose Sand

n_G	C_1 (%)	C_2	C_3	C_4	α_a	α_b	α_c
0.44	0.062	0.8	1.0	0.13	0.001	0	0.001

Table 4.8 C_{G1} of different shear wave velocities at different embedment depths

	320 fps at 10-in Embedment	340 fps at 10-in Embedment	365 fps at 20-in Embedment	395 fps at 20-in Embedment
C_{G1} (psi)	14224	15883	13612	15883

According to geophone testing, the measured shear wave velocity at the embedment depth of 10 inches was from 320 fps to 340 fps and the measured shear wave velocity at the embedment depth of 20 inches was from 365 fps and 395 fps. The Poisson's ratio was assumed to be 0.1 based on the measurement. The unit weight of the sand was 0.06 pci when the void ratio was 0.56.

Figures 4.32 to 4.34 show comparisons between the measured and predicted load-displacement curves for the varying sphere diameters at embedment depths of 10 inches and 20 inches. For all the spheres, the curves extracted from Abaqus overlay the load curves obtained from laboratory tests, which show they have good agreement between the numerical modeling and experimental results. The predicted load at the 0.25% diameter is proportional to the projection area of the sphere in the loading direction.
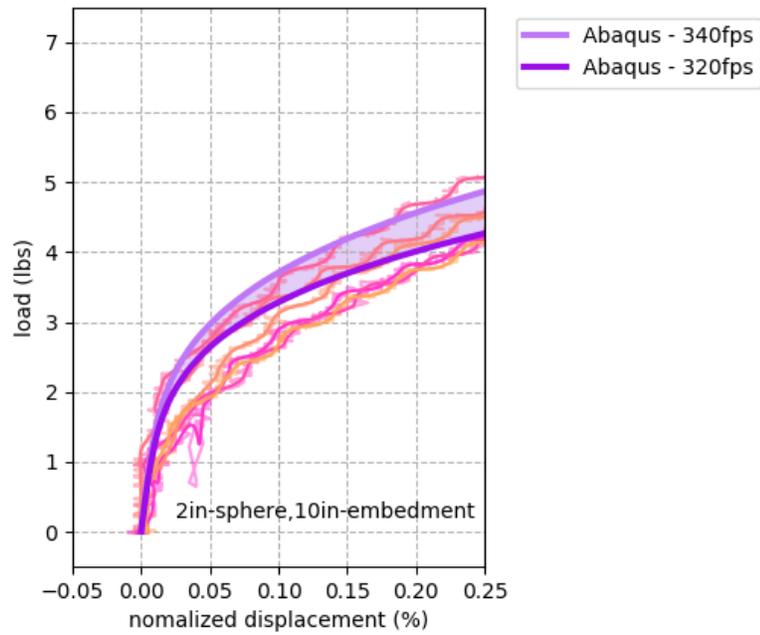
(a) 2in-Sphere, 10in-Emebedment
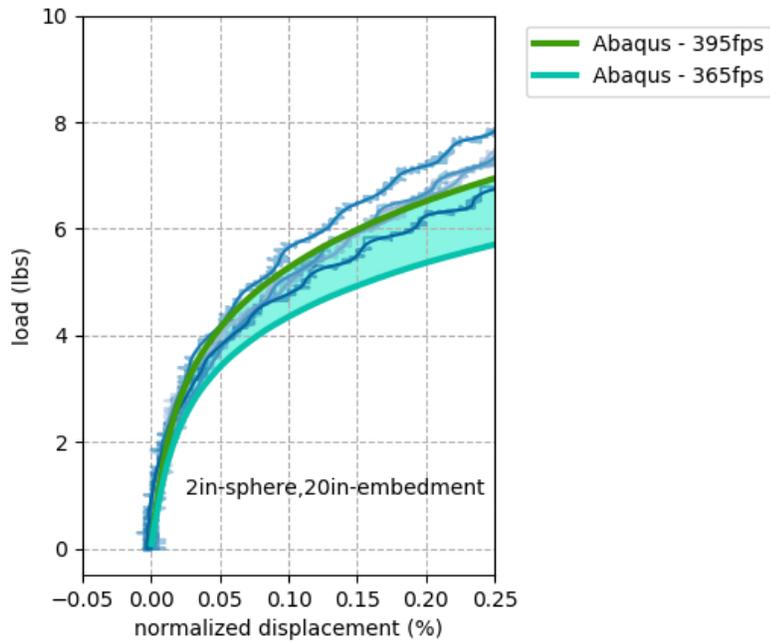
0

(b) 2in-Sphere, 20in-Embedment

Figure 4.32 Comparison between experimental and predicted load-displacement curves for 2-inch sphere
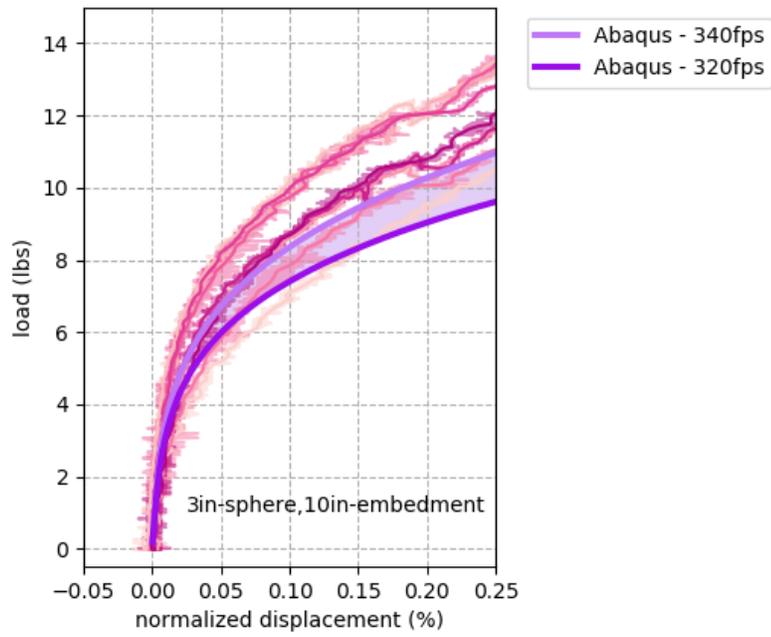
(a) 3in-Sphere, 10in-Embemdnet
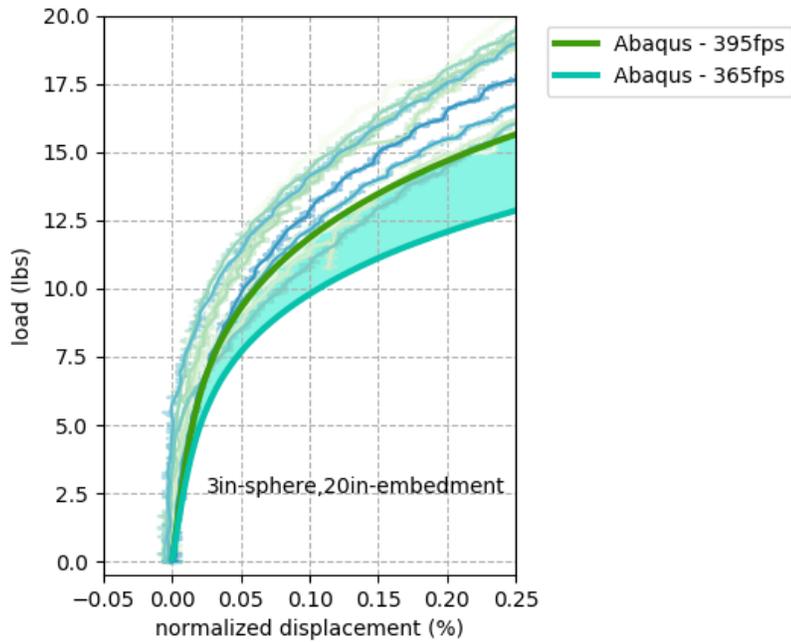
(b) 3in-Sphere, 20in-Embedment

Figure 4.33 Comparison between experimental and predicted load-displacement curves for 3-inch sphere
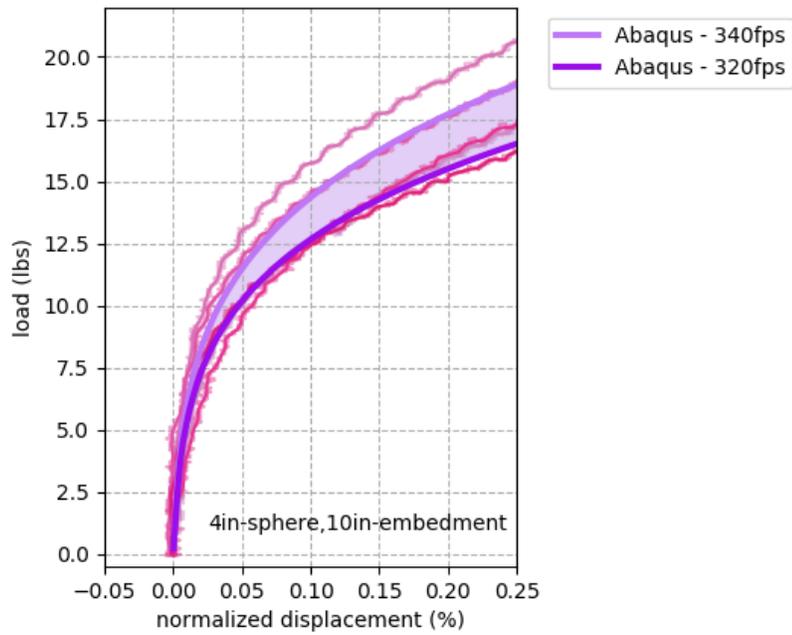
(a) 4in-Sphere, 10in-Embemdnet
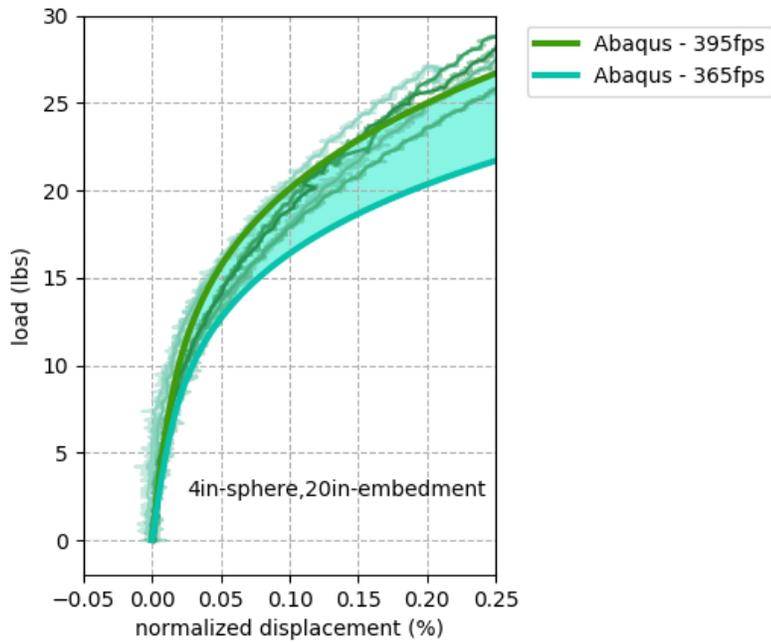
(b) 4in-Sphere, 20in-Embemdnet

Figure 4.34 Comparison between experimental and predicted load-displacement curves for 4-inch sphere

4.4 Laboratory Model Testing Conclusions

The major conclusions from the laboratory model tests are as follows:

1. The procedure developed for creating a sand bed is both repeatable and reliable when conducting both monotonic and cyclic push tests.
2. The initial relationship between lateral load and lateral displacement in the model tests is non-linear, even at very small displacements.
3. Small-strain stiffness and permanent displacement increase with increasing cycles of one-way loading, but the changes become asymptotically smaller as the number of cycles increase; from a practical perspective, the changes in stiffness and permanent displacement are negligible after about 1,000 cycles.
4. Numerical modeling using the FEM model developed in Task 3 with the measured properties of the sand used in the model tests produces results that agree well with the measurements in the laboratory model tests, including the stiffness under static loading and the change in stiffness with cyclic loading. Accumulated permanent displacement still needs to be addressed with the numerical FEM model.

5. Technical Workshop

A workshop was held in May 2018 at The University of Texas at Austin. The participants included the project team together with the technical advisors (Table 5.1).

Table 5.1: List of Participants in the Technical Workshop

Name	Company	Email
Robert Gilbert	UT	bob_gilbert@mail.utexas.edu
Kenneth Stokoe	UT	k.stokoe@mail.utexas.edu
Yunhan Huang	UT	yunhan_huang@utexas.edu
James Munson	UT	jamesmunson@utexas.edu
Jonas Bauer	UT	jonasbauer@utexas.edu
Reinhaneh Hosseini	UT	reihos@utexas.edu
Shin Tower Wang	Ensoft	stw@ensoftinc.com
Hossein Fadaifard	Ensoft	hf@ensoftinc.com
Hendrik Sturm	NGI	Hendrik.Sturm@ngi.no
Hendrik Versteele	Cathie-Associates	Hendrik.Versteele@cathie-associates.com
Aaron Bradshaw	University of Rhode Island	abrads@uri.edu
Don J. Degroot	UMass Amherst	degroot@ecs.umass.edu
Cedric VandenHaute	Parkwind	Cedric.VandenHaute@parkwind.eu
Byron Byrne (remotely)	University of Oxford	byron.byrne@eng.ox.ac.uk
Harvey Burd (remotely)	University of Oxford	harvey.burd@eng.ox.ac.uk

The workshop presented (1) the results in the database indicating that the initial stiffness using p-y curves under widely used design guidelines were generally under-predicted at small lateral displacements; (2) the background on resonant column and torsional shear tests conducted in the laboratory and previous projects regarding field seismic tests in offshore conditions; (3) the detailed development and implementation of a constitutive model used to model small-strain shear strains in sands; (4) the laboratory model tests developed to simulate small-strain behavior created by laterally-loaded monopiles; (5) the seismic tests conducted at Mustang Island; (6) the comparisons between the numerical modeling and the measurement of the field and laboratory; (7) the monitored data from Belwind offshore wind farm the comparison between the predicted and measured resonance frequencies; and (8) the related

research, results and design recommendations from the PISA project. Details of the presentations are included as Appendix L.

At the conclusion of the workshop, the participants had a free exchange of views and reached consensus on a number of key issues. The main topic of the workshop, both in the presentation and discussion, is the advantage of using the theory of soil dynamics at small shear strains to simulate the behavior of the soil in the small-strain less than 0.25%. There was general agreement among the participants that the proposed approach (using in-situ dynamic tests to determine the small-strain stiffness and using laboratory dynamic tests to measure the small-strain non-linearity of sand) in a 3-D finite element model showed promise. Furthermore, the workshop participants agreed on the following:

- The comparison of measured and designed values of resonance frequencies for wind turbines at Belwind illustrates that the resonance frequencies have been generally been underestimated by designers.
- The measured resonance frequencies of in-service offshore wind turbines tend to increase with time. The increase in second order resonance frequency is more obvious than the first order resonance frequency.
- The conventional LPILE model with sand p-y curves underestimates the pile stiffness and cannot capture the high non-linearity in the range of the small lateral displacement.

Furthermore, the workshop provided the opportunity of discussing the possibility of future cooperation with the participants in the PISA project.

6. Design Guidelines

The results from this research lead to three recommendations for the design of laterally loaded piles in sand:

1. The p-y curves used in current design practice do not predict well the stiffness and the non-linearity of laterally loaded piles at the small lateral displacements relevant for offshore wind turbine monopiles in service.
2. In order to better predict the stiffness and non-linearity of laterally loaded piles at small lateral displacements, there is a need to either measure directly or empirically establish for the sand the in situ maximum ("small-strain") shear modulus, the relationship between shear modulus and shear strain, the relationship between shear modulus and effective confining pressure, and the effect of cyclic loading on the shear modulus.
3. Improved p-y curves to be used in design can be derived directly from 3-D FEM analyses using representative properties of the sand in situ at small strains or indirectly from simplified models relating the shapes of the p-y curves to the properties of the sand.

6.1 Do Not Use Standard p-y Curves for Design of Monopiles in Service

The p-y curves used in current design practice do not predict well the stiffness and the non-linearity of laterally loaded piles at the small lateral displacements relevant for offshore wind turbine monopiles in service. This conclusion is supported by the data base of lateral load tests for piles in sand, the monitoring data from the offshore wind turbines in service, the laboratory model tests conducted in this research, and the numerical analyses using realistic properties for sands. The potential difference in the initial stiffness between the design predictions and reality, which is simplistically the measure that most affects design of the tower and the turbine for service loading conditions due to its influence and resonance and fatigue, is more than a factor of five and could be as much as an order of magnitude. In addition, the difference will depend on the specific properties of the sand.

Since it is unreasonable to simply factor the initial portion of p-y curves by a factor of five or more (for context, the difference of the initial stiffness of the p-y curve for sands ranging from very loose to very dense is about a factor of ten), we recommend that the existing p-y curves not be used to design offshore wind turbine monopiles in service loading conditions.

6.2 Measure Properties of Sand at Small Strains

In order to better predict the stiffness and non-linearity of laterally loaded piles at small lateral displacements, there is a need to either measure directly or empirically establish for the sand the in situ maximum ("small-strain") shear modulus, the relationship between shear modulus and shear strain, the relationship between shear modulus and effective confining pressure, and the effect of cyclic loading on the shear modulus.

In Situ G_{max}

The maximum value of the shear modulus at very small strains, G_{max}, is measured in situ by propagating shear (S) waves through the soil. Two commonly used approaches on land are the downhole and crosshole seismic methods. In the downhole method, the shear-wave source is located on the ground surface and the sensing element (a three-dimensional (3D) geophone) is lower down the borehole. Source-to-receiver measurements are performed at multiple depths to develop a shear wave velocity (Vs) versus depth profile. (This configuration is also used offshore in terms of a seismic cone penetration test, known as seismic CPT.) The crosshole method involves 2 or 3 cased boreholes, with the shear-wave source in one borehole and 3D receivers located at the same depth in the other boreholes. Again, measurements are performed at multiple depths to develop a Vs versus depth profile.

For offshore measurements, the seismic CPT described above is used to determine Vs depth profiles. However, a logging tool, known as the P/S suspension logger (P = compression waves and S = shear waves) is also used in a single borehole. A third method that can be used offshore is the Spectral-Analysis-of-Surface-Waves (SASW) method. In this method, the source is placed on the sea floor and the receivers are also located on the sea floor at different distances away from the source (Luke and Stokoe, 1998). In the SASW method, surface interface waves, known as Scholte waves at a water–solid interface, are generated with vertically oriented shaking at the source. The resulting vertical surface motions are measured at various distances away from the source. The goal of the SASW test is to determine the phase difference between pairs of receivers over a wide range in frequencies (Joh, 1996). Figure 6.1 shows a typical field testing arrangement for the source and one pair of receivers. Due to the cost of drilling boreholes offshore and the large areas associated with wind farms, SASW testing is an efficient way of directly measuring G_{max} versus depth in the soil (Lee et al., 1997).
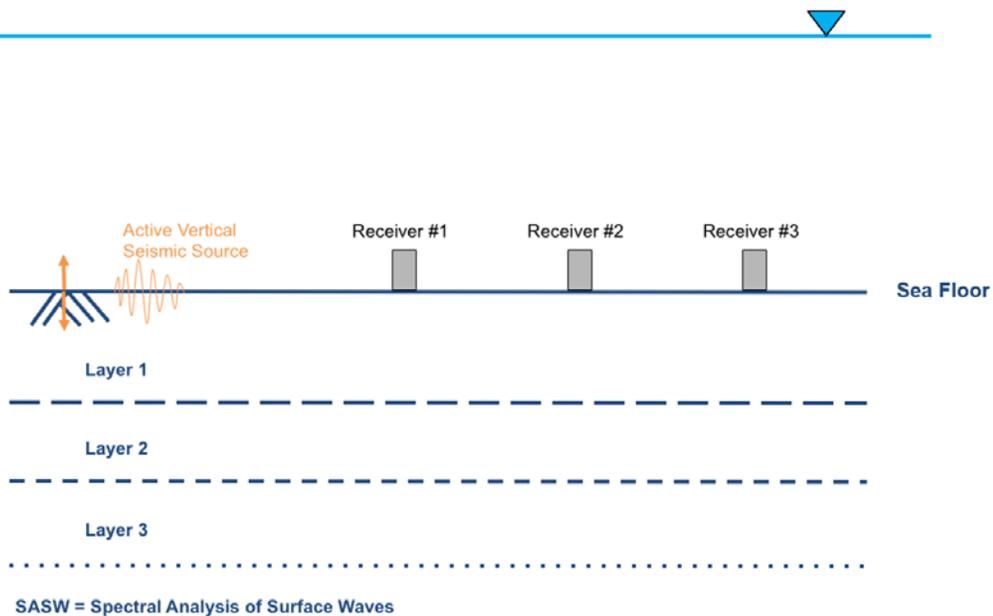
Figure 6.1 Typical field testing arrangement for the source and one pair of receivers used in SASW testing offshore

There are empirical equations relating G_{max} to cone penetration resistance; however, there is significant variability in the results since cone penetration resistance is a destructive method that imposes very large shear strains on the soil. There also empirical relations relating G_{max} to the density and distribution of grain sizes (see Section 3.1.1). While there is also significant variability in these empirical equations, they do provide a reasonable preliminary estimate of G_{max}. In addition, an empirical approach such as this will be the best way to estimate the small-strain properties of scour protection material, which cannot be measured in situ during design since it has not yet been placed.

Relationships between G and γ, G and σ' and G and N_{cycle}

The non-linearity of the soil stiffness (G) with shear strain (γ) is important to predict the non-linearity of a laterally loaded monopile at small displacements. This relationship is best measured in the laboratory using resonant column and torsional shear tests on either "undisturbed" samples from the field (generally not possible with sands) or reconstituted samples with similar void ratios as those in the field. In addition, triaxial tests are needed to extend the non-linearity at small strains to larger strains in order to capture the entire p-y curve.

The relationship between soil stiffness and effective confining stress is (σ') is important (1) to improve the resolution of in situ measurements of shear stiffness (usually done over relative large intervals of depth) and (2) to model how the soil properties change as the pile is displaced into the soil. This relationship is best measured in the laboratory by performing resonant column and torsional shear tests over a range of confining stresses.

The relationship between soil stiffness and number of cycles of loading is important to predict how cycles of loading will affect the stiffness and permanent lateral displacements. This information can be extracted from the torsional shear test results versus the number of cycles of shear.

There are empirical equations to estimate the relationships between G and γ and G and σ' as a function of void ratio and grain size. We are not aware of any empirical relationships at present relating G and N_{cycle}.

6.3 Revise p-y Curves with Small-Strain Properties of Sand

The p-y curves used for design of offshore monopiles in service loading conditions should be revised based on the small-strain properties of the site-specific soils (sands). Even if a project-specific 3-D FEM analysis is conducted, there is still a need to reduce the results into the form of p-y curves for the non-linear, dynamic models used to design the tower and turbine. There are three approaches to revise the p-y curves:

1. Establish p-y curves directly from a project-specific 3-D FEM analysis using a constitutive model of the sand that captures its small-strain properties.
2. Estimate p-y curves indirectly from the small-strain properties of the sand using a simplified parametric model that approximates the results of a 3-D FEM analysis based on the input to the FEM analysis.
3. Adjust the initial portion of the API p-y curves used in current practice approximately based on the shear stiffness of the sand at very small strains.

6.3.1 Establish p-y Curves Directly from Project-Specific 3-D FEM Analysis

The most rigorous approach to incorporate the small-strain properties of the sand into the model for the pile response is to conduct a 3-D FEM analysis using a constitutive model that captures the small-strain properties of the sand (e.g., Section 3.4). The p-y curves can be calculated directly by modeling the monopile as a rigid body with the same lateral displacement imposed at the top and bottom, i.e., it only translates horizontally into the soil (Figure 6.2). At each depth, the unit lateral load, p (lbs/in), in the p-y curve is computed as the sum of the projected contact force in the displacement direction along the contact surface of the pile and the displacement, y $(in.)$, is the imposed lateral displacement (Figure 6.3).

As an example, the p-y curves from the FEM analysis of the Mustang Island pile are shown in Figure 6.4. The result of inputting these p-y curves into a conventional p-y analysis (say with LPILE) is essentially identical to the FEM results (Figure 6.5).
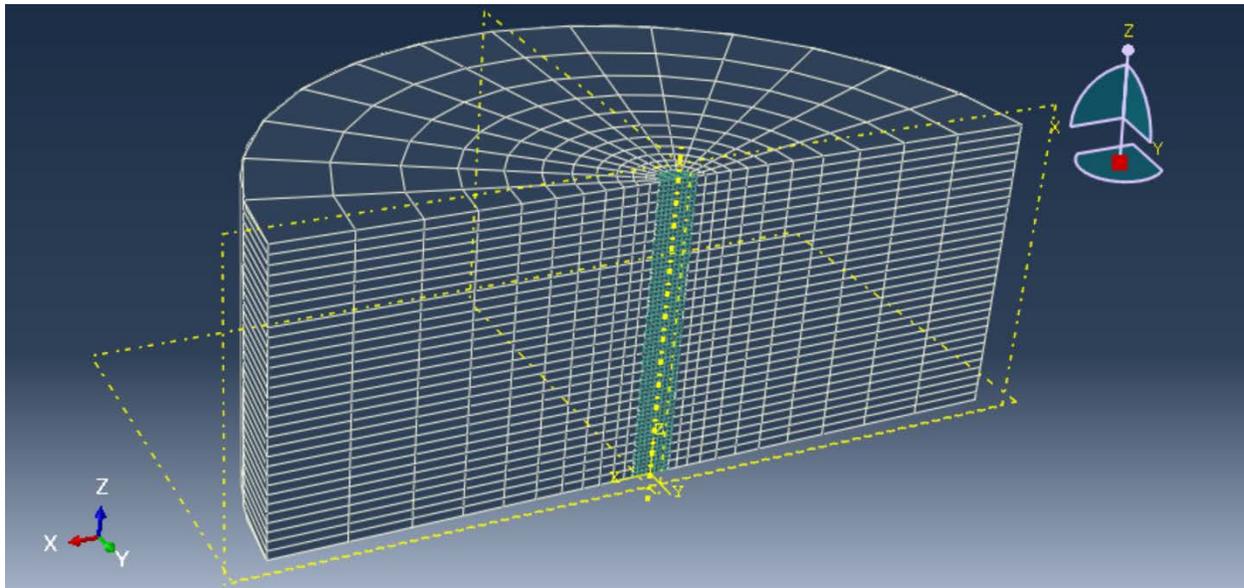
Figure 6.2 Pile model for parametric study on p-y curves
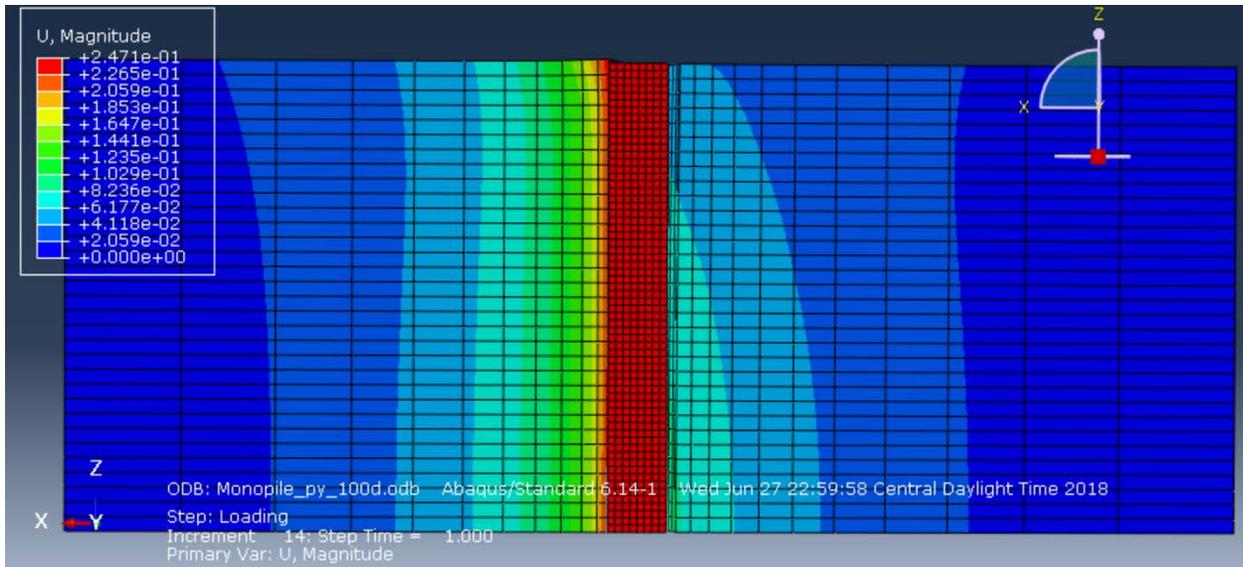
Figure 6.3 Displacement contour of the perfect rigid pile (Deformation Scale Factor:100)
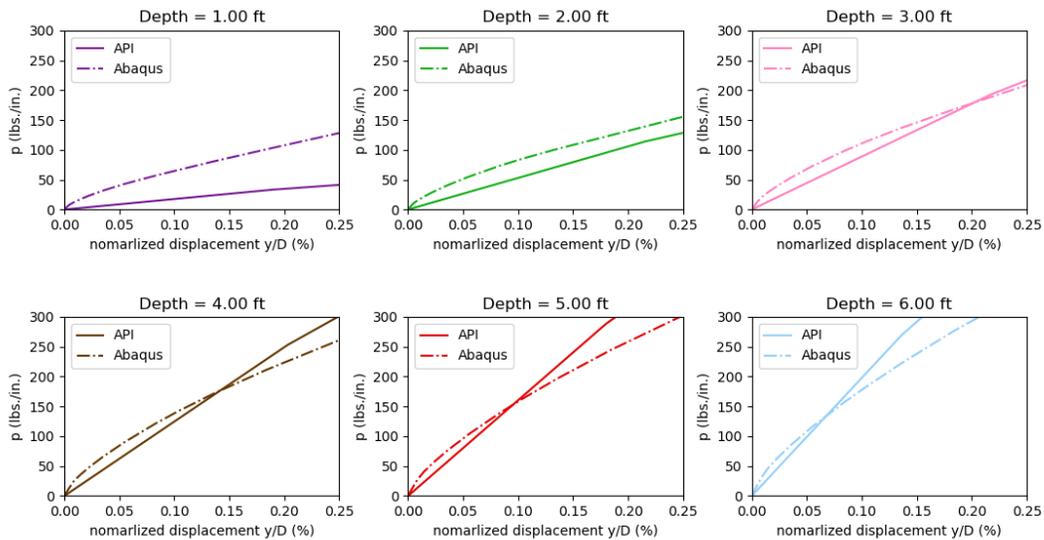
Figure 6.4 Comparison of the p-y curves between the proposed method and traditional method at small displacements for Mustang Island load test
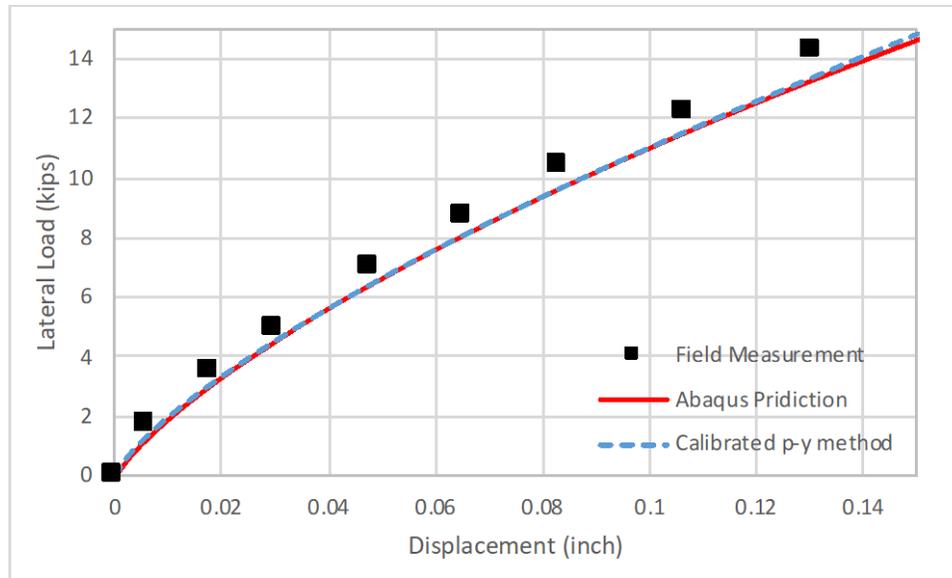
Figure 6.5 Comparison between the load versus displacement curves predicted by the proposed p-y method and 3-D finite element model on Mustang Island Test

One potential source of complexity in this approach is the effect of side shear on the walls of the pile, which will restrain rotation, and the effect of shear and rotational resistance at the tip of the pile. If the pile does not rotate significantly because the pile is either (i) long and slender or (ii) the lateral displacement at the pile head is small, then these additional effects are negligible. For example, these effects are not noticeable in comparing the FEM results (which account for all of the soil resistance) with the p-y results (which only account for the lateral soil resistance along the pile length) in Figure 6.5. As a further check of the importance of this additional resistance for a shorter pile, two similar comparisons were performed for a monopile with a diameter of 195 inches and a length to diameter (L/D) ratio of 4. At lateral displacements similar to the service loading displacements for Belwind (0.05% of the pile diameter), the additional effects of side shear and tip resistance are very small (Figure 6.6); even at lateral displacements up to 0.25% of the pile diameter, the contribution of the effects of side shear and tip resistance are only about 10 percent (Figure 6.6). To be more rigorous, these effects can be directly incorporated into a p-y type of an analysis by introducing additional rotational springs along the pile length and lateral and rotational springs at the tip. The stiffness for these springs can be extracted from a 3-D finite element analysis of the monopile under imposed lateral loads and moments at the pile head in a similar way that the p-y curves are extracted. The proposed design approach resulting from the PISA project includes incorporating these additional springs (e.g., Byrne et al. 2017).
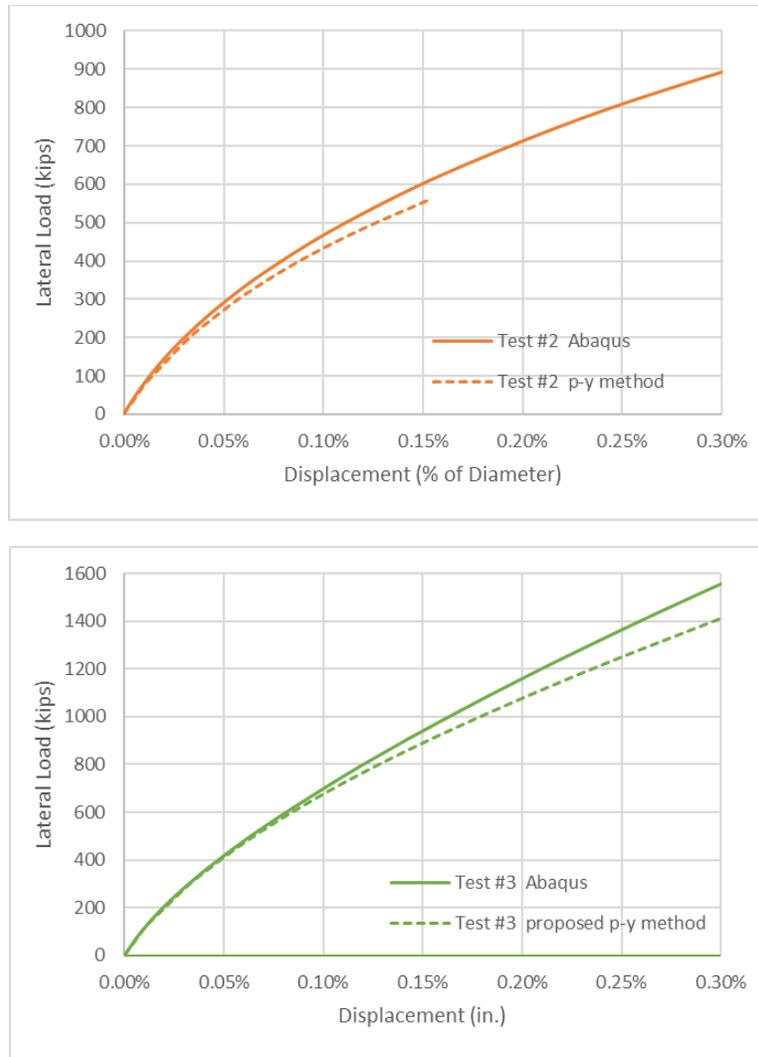
Figure 6.6 Comparison between the load versus displacement curves predicted by the proposed p-y method and 3-D finite element model on Monopile with L/D = 4 (see Section 6.3.2 for a description of the soil properties for Test #2 and Test #3)

6.3.2 Estimate p-y Curves Indirectly from Simplified Parametric Model

A less rigorous approach to incorporate the small-strain properties of the sand into the model for the pile response is to estimate the shape of the p-y curves based on a simplified model that has been calibrated from parametric studies with 3-D FEM analyses.

In order to explore the potential of this simplified approach, a preliminary parametric study has been used to calibrate a simplified model to estimate p-y curves from the following eight input parameters to a rigorous 3-D FEM analysis: (1) pile diameter, d; (2) effective vertical stress versus depth, σ'_v; (3) C_{G1} and n_G describing the maximum shear stiffness, G_{max}; and (4) C_1, C_2, C_3, and C_4 describing the $G/G_{max} - \log \gamma$ curves.

A series of 3-D finite element models was established to study the influence of the eight parameters on the shape and the magnitude of the proposed p-y curves. Figure 6.2 shows the 3-D finite element model of the pile with a diameter of 96-inch. Half models of piles were analyzed in the finite element software, Abaqus, with diameters of 24-inch, 48-inch, 96-inch, 144-inch, and 196-inch. The heights of the piles and the soil in all the models were 768-inch. Horizontally, the soil extended 10 diameters from the edge of the pile. The models of the piles with different diameters were used to analyze the influence of the pile diameter. The model of the pile with 96-inch diameter was used to analyze the influence of the other seven parameters.

The properties of the sand for the parametric analyses are summarized in Table 6.1. The submerged unit weight was assumed equal to 0.03-pci and Poisson' ratio assumed equal to 0.3 for the sand.

The piles were modeled as perfect rigid body. The soil-pile interface was frictionless. Same displacement was applied at the top and the bottom planes of the pile to make the pile move horizontally as a rigid body (Figure 6.2). The displacement was set to be 0.25% of the diameter of the pile. The p-y curves were extracted directly from the FEM results (Figure 6.3).

Table 6.1 Numerical models for parametric study

Test #	D (in.)	C_G1 (psi)	n_G	C1	C2	C3	C4
1	24	15069	0.45	0.1	0.5	0.85	0.05
2	48	15069	0.45	0.1	0.5	0.85	0.05
3	96	15069	0.45	0.1	0.5	0.85	0.05
4	144	15069	0.45	0.1	0.5	0.85	0.05
5	192	15069	0.45	0.1	0.5	0.85	0.05
6	96	7534.5	0.45	0.1	0.5	0.85	0.05
7	96	11301.75	0.45	0.1	0.5	0.85	0.05
8	96	15069	0.45	0.1	0.5	0.85	0.05
9	96	22603.5	0.45	0.1	0.5	0.85	0.05
10	96	30138	0.45	0.1	0.5	0.85	0.05
11	96	15069	0.5	0.1	0.5	0.85	0.05
12	96	15069	0.45	0.1	0.5	0.85	0.05
13	96	15069	0.4	0.1	0.5	0.85	0.05
14	96	15069	0.35	0.1	0.5	0.85	0.05
15	96	15069	0.3	0.1	0.5	0.85	0.05
16	96	15069	0.45	0.05	0.5	0.85	0.05
17	96	15069	0.45	0.075	0.5	0.85	0.05
18	96	15069	0.45	0.1	0.5	0.85	0.05
19	96	15069	0.45	0.125	0.5	0.85	0.05
20	96	15069	0.45	0.15	0.5	0.85	0.05
21	96	15069	0.45	0.1	0.4	0.85	0.05
22	96	15069	0.45	0.1	0.5	0.85	0.05
23	96	15069	0.45	0.1	0.6	0.85	0.05
24	96	15069	0.45	0.1	0.7	0.85	0.05
25	96	15069	0.45	0.1	0.8	0.85	0.05
26	96	15069	0.45	0.1	0.5	0.6	0.05
27	96	15069	0.45	0.1	0.5	0.7	0.05
28	96	15069	0.45	0.1	0.5	0.85	0.05
29	96	15069	0.45	0.1	0.5	1	0.05
30	96	15069	0.45	0.1	0.5	1.1	0.05
31	96	15069	0.45	0.1	0.5	0.85	0
32	96	15069	0.45	0.1	0.5	0.85	0.02
33	96	15069	0.45	0.1	0.5	0.85	0.04
34	96	15069	0.45	0.1	0.5	0.85	0.06
35	96	15069	0.45	0.1	0.5	0.85	0.08
36	96	15069	0.45	0.05	0.5	0.6	0.05
37	96	15069	0.45	0.075	0.5	0.6	0.05
38	96	15069	0.45	0.1	0.5	0.6	0.05
39	96	15069	0.45	0.125	0.5	0.6	0.05
40	96	15069	0.45	0.15	0.5	0.6	0.05
41	96	15069	0.45	0.05	0.5	1.1	0.05
42	96	15069	0.45	0.075	0.5	1.1	0.05
43	96	15069	0.45	0.1	0.5	1.1	0.05
44	96	15069	0.45	0.125	0.5	1.1	0.05
45	96	15069	0.45	0.15	0.5	1.1	0.05
46	96	15069	0.45	0.1	0.4	0.6	0.05
47	96	15069	0.45	0.1	0.5	0.6	0.05

Test #	D (in.)	C_G1 (psi)	n_G	C1	C2	C3	C4
48	96	15069	0.45	0.1	0.6	0.6	0.05
49	96	15069	0.45	0.1	0.7	0.6	0.05
50	96	15069	0.45	0.1	0.8	0.6	0.05
51	96	15069	0.45	0.1	0.4	1.1	0.05
52	96	15069	0.45	0.1	0.5	1.1	0.05
53	96	15069	0.45	0.1	0.6	1.1	0.05
54	96	15069	0.45	0.1	0.7	1.1	0.05
55	96	15069	0.45	0.1	0.8	1.1	0.05
56	96	7534.5	0.3	0.1	0.5	0.85	0.05
57	96	11301.75	0.3	0.1	0.5	0.85	0.05
58	96	15069	0.3	0.1	0.5	0.85	0.05
59	96	22603.5	0.3	0.1	0.5	0.85	0.05
60	96	30138	0.3	0.1	0.5	0.85	0.05
61	96	7534.5	0.375	0.1	0.5	0.85	0.05
62	96	11301.75	0.375	0.1	0.5	0.85	0.05
63	96	15069	0.375	0.1	0.5	0.85	0.05
64	96	22603.5	0.375	0.1	0.5	0.85	0.05
65	96	30138	0.375	0.1	0.5	0.85	0.05

To parametrize the p-y curves, the lateral displacement was normalized by the diameter of the pile and the load was normalized by the load at 0.25% diameter displacement, $p_{0.25\%}$. The shape of the normalized p-y curves was approximated using the following expression:

$$\frac{p}{p_{0.25\%}} = (1-n) \times (\frac{400 \times y}{d}) + n \times (1 - (\frac{400 \times y}{d} - 1)^2)^{0.5} \tag{6.1}$$

where, $\frac{p}{p_{0.25\%}}$ is the normalized load, $\frac{y}{d}$ is the normalized displacement, and n is a parameter controlling the shape of the expression (Figure 6.7).
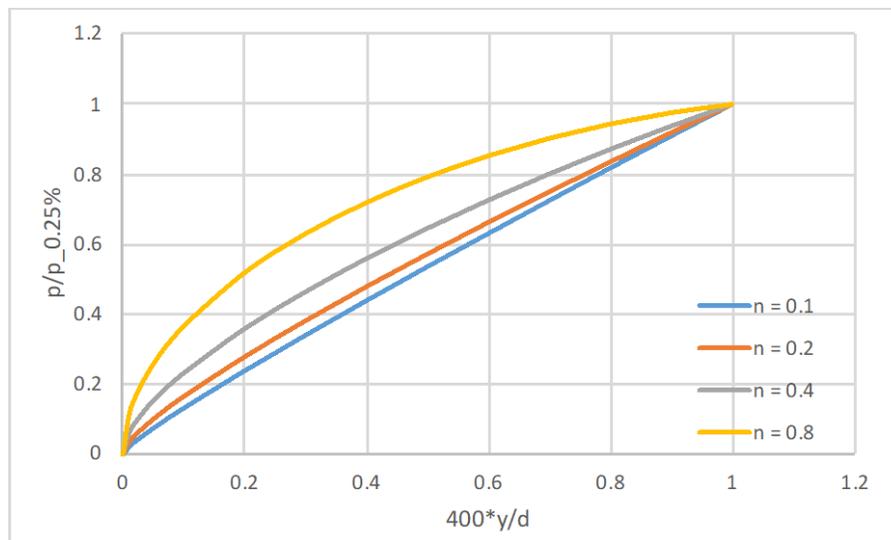
Figure 6.7 Proposed normalized p-y curve

115

Laboratory Testing of Lateral Load Response for Monopiles in Sand

The study on the parameter n shows that only four parameters, C_{G1} (psi), C_1 (%), C_2, and C_3 have significant influence on the shape of the normalized p-y curve. The relationship between n and the four parameters is approximated as:

$$n = 0.4 + x_{CG1} \times (C_{CG1} - 15069) + x_{C1} \times (C_1 - 0.1) + x_{C2} \times (C_2 - 0.5) + \frac{x_{C3}}{C_3 - y_{C3}} + z_{C3} \quad (6.2)$$

where,

x_{CG1}	x_{C1}	x_{C2}	x_{C3}	y_{C3}	z_{C3}
-2.75E-5	-5.42	1.28	-0.45	1.48	-0.71

The study on the parameter $p_{0.25\%}$ (lbs/in) shows that all the eight parameters have a significant influence on the magnitude of the load at the 0.25% diameter displacement. The relationship between $p_{0.25\%}$ and the eight parameters is approximated as:

$$p_{0.25\%} = 666 \times A_d \times \left[B_{CG1} \times \left(\frac{C_{G1}}{15069} \right)^{D_{CG1}} \right] \times \left(E_{C1} \times C_1^{F_{C1}} \right) \times \left(G_{C2} \times C_2^{H_{C2}} \right) \times I_{C4} \times J_\sigma / K_{C3} \quad (6.3)$$

where,

$$A_d = -a_d * d^2 + b_d * d + c_d$$

$$B_{CG1} = a_{CG1} * n_g^2 - b_{CG1} * n_g + c_{CG1}$$

$$D_{CG1} = d_{CG1} * n_g^2 - e_{CG1} * n_g + f_{CG1}$$

$$E_{C1} = a_{C1} * C_3 - b_{C1}$$

$$F_{C1} = c_{C1} * C_3 - d_{C1}$$

$$G_{C2} = a_{C2} * \exp(-b_{C2} * C_3)$$

$$H_{C2} = -c_{C2} * C_3 + d_{C2}$$

$$I_{C4} = a_{C4} * C_4 + b_{C4}$$

$$J_\sigma = a_s * \sigma_v' + b_s$$

$$K_{C3} = -a_{C3} * C_3 + b_{C3}$$

a_d	b_d	c_d	a_{CG1}	b_{CG1}	c_{CG1}
0.105	1.1	0.023	16.7	16.4	5.12
d_{CG1}	e_{CG1}	f_{CG1}	a_{C1}	b_{C1}	c_{C1}
3.21	1.40	1.56	13.02	3.79	1.45
d_{C1}	a_{C2}	b_{C2}	c_{C2}	d_{C2}	a_{C4}
0.39	5.27	3.17	2.34	0.661	1.34
b_{C4}	a_s	b_s	a_{C3}	b_{C3}	
0.93	0.61	0.33	1.38	2.14	

The model proposed here for the p-y curve up a lateral displacement of 0.25% the diameter of the pile is merged with the API p-y curve for larger displacements. In some cases, the model proposed here needs to be extrapolated to larger displacements in order to intersect the API curve; in those cases, the model is extrapolated with a line that is tangent to the end of the curve (Figure 6.8) until it intersects the API curve.
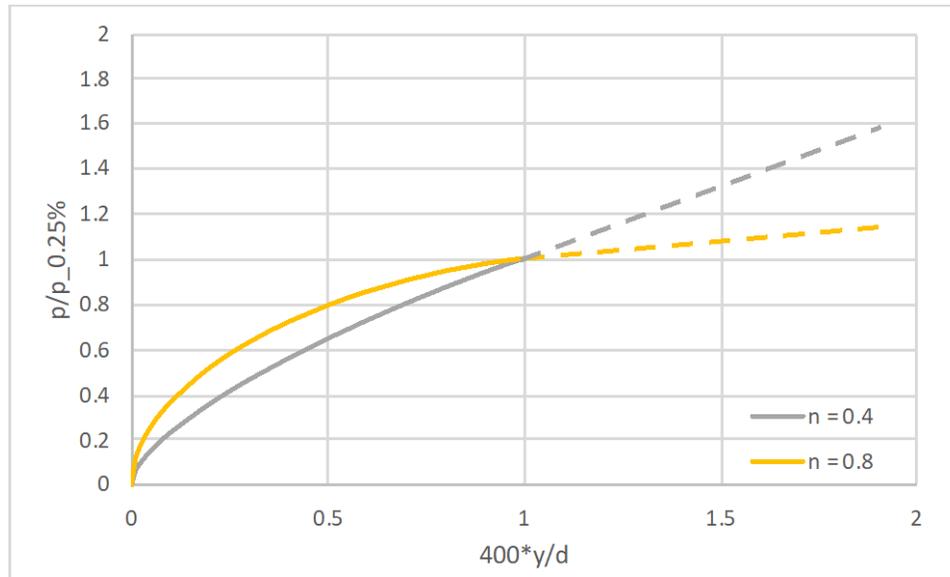
Figure 6.8 Extending the proposed p-y curve out of the range of 0.25% diameter

As one test of the proposed approach, Figure 6.9 shows the result of this approach applied to the Mustang Island test in comparison with the FEM results. In this case, the two results match very well since the Mustang Island sand was used as the based case in the parametric study.
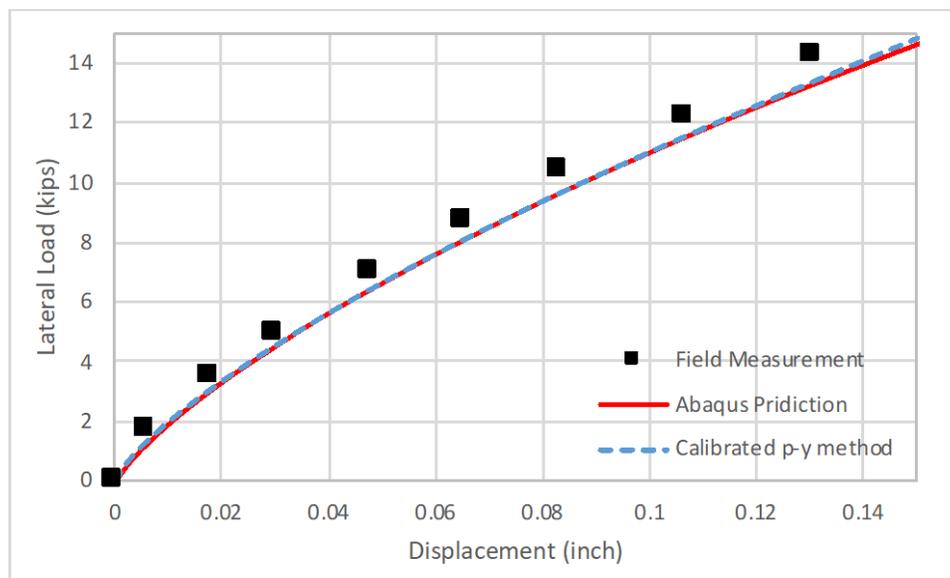
Figure 6.9 Comparison between the load versus displacement curves predicted by the proposed p-y method and 3-D finite element model on Mustang Island Test

As another test of the proposed approach, a monopile was analyzed with a diameter of 195 inches, a wall thickness of 2.36 inches, and a length of 780 inches giving L/D = 4 (Figure 6.2); this pile is similar to the Belwind monopiles. Table 6.2 lists three different sets of parameters ("tests") characterizing the small-strain soil properties for this study.

Table 6.2 Parameters of soil used to study proposed parametric model

	C_{G1} (psi)	n_g	C_1 (%)	C_2	C_3	C_4
Test 1	15069	0.45	0.1	0.5	0.85	0.05
Test 2	11648	0.4	0.05	0.4	0.8	0.01
Test 3	21102	0.43	0.06	0.6	0.75	0.08

The lateral load versus displacement curves calculated by Abaqus are compared to the curves derived from proposed p-y curves in Figures 6.10 to 6.12. All the three tests show reasonably good agreement between the two procedures. This proposed simplified parametric model is preliminary and could be improved by providing better expressions to describe the magnitude and shape of the p-y curves, incorporating Poisson's ratio directly into the parameters by using confining stress rather than vertical effective stress as a parameter, by possibly non-dimensionalizing all of the parameters, and by conducting more extensive parametric studies to capture a wider range of possible input parameters.
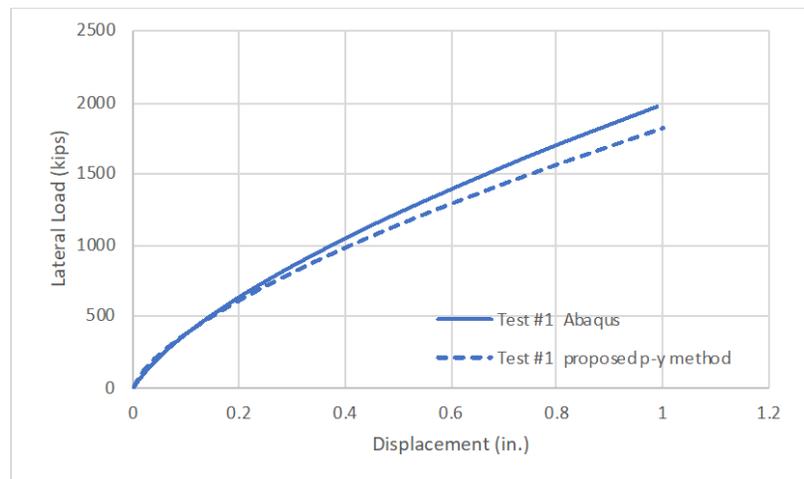
Figure 6.10 Load versus displacement curve from Abaqus model compared with proposed p-y method (Test 1)
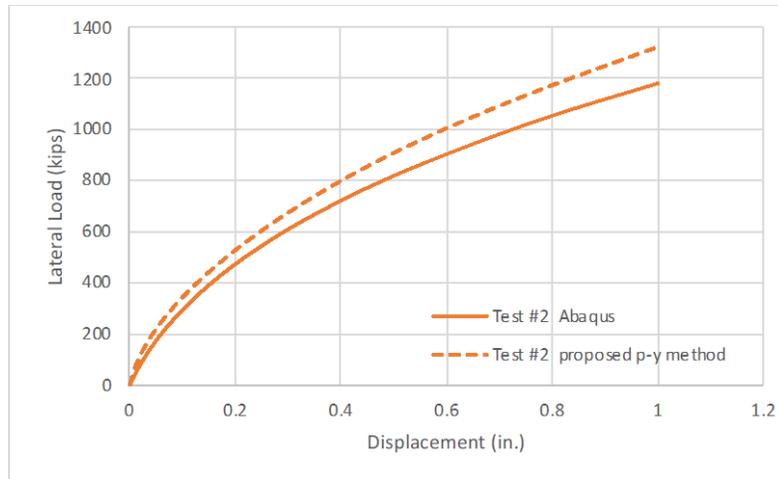
Figure 6.11 Load versus displacement curve from Abaqus model compared with proposed p-y method (Test 2)
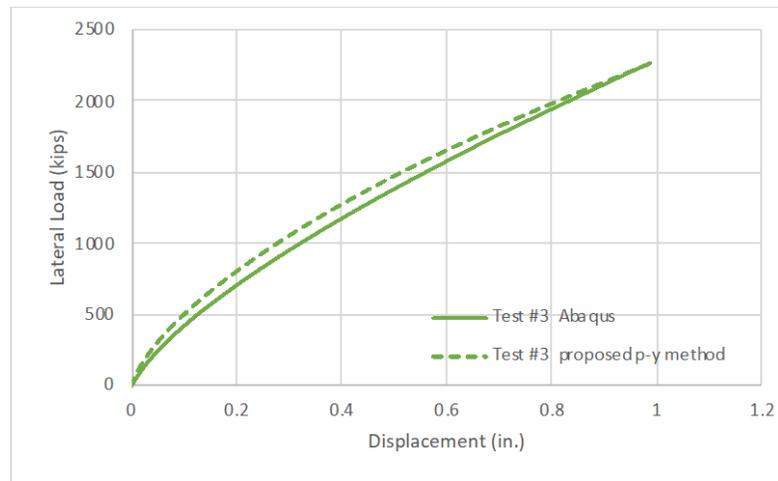
Figure 6.12 Load versus displacement curve from Abaqus model compared with proposed p-y method (Test 3)

This type of a simplified parametric approach is included in the design recommendations resulting from the PISA project (e.g., Byrne et al. 2017). However, the current PISA approach does not capture the non-linearity of the pile response at small lateral displacements because it has fewer parameters than we are proposing.

6.3.3 Adjust Initial Portion of API p-y Curves

The simplest and most practical approach to incorporate the small-strain properties of the sand into the model for the pile response would be to adjust the initial portion of the API p-y curves as a function of the maximum shear stiffness, G_{max}. There is unfortunately no explicit, theoretical relationship between the initial slope of a p-y curve and G_{max} because the stiffness changes with confining stress (which increases as the pile is loaded) and because of the three-dimensional complexity caused by the free-surface

boundary at the top of the soil. Subsequently, an approach like this would need to be empirical calibrated with field test results or approximated using numerical 3D FEM analyses as the "true" solution. Even then, this approach will not capture the non-linearity of the p-y curves measured in field tests and estimated from FEM results. We will use the numerical parametric results from Section 6.3.2 to explore the viability of this approach further.

7. Conclusions and Future Work

The following major conclusions are drawn from this research:

1) The analysis of existing results from field lateral load tests conducted on piles in sand shows the following:
   a. In all of the field lateral load tests with enough resolution to discern the initial relationship between load and displacement of the pile head, the relationship is not linear and is, therefore, not easily captured by assuming an elastic subgrade modulus as is done in the current design practice.
   b. In general, the p-y curves from the current design practice underestimate the initial stiffness for field lateral load tests of piles in sand, both for monotonic and cyclic tests.
2) The comparison of measured and designed values of resonance frequencies for offshore wind turbines at Belwind and Northwind illustrates the following:
   a. The resonance frequencies have been under-predicted in design. In addition, the measured resonance frequencies of these wind turbines increase with time; the increase in second mode resonance frequency is more significant than the increase in first mode resonance frequency.
   b. The calculated resonance frequencies of wind turbines increase with the assumed stiffness of the sand. The results of this study demonstrate that the resonance frequency predictions are sensitive to an accurate evaluation of the pile-soil stiffness and that the subgrade modulus (k) value used in design needs to be increased by more than five times to match the field observations. Increasing the stiffness of the sand has a larger influence on the second mode resonance frequency than on the first mode resonance frequency.
   c. The predicted lateral displacement at the pile head for the Belweind and Nothwind monopiles under service loading (using the calibrated model to match field measurements) is less than 0.05% of the pile diameter.
3) The results of laboratory model tests with cyclic lateral loads applied to a sphere embedded in sand, which provides a state of stress and strain around the sphere that is similar to those around a laterally loaded piles, show the following:
   a. The initial relationship between lateral load and lateral displacement in the model tests is non-linear, even at very small displacements.
   b. Small-strain stiffness and permanent displacement increase with increasing cycles of one-way loading, but the changes become asymptotically smaller as the number of cycles increase; from a practical perspective, the changes in stiffness and permanent displacement are negligible after about 1,000 cycles.
4) A 3-D FEM model that incorporates a constitutive model to characterize the small-strain properties of sand, including the maximum shear stiffness at very small strains and the relationships between shear stiffness and shear strain and shear stiffness and effective confining stress, is capable of the following:
   a. It is able to predict the results of laboratory element tests in static and cyclic loading (e.g., torsional shear and dynamic triaxial tests).
   b. In the analysis of the Mustang Island lateral load field tests, the predicted response of the pile, which is based on constitutive parameters based on the field measurements of shear

velocity and resonant column and torsional shear tests on laboratory specimens, matches well with the measured results. The conventional p-y method underestimates the pile stiffness in the range of the small displacement and does not predict the non-linearity of the response.

c. In the analyses of laboratory model tests conducted in this research, it produces results that agree well with the measurements in the laboratory model tests, including the stiffness under static loading and the change in stiffness with cyclic loading. Accumulated permanent displacement still needs to be addressed with the numerical FEM model.

These conclusions lead to the following recommendations for design of laterally loaded monopiles in sand:

1) Exercise caution in using conventional p-y curves for sand to predict the performance of offshore wind turbine monopiles in service. The p-y curves used in current design practice do not predict well the stiffness and the non-linearity of laterally loaded piles at the small lateral displacements relevant for offshore wind turbine monopiles in service.

2) Measure directly or empirically establish for sand the in situ maximum ("small-strain") shear modulus, the relationship between shear modulus and shear strain, the relationship between shear modulus and effective confining pressure, and the effect of cyclic loading on the shear modulus. These small-strain properties are needed in order to predict the stiffness and non-linearity of laterally loaded piles at small lateral displacements.

3) Establish improved p-y curves to be used in design directly from 3-D FEM analyses using representative properties of the sand in situ at small strains. It may also be possible with future research to establish these curves from simplified models relating the shapes of the p-y curves to the small-strain properties of the sand.

Future work is recommended in the following areas to better integrate the results from this research into practice:

1) The proposed finite element model needs to be extended to capture the behavior at large displacements for design with ultimate load cases. While these cases, in our experience, do not govern the design of offshore monopiles, it would be helpful for the proposed approach to capture both design cases realistically.

2) The effects of cyclic loading on stiffness and permanent displacement need to be incorporated into (1) the laboratory testing procedures to characterize these properties of the sand and (2) into the finite element model to represent these properties realistically.

3) Simpler design approaches to adjust the p-y curves used in current practice to better represent the behavior of laterally loaded piles at small (service load) displacements need to be refined and made as practical as possible.

4) Additional analyses of field data from lateral load tests (e.g., the PISA lateral load tests on piles in sand) and monitoring results from offshore wind turbines are always needed to better understand and characterize the complicated behavior of laterally loaded piles subjected to many cycles of load at relatively small amplitudes of displacement.

Reference

API. (2011). Geotechnical and Foundation Design Considerations, *2003*(April 2011).

Benz, T. (2007). *Small-Strain Stiffness of Soils and its Numerical Consequences*. *University of Stuttgart*.

Beuckelaers, W. J. A. P. (2017). Numerical Modelling of Laterally Loaded Piles for Offshore Wind Turbines.

Bryne, B., Burd, H., Mcadam, R., and Houlsby, G.T. (2017). PISA: New design methods for offshore wind turbine monopiles.

Cox, W. R., Reese, L. C., & Grubbs, B. R. (1974). Field Testing of Laterally Loaded Pi les In Sand. *Offshore Technology Conference*.

Darendeli, M. B. (2001). Development of a new family of normalized modulus. *UT Austin Dissertation*, *1542*(9), 33–36. https://doi.org/10.1017/CBO9781107415324.004

DNV.GL. (2016). DNVGL-ST-0126 : Support structures for wind turbines. *Dnv Gl As*, (April 2016).

DNV. (2014). DNV-OS-J101 Design of Offshore Wind Turbine Structures. *May*, (May), 212–214.

Hardin, B. O., & Drnevich, V. P. (1972). Shear Modulus and Damping in Soils: Dsesign Equations and Curves. *Soil Mechanics and Foundations Division*, (SM7), 667–692. https://doi.org/10.1017/S000748530002229X

Isenhower, W. M., & Wang, S. (2013). Technical Manual for LPile 2018 (Using Data Format Version 10), *2013*(October).

Ishibashi, I., & Zhang, X. (1993). Unified dynamic shear moduli and damping ratio of sand and clay. *Japanese Society of Soil Mechanics and Foundation Engineering*, *33*, 182–191. https://doi.org/10.1248/cpb.37.3229

Joh, S. H. (1996). Advances in the data interpretation technique for spectral-analysis-of-surface-waves (SASW) measurements. *Doctoral Dissertation*, 240.

Kacar, O., & Onur. (2014). Building a framework for predicting the settlements of shallow foundations on granular soils using dynamically measured soil properties. *UT Austin Dissertation*.

Luke, B.A. and Stokoe, K.H. (1998) "Application of the SASW Method Underwater," *Journal of Geotechnical and Geoenvironmental Engineering*, American Society of Civil Engineers, Vol. 124 No. 6, June, 1998, pp. 523-531.

Lee, B., Rosenblad, B.L., Wright, S.G. and Stokoe, K.H. (1997) "Analytical Study of Surface Wave Testing Along the Seafloor, Proceedings, 1997 Offshore Technology Conference, OTC 8326, Houston, TX, May 5-8, 1997.

LEBLANC, C., HOULSBY, G. T., & BYRNE, B. W. (2010). Response of stiff piles in sand to long-term cyclic lateral loading. *Géotechnique*, *60*(2), 79–90. https://doi.org/10.1680/geot.7.00196

Little, R.L. and Briaud, J.L. (1988). Full scale cyclic lateral load tests on six single piles in sand.

Menq, F.-Y. (2003). Dynamic Properties of Sandy and Gravelly Soils. *UT Austin Dissertation*. Retrieved from http://dspace.lib.utexas.edu/bitstream/2152/980/1/menqf032.pdf

Middelweerd, L. (2017). Sensitivity analysis of the first natural frequency of the offshore wind turbines in the Eneco Luchterduinen wind farm Sensitivity analysis of the first natural frequency of the offshore wind turbines in the Eneco Luchterduinen wind farm.

PLAXIS. (2016). PLAXIS Material Models Manual.

Reese, L. C., Cox, W. ., & Koop, F. . (1997). Analysis of laterally loaded piles in sand. *6th Annual Offshore Technology Conference*. https://doi.org/10.4043/2080-MS

Senanayake, A., Gilbert, R. B., Wang, S., & Rendon, E. (2015). DESING OF WIND TURBINE MONOPILES FOR LATERAL LOADS.

Weijtjens, W., & Devriendt, C. (2017). Temporal evolution of stiffness for offshore monopile foundations, (June), 2017. https://doi.org/10.13140/RG.2.2.14862.56644

Tatsuoka, F., Presti, D.L., Kohata, Y. (1995). Deformation Characteristics of Soils and Soft Rocks under Monotonic and Cyclic Loads and Their Relationships